Cerebrospinal Fluid Pulsations and Aging Effects in Mathematical Models of Hydrocephalus

by

Kathleen Patricia Wilkie

A thesis
presented to the University of Waterloo
in fulfillment of the
thesis requirement for the degree of

Doctor of Philosophy

in

Applied Mathematics

Waterloo, Ontario, Canada, 2010

Author's declaration

I hereby declare that I am the sole author of this thesis. This is a true copy of the thesis, including any required final revisions, as accepted by my examiners.

I understand that my thesis may be made electronically available to the public.

Abstract

In this Thesis we develop mathematical models to analyze two proposed causative mechanisms for the ventricular expansion observed in hydrocephalus: cerebrospinal fluid pulsations and small transmantle pressure gradients.

To begin, we describe a single compartment model and show that such simple one-dimensional models cannot represent the complex dynamics of the brain. Hence, all subsequent models of this Thesis are spatio-temporal.

Next, we develop a poroelastic model to analyze the fluid-solid interactions caused by the pulsations. Periodic boundary conditions are applied and the system is solved analytically for the tissue displacement, pore pressure, and fluid filtration. The model demonstrates that fluid oscillates across the brain boundaries. We develop a pore flow model to determine the shear induced on a cell by this fluid flow, and a comparison with data indicates that these shear forces are negligible. Thus, only the material stresses remain as a possible mechanism for tissue damage and ventricular expansion.

In order to analyze the material stresses caused by the pulsations, we develop a fractional order viscoelastic model based on the linear Zener model. Boundary conditions appropriate for infants and adults are applied and the tissue displacement and stresses are solved analytically. A comparison of the tissue stresses to tension data indicates that these stresses are insufficient to cause tissue damage and thus ventricular expansion.

Using age-dependent data, we then determine the fractional Zener model parameter values for infant and adult cerebra. The predictions for displacement and stresses are recomputed and the infant displacement is found to be unphysical. We propose a new infant boundary condition which reduces the tissue displacement to a physically reasonable value. The model stresses, however, are unchanged and thus the pulsation-induced stresses remain insufficient to cause tissue damage and ventricular expansion.

Lastly, we develop a fractional hyper-viscoelastic model, based on the Kelvin-Voigt model, to obtain large deformation predictions. Using boundary conditions and parameter values for infants, we determine the finite deformation caused by a small pressure gradient by summing the small strain deformation resulting from pressure gradient increments. This iterative technique predicts that pediatric hydrocephalus may be caused by the long-term existence of small transmantle pressure gradients.

We conclude the Thesis with a discussion of the results and their implications for hydrocephalus research as well as a discussion of future endeavors.

Acknowledgments

This Thesis would not have been possible without the support of several people. I would like to thank my supervisor, Siv Sivaloganathan, for introducing me to mathematical medicine, for connecting me to distinguished researchers in the field of hydrocephalus, and for teaching me the importance of politics in academia. I would also like to thank Corina Drapaca, without her patience and willingness to answer my questions via email, I would surely have been lost. A special thanks should be made to Giuseppe Tenti, for the useful discussions and suggestions in the darkest of times, to James Drake for sharing his insights and experiences that can only come from dealing with hydrocephalus patients every day, and to Miles Johnston for showing me the joys of working in such a controversial area of research. I also wish to thank all of the committee members for their comments on my Thesis: S. Sivaloganathan, G. Tenti, M. Kohandel, J. Wan, J. Drake, and A. Wineman.

I would like to thank the Applied Math department, especially our wonderfully helpful secretary Helen Warren, and all the graduate students and friends I have met along this incredible journey. I thank my family for their support over the past seven years of graduate school, and I thank my friends for distracting me from my research and keeping me sane. Special thanks go to Nikola Lang for keeping me laughing through the ups and downs of research and to Laurie Sutton for understanding exactly what I was going through.

Lastly, I must thank my husband Michael La Croix for the LaTeXconsultations, technical support, and encouragement. You have given me all that I needed in the ways that you knew how, and I thank you.

Kathleen Patricia Wilkie
Monday, August 16, 2010

Table of Contents

List of Tables

List of Figures

Chapter 1

Introduction

In recent years, the biomechanics of brain tissue has been the subject of much interest in the literature. Mathematical models capable of correctly predicting the brain's response to mechanical stresses induced by surgical procedures, traumatic injuries, or conditions such as hydrocephalus, aid in the design of better diagnoses, treatments, and protocols. In this Thesis, we develop mathematical models to analyze medical theories for the pathogenesis of hydrocephalus.

Hydrocephalus is a condition that arises due to a perturbation in the balanced dynamics and interaction of cerebrospinal fluid (CSF), blood, and brain parenchyma. The condition is characterized by enlarged ventricles and compressed white and gray matter, and often has an associated increase in mean intracranial pressure and/or CSF pulse amplitude. Other associated phenomena of hydrocephalus include the presence of edema (fluid accumulation), and damage to the tissue near the ventricles. Although the earliest known instances of hydrocephalus date back to the time of Hippocrates, the pathophysiology of hydrocephalus is still poorly understood, and is the subject of active debate in the literature.

Brain tumours, infections, and traumas can all lead to the development of hydrocephalus. When hydrocephalus develops from a known cause it is usually called secondary hydrocephalus, since it develops after a primary injury. Hydrocephalus can also develop from unknown causes, and it is this type that we shall focus on in this Thesis. It has been estimated that out of every 1000 live births, 1 to 2 babies are born with hydrocephalus, making it as common a congenital condition as Down syndrome; also, an estimated 375 000 older Americans are currently believed to be suffering from normal pressure hydrocephalus, with many of these cases being undiagnosed or misdiagnosed [2].

Traditionally, hydrocephalus has been classified into two distinct classes: the first is non-communicating hydrocephalus, where the circulation of CSF is somehow impeded (by a tumour occluding an aqueduct, for example), and the second is communicating hydrocephalus, where the CSF circulates freely, but absorption is compromised (due to infections such as meningitis, for example).

A special, and quite puzzling, case of great clinical interest in communicating hydrocephalus is that of normal pressure hydrocephalus, where the ventricles are enlarged with accumulated CSF, but the intracranial pressure is within the normal range.

In non-communicating hydrocephalus, a large pressure gradient forms across the blockage and thus provides an underlying mechanism responsible for ventricular expansion and tissue compression. In communicating hydrocephalus, however, the free circulation of CSF implies that no significant pressure gradient can exist, and indeed this has been verified experimentally. In this Thesis, we focus on theories for the pathogenesis of communicating hydrocephalus and thus, for brevity, the term hydrocephalus is used to mean communicating hydrocephalus except where otherwise noted.

We will analyze two of the current theories for ventriculomegaly in hydrocephalus. The first theory claims that the pulsations of the cerebrospinal fluid damage the tissue near the ventricles, causing the ventricles to expand and the parenchyma to compress. We refer to this theory as the pulsation-damage hypothesis of hydrocephalus. Using both poroelastic and viscoelastic mathematical models, we will show that the CSF pulsations of a hydrocephalic brain are incapable of causing damage to healthy brain tissue, and thus, the basis on which the pulsation-damage hypothesis rests, is unfounded.

The second theory for ventricular expansion presumes that the brain tissue's ability to absorb fluid is abnormally elevated, creating an intramantle pressure gradient, with high fluid pressure outside the tissue and low fluid pressure inside the tissue. In addition to this, a transmantle pressure gradient must exist with a magnitude smaller than the sensitivity of experimental sensors. These pressure gradients, in combination with a reduced Young's modulus due to tissue degradation, are theorized to be the mechanisms underlying ventricular expansion in hydrocephalus. We call this theory the absorption-degradation hypothesis of hydrocephalus. Using a hyper-viscoelastic model, we will show that in infant hydrocephalus, where the value of the steady-state elastic modulus is reduced compared to the adult value, a small transmantle pressure gradient is sufficient to cause ventricular expansion. This suggests that the absorption-degradation hypothesis of ventricular expansion is plausible and worthy of further investigation.

In the process of analyzing these two medical hypotheses, we will also attempt to answer some of the questions posed by Bergsneider, Egnor, and Johnston, *et al.* in their paper entitled *What we don't (but should) know about Hydrocephalus* [10]. Specifically, we attempt to answer the following questions:

1. "Why do the ventricles dilate in communicating hydrocephalus?",
2. "What causes normal pressure hydrocephalus?", and
3. "How is the brain of a child with hydrocephalus different from that of a young or elderly adult?".

Organization of this Thesis

The remainder of this Thesis is organized as follows.

Chapter 2 briefly introduces the physiology and medical background necessary to have a clear picture of the clinical condition known as hydrocephalus. Two medical hypotheses are then described for the pathogenesis of hydrocephalus. An in-depth discussion of the experimental evidence supporting these theories, the current mathematical modelling attempts, and the limitations of the hypotheses and modelling attempts are also presented. The Chapter concludes with a description of the modelling approaches used in this Thesis, these include time-dependent pressure volume models and both poroelastic and viscoelastic mechanical models.

Many mathematical models have been proposed in the quest to understand the pathophysiology of hydrocephalus. The simple, and hence commonly used, pressure volume models, and analogous electric circuit models, have possibly been overused and stretched beyond their capabilities. Chapter 3 uses constant and phenomenological forms of the cranial compliance to demonstrate that pressure volume models are incapable of describing the complex dynamics of the CSF. By comparing the predictions of the pressure volume models to clinical observations, we demonstrate in Chapter 3 that such models are unable to accurately predict the pulsatile dynamics of CSF.

The next two Chapters develop mathematical models to investigate the effects of CSF pulsations on brain tissue, in order to determine their significance in the pathogenesis of hydrocephalus, with specific reference to the pulsation-damage hypothesis. In Chapter 4 we present a poroelastic model for the brain which permits analysis of the interaction between the fluid and solid phases of the tissue. Pressure pulsations are incorporated via boundary conditions and the pulse amplitudes are determined from experimental data. Numerical simulations of the analytic solutions for displacement and fluid filtration demonstrate the effect CSF pulsations have on the brain. We also present a model of fluid flow though a single pore to determine the shear stresses induced on the tissue by the fluid filtration. This shear stress is found to be negligible in comparison to experimental data. Thus, the effect of CSF pulsations on the fluid phase of brain tissue is found to be incapable of causing tissue damage, leaving only the effects of the CSF pulsations on the solid phase as a possible mechanism for ventricular expansion in the pulsation-damage hypothesis.

In Chapter 5, we analyze the mechanical effects of the CSF pulsations on the solid phase of brain tissue using a fractional Zener viscoelastic model. The fractional differential operator incorporates a history-dependence into the constitutive equation of the material and, in Chapter 5, we hypothesize that this operator is capable of capturing microstructural changes in the tissue. The infant and adult cases of hydrocephalus are distinguished by prescribing different conditions at the outer boundaries, and numerical simulations of the analytic solutions demonstrate the effects of the CSF pulsations. The internal stresses predicted by this model are compared to experimental data and are found to be

too small to cause tissue damage. Thus, we conclude that CSF pulsations are incapable of causing sufficiently large internal stresses to damage healthy brain tissue, leaving no mechanism for ventricular expansion in the pulsation-damage hypothesis.

In Chapter 6, we determine the model parameter values of several viscoelastic models for both infant and adult brain tissue using age-dependent shear complex modulus data. The fractional Zener model parameters are then used to recompute the simulations of the previous Chapter. The infant model is found to predict tissue displacements that are unphysical for our model geometry and a new boundary condition is proposed to replace the weak condition of a stress-free outer boundary used in Chapter 5. The material stresses are relatively unaffected by the new parameter values with an order of magnitude still incapable of causing tissue damage. Parameter sensitivity analyses identify the steady-state elastic modulus as the parameter of interest in the development of hydrocephalus: it is found to depend on age, increasing from a minimum value for infant cerebrum to a maximum value for young adult cerebrum, and, in Chapter 6, we hypothesize that the steady-state elastic modulus then slowly decreases with age. The low steady-state elastic modulus of the infant brain (and possibly the aged brain) increases the tissue's susceptibility to large deformations and thus to the ventricular expansion characteristic of hydrocephalus.

With regards to the absorption-degradation hypothesis, in Chapter 7 we investigate the potential of small pressure gradients to cause ventricular expansion in infant brains. A hyperelastic, fractional derivative viscoelastic model is derived to describe infant brain tissue under conditions consistent with the development of hydrocephalus. Both the small strain oscillatory response and the step response of the material are analyzed, and an incremental numerical technique is developed to determine the relationship between tissue deformation and applied pressure gradients. Using parameter values appropriate for the infant brain, we show in Chapter 7 that pressure gradients on the order of 1 mm Hg are sufficient to cause hydrocephalus. This is significant since such small pressure gradients are below the sensitivity threshold of pressure transducers and are thus undetectable experimentally. Predicting brain tissue deformation resulting from pressure gradients is of interest and relevance to the treatment and management of hydrocephalus, and to the best of our knowledge, this is the first time that results of this nature have been presented.

Finally, in Chapter 8 we summarize the results and discuss the implications of the analyses presented in this Thesis. Reviewing the results of both the poroelastic and viscoelastic analyses of the effects of CSF pulsations on healthy brain tissue suggests that the pulsation-damage hypothesis should be revised. In addition, reviewing the hyper-viscoelastic analysis suggests that the absorption-degradation hypothesis is worthy of further investigation. The Chapter concludes by listing the experimental data that would be useful in pursuing the concepts discussed and conjectures made in this Thesis. We also describe possible future projects that would extend or explore further the ideas contained within this Thesis.

Chapter 2

Preliminaries

In this Chapter we provide a brief introduction to the physiology of the cranium, as well as the clinical condition known as hydrocephalus, and various medical theories concerning its pathogenesis. We conclude the Chapter with descriptions of the mathematical models used in this Thesis to analyze these medical theories.

2.1 Physiology

The brain and spinal cord comprise the human central nervous system. *Cerebrospinal fluid* (CSF) surrounds the central nervous system and it also fills the four interconnected interior regions, or *ventricles*, of the brain. Effectively, the brain and spinal cord are submerged in a CSF bath which protects, nourishes, and cleanses the tissue. The *choroid plexi* of the ventricles produce about 80% of the CSF, while the remainder is produced by the tissue itself. The normal circulation of CSF flows from the two lateral ventricles into the third then fourth ventricle and finally into the *subarachnoid space* (SAS). It also flows through the brain parenchyma from the ventricles to the SAS. From here, it may flow down into the spinal cord central canal or spinal SAS, or it may be absorbed [64]. CSF was previously believed to be primarily absorbed by the arachnoid villi into the cranial venous sinuses; however, recent work by Johnston and coworkers [92] has challenged this traditional view of CSF circulation and absorption. The overwhelming body of experimental evidence amassed by Johnston *et al.* now implicates the nasal mucosal lymphatic system as the major site of CSF absorption. Figure 2.1 shows the central nervous system and the circulation of CSF.

Brain tissue is a unique tissue of the human body for three reasons. First, the brain has no lymphatics. One of the primary functions of the lymphatic system is to remove interstitial fluid from tissues, and since the brain does not have any lymphatic vessels, this mechanism for fluid removal is not directly available. Second, the blood brain barrier, which only exists in the central nervous system,

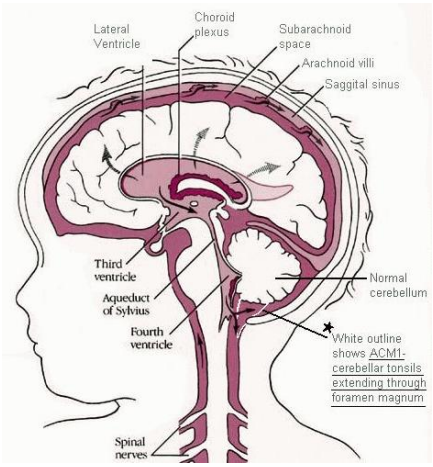

Figure 2.1: CSF flow in the cranial cavity. Image courtesy of [3].

restricts the normal transcapillary flow of nutrients. The barrier, formed by tight junctions between endothelial cells, restricts large molecules from diffusing into the tissue and instead active transport is required to transport specific nutrients into the brain tissue. Third, while all tissues have interstitial spaces filled with interstitial fluid, the space and fluid surrounding the cells, brain tissue also has four interior ventricular compartments that are filled with interstitial fluid, or CSF.

The cranial cavity holds three basic components inside the skull: CSF, brain parenchyma, and blood. The contents of the skull are connected to the spinal cord through the foramen magnum. By conservation of volume, if the intracranial volume of one of these components increases, then assuming incompressibility of all components, a necessary decrease in volume must occur in at least one of the other components. During systole, arterial blood pulses into the cranial cavity. Venous blood and CSF respond by pulsing out of the cranial cavity; venous blood flows back to the heart, and CSF flows down through the foramen magnum into the spinal SAS. Since arterial pressure is pulsatile with a frequency commensurate with that of the heartbeat, the CSF and venous blood also pulse with this frequency [48]; however, despite the pulsatile intracranial arterial, CSF, and venous flow, capillary flow is essentially non-oscillatory. The oxygenated blood vessel network of artery to arteriole to capillary provides enough resistance to smooth out the pulsatile nature of the flow.

The movement of CSF from the cranium to the spinal SAS is one example of a volume compensation mechanism available to the cranium. The intracranial compensatory mechanisms range in reaction time from rapid to slow. Distention of the spinal SAS, CSF absorption, and collapse of veins and sinuses are rapid compensation mechanisms that respond to the arrival of arterial blood [74]. They also act to dampen the cardiac pulse. Larger reductions in CSF volumes,

decreases in extracellular volume, and vasoconstriction occur quickly, but not quickly enough to damp the cardiac pulse. Cell volume loss is the slowest compensatory mechanism, allowing for tissue volume loss to compensate for volume gain in CSF or blood [74].

The fluid pressure in the ventricular CSF is called the *intracranial pressure* (ICP). It is oscillatory and is dependent on factors such as the heart rate, respiratory rate, coughing, and straining [76]. CSF and venous blood are able to quickly compensate for the arterial pulsations since they are both connected to lower pressure regions outside of the cranium. When the CSF and venous blood compensatory mechanisms are exhausted, ICP will increase and eventually become unstable [76]. *Compliance* is a measure of how volume changes occur in response to changes in pressure. Mathematically, this is expressed as

$$C = \frac{\Delta V}{\Delta P}. \tag{2.1}$$

Elastance is the reciprocal of compliance. Compliance and elastance, common parameters in the hydrocephalus literature, are not to be confused with the mechanical concepts of elasticity [128]. Increasing the volume of intracranial blood or CSF eventually exhausts the compliance of the cranium which destabilizes the ICP. At this point, small changes in intracranial volume will produce very large changes in ICP. In an adult, these large changes in pressure can cause herniation of the brain through the foramen magnum [76].

Brain tissue consists of neuronal and glial cells which produce, organize, remove, and attach to the *extracellular matrix* (ECM). The ECM is a collection of fibers, such as versican and hyaluronic acid, which provide the scaffolding of the tissue, and cells attach to these fibers via the *integrins* that protrude from their membranes. The development, shape, migration, proliferation, survival, and function of most cells are influenced by the ECM [55]. The tissues of the central nervous system are classified as either gray or white matter and structural differences between these two types occur due to factors such as the concentration of blood vessels, the level of myelination, and the physical arrangement of the axons. As a result, gray matter has a higher structural resistance to deformation (is stiffer) than white matter. Furthermore, white matter is more anisotropic than gray matter, displaying a strong directional dependence [61].

Brain ECM has low concentrations of the common proteins found in other tissue matrices such as collagen and fibronectin, and instead it appears to be primarily composed of a family of proteoglycans called lecticans and two ECM components to which they bind, tenascin and hyaluronic acid [105]. The ECM of cartilage is also abundant in hyaluronic acid and here it appears to provide a cushioning mechanism. The acid binds large quantities of water that can be released when the tissue is compressed and reabsorbed when the compression is released. It is likely that a similar mechanism occurs in brain ECM. Another commonality between brain and cartilage is the relatively rare occurrence of non-local cancer invasion. Ruoslahti [105] hypothesized that the uniqueness of

the brain ECM may resist invasion from cancer cells except from glial cancer cells, which may possess the mechanisms to circumvent this resistance since they normally exist in this unique matrix environment.

According to Holbourn [54], the most important physical properties of brain tissue are the comparatively uniform density, the extreme incompressibility, and the small modulus of rigidity. Neural cells, blood, and CSF all have approximately the same density as water, giving brain tissue an approximately uniform density. Brain tissue strongly resists changes in volume due to hydrostatic pressures, and in comparison, it provides little resistance to changes in shape. Thus, the *bulk modulus* (resistance to uniform compression) of brain tissue is large compared to the *shear modulus* (rigidity under shear strains), and in this case, tissue damage is proportional to the shear strain [54]. Due to the geometry of the brain, the ventricle walls are more prone to damaging shear strains, and this damage may consist of tearing of the blood vessels, axons, and synapses, or disruption of the cell bodies. This damage may be sufficient to disturb brain function even if it is insufficient to cause tissue breakage [54].

Brain tissue is a viscoelastic material, meaning it behaves like an elastic solid on short time scales and like a viscous fluid on long time scales. It has a strong strain-rate dependence. In this Thesis, the following four simplifying assumptions of brain tissue are made:

- The CSF, interstitial fluid, and other fluids that may exist in brain parenchyma are not differentiated and they are all referred to as CSF.
- The structural differences between gray and white matter are neglected and they are assumed to be mechanically equivalent in both their elastic properties and their permeabilities.
- The ventricle walls are assumed to have the same permeability and mechanical properties as brain parenchyma.
- The cranial SAS is assumed to be negligibly thin, so that the brain parenchyma and skull share a common boundary.

These assumptions simplify the mathematical analyses while not significantly detracting from the results or conclusions of this Thesis.

2.2 Hydrocephalus

Hydrocephalus is a clinical condition of the brain caused by a disturbance in the production, absorption, or flow of CSF. It is characterized by the presence of enlarged ventricular cavities. A tumour impairing the flow of CSF into the cranial and spinal subarachnoid spaces is one possible cause of hydrocephalus. This case is called *non-communicating* since the normal circulation of CSF is inhibited. Traumas and infections such as meningitis are other possible causes of hydrocephalus. These cases are called *communicating* since the CSF is free

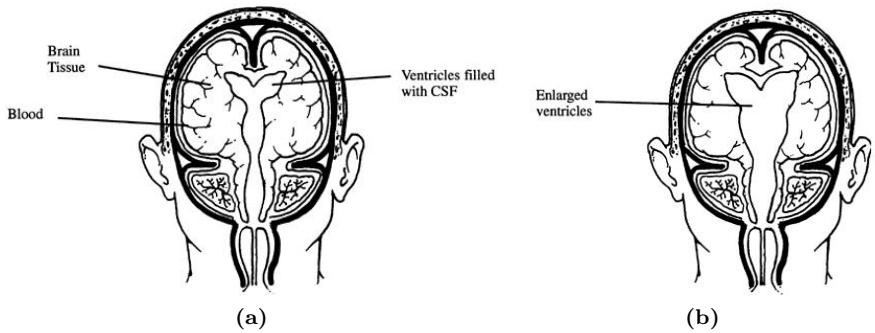

Figure 2.2: Illustrations of a normal brain (a) and a hydrocephalic brain (b). Images courtesy of [87].

to move into the spinal SAS but not into the cranial SAS where absorption occurs [64]. In all cases, the ventricles become enlarged at the expense of brain parenchyma. Increased volume of intracranial CSF causes the brain tissue to be squeezed between the extended ventricular walls and the skull. Figure 2.2 illustrates a normal brain and a hydrocephalic brain.

In non-communicating hydrocephalus, the blockage that impedes the circulation of CSF causes fluid accumulation. Fluid pressure builds up in the ventricles which provides the force necessary to expand the ventricle walls and compress the brain parenchyma. Communicating hydrocephalus is a curious phenomena because no obstruction exists, and hence no pressure gradient exists between the central ventricles and the subarachnoid space, (i.e. no *transparenchymal* gradient exists). This fact has been verified experimentally [68]. Nevertheless, the cerebral ventricles still become enlarged and the brain parenchyma still becomes compressed. Elevated mean ICP and elevated ICP wave amplitudes are often observed in communicating hydrocephalus, but are not necessary. *Normal pressure hydrocephalus* (NPH) is a puzzling class of communicating hydrocephalus where ventricular enlargement occurs but the ICP is only slightly elevated and still within the normal range.

Although hydrocephalus can occur at any age, until the last decade the most common occurrence of this clinical condition was in the pediatric population. With improving health care and an aging population, however, the situation has changed to a great degree and the occurrence of hydrocephalus has seen a marked increase amongst the elderly, whilst there has been some decline in the pediatric population [27]. This does not mean that infant hydrocephalus is no longer a clinical concern. In 1992, estimates of the incidence of congenital hydrocephalus were about 3 to 4 per 1000 live births [56] and statistics from the U.S. Centers for Disease Control and Prevention from 2001 indicate that approximately 7 infants out of every $100,000$ live births died from congenital hydrocephalus [39]. For comparison, estimates of the incidence of NPH among those residing in assisted-living or extended-care facilities ranges from 9 to 14% [72].

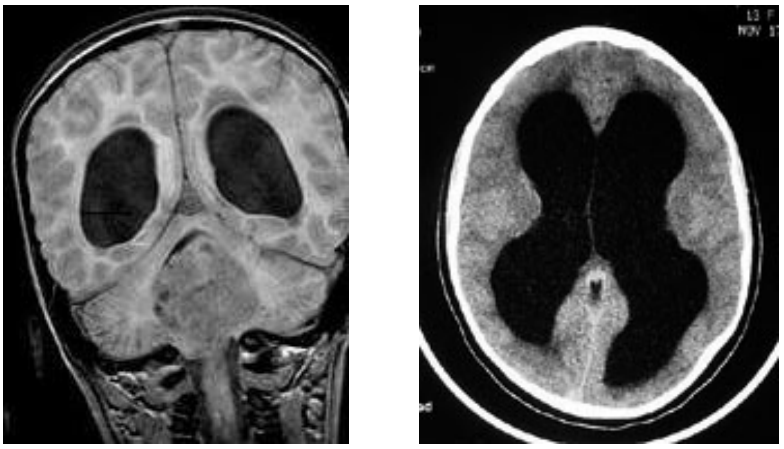

(a) (b)

Figure 2.3: Coronal (a) (image courtesy of [89]) and transaxial (b) (image courtesy of [27]) MR images of hydrocephalic brains.

Symptoms of hydrocephalus can vary and depend on patient age. In infants, where the cranial plates are not yet fused, the fontanel (soft spot) may bulge, the scalp may appear thin with full veins, and the plates may feel separated. The patient may experience vomiting, sleepiness, irritability, and a downward cast to the eyes. In older children and adults, where the sutures are now fused, symptoms include headache, nausea, vomiting, blurred vision, balance problems, gait disturbance (or delayed development in children), poor coordination, and a decline in mental performance. Most commonly found in the elderly population, NPH is usually diagnosed by Hakim's triad of symptoms: gait disturbance, urinary incontinence, and dementia, and it is often misdiagnosed as either Parkinson's disease or Alzheimer's disease. Medical imaging (either MR or CT) is normally performed to determine the extent of the ventricular enlargement, and a frontal horn span greater than 5.5 cm or an Evans ratio (the ratio of the maximum width of the frontal horns to the maximum width of the brain) greater than 0.4 is an indicator of hydrocephalus [125]. Figure 2.3 shows sample MR images of hydrocephalic brains. In severe cases of hydrocephalus, an accumulation of extracellular fluid, or *edema*, is observed in the parenchyma near the ventricles (the *periventricular region*) [59] which appears as a periventricular lucency in MR images. Tissue damage in the periventricular region and ventricle walls is also commonly observed in hydrocephalus.

The causes of hydrocephalus are many and varied. Some forms are congenital while others result from infections, hemorrhages, traumas, or tumours. There is no known cure for hydrocephalus, but treatments exist to help manage the condition. Commonly, mechanical shunts are used to drain excess CSF from the ventricles into other regions such as the peritoneal cavity. Certain patients

may be suitable for a third ventriculostomy which is a surgical procedure that creates a new pathway for CSF in order to restart the circulation. And finally, pharmacological treatments are being investigated. Unfortunately, the most common treatment, shunting, is riddled with complications. Shunt malfunction, subdural hematoma, seizure, infection, and intracerebral hematoma are a few examples of these complications. It has been estimated that of the over 40 000 hydrocephalus operations performed annually in the US, only 30% of these are the patient's first surgery [2].

2.3 Theories of Ventriculomegaly

A fundamental understanding of the development of communicating hydrocephalus, especially NPH, has remained elusive, although putative theories have been proposed [9, 32, 33, 64, 93]. In non-communicating hydrocephalus, it is easy to understand that ventricular expansion results from the accumulated fluid and pressure build-up that occurs behind the obstruction inhibiting the normal circulation of CSF. Since this standard explanation does not hold for communicating hydrocephalus, new theories must be explored. Here two theories for ventricular expansion are discussed. The CSF pulsation mechanism hypothesis is presented first since it is the main theory analyzed in this Thesis.

2.3.1 CSF Pulsations

Measurements of CSF pressure clearly indicate the pulsatile nature of its flow [68], and a link between these pulsations and ventricular enlargement has been proposed. As early as 1979, supported by experimental evidence, Di Rocco *et al.* hypothesized that ventricular enlargement may be due to abnormally high ventricular CSF pressure pulse amplitudes [102].

Experimental Evidence

There is substantial evidence indicating that CSF pulsations may be involved in ventricular enlargement. Bering [11] showed that in kaolin-induced hydrocephalus, the removal of the choroid plexus from one lateral ventricle caused dilation to mainly occur on the side with the choroid plexus intact. Milhorat [77] tried to reproduce these results by removing the choroid plexus from one lateral ventricle and inducing hydrocephalus by blocking the aqueduct. He observed that both ventricles dilated, thus showing that while pulsations may be important in the pathogenesis of communicating hydrocephalus, they are not necessary in the pathogenesis of non-communicating hydrocephalus. Wilson and Bertan [133] extended the work of Bering by obstructing the artery leading to one of the lateral ventricles. After inducing hydrocephalus, they found that the ventricle with the obstructed artery had a smaller CSF pulse amplitude and was smaller in size compared to the unobstructed side. They concluded that ventricular

pressure pulsations driven by the intracranial arteries were responsible for the formation of hydrocephalus.

Guinane [49] injected silicone into the subarachnoid space adjacent to a ventricle and observed localized ventricular dilation. He claimed the silicone reduced the compliance of the CSF space and increased the strain-stress ratio in the ventricular wall, thus concluding that the increased strain caused the tissue destruction (stretching) he observed in the *ependyma* (ventricle wall). Di Rocco [101] conducted experiments by pulsing a balloon inserted into a lateral ventricle to increase the amplitude of the CSF pulsations. He found that ventricular dilation occurred, with the balloon-inserted ventricle being larger than the other lateral ventricle. He also found that when the pulsing balloon was inserted into the parenchyma, ventricular dilation was not observed. Hence he concluded that the pulsations must originate in the ventricles for ventriculomegaly to occur. In a Letter to the Editor responding to the work of Di Rocco *et al.* [102], McLone provided a possible explanation for increased CSF pulse amplitudes without increased mean ICP [74]. He claimed that the ventricular pulse generated by the choroid plexus may be larger than the parenchyma pulse if the rapid compensatory mechanisms of the cranium are impaired. Loss of elasticity from hypertension or aging may transmit the cardiac pulse more to the choroid plexus than to the cerebral tissues. Coupled with partial obstruction of CSF circulation, he hypothesized that this could explain NPH.

The Pulsation-Damage Hypothesis

The theory of CSF pulsations as a causative mechanism for hydrocephalus is based on the assumption that these pulsations damage the ventricle walls and surrounding tissue. In systole, the choroid plexus becomes enlarged with blood which generates a pressure pulse in the surrounding CSF. Since CSF is incompressible, the pulse is transmitted without attenuation or phase lag to the ventricle walls and brain parenchyma. The pulse is finally absorbed by the SAS, dura, and skull. In diastole, blood returns to the heart, decreasing the volume of the choroid plexus and depressurizing the ventricle walls. The pressurization cycle repeats with the heart rate, during which CSF may oscillate in and out of the ventricle walls and parenchyma. These constant oscillations may generate large shear stresses in the periventricular tissues which may damage the cells. The damaged tissue may lose its structural integrity, becoming more porous and allowing oscillating CSF to penetrate increasingly deeper. This will propagate the damage into the tissue, compressing the parenchyma behind the expanding ventricles. Increased CSF pressure pulse amplitudes, often observed in hydrocephalus, will exacerbate this damage mechanism. One theory for this increased pulsatility is a decrease in the cranial compliance due to a blocked CSF or venous pathway [11].

Modelling Attempts

With the majority of mathematical models focusing on CSF bulk flow, to date, not much work has been done to incorporate pulsatile CSF dynamics into models of hydrocephalus. The first attempt to model these pulsations was work by Egnor *et al.* [32, 33] which reignited the debate over the role of pulsations in the development of hydrocephalus [122, 123, 65]. Encouraged by the observation that intracranial arterial, CSF, and venous pressure waveforms are all approximately simultaneous [97], Egnor *et al.* suggested that the cranial compartment is in what they called a *natural state of resonance*. They claimed that deviations from this state lead to a loss of normal cerebral blood and CSF flows and ultimately to the development of hydrocephalus.

The model proposed by Egnor *et al.* [32, 33] is a simple linear damped oscillator:

$$m_{CSF}\,\ddot{x}_{CSF}(t) = F_0 \sin(\omega t) - R\dot{x}_{CSF}(t) - k_E\,x_{CSF}(t), \tag{2.2}$$

where m_{CSF} is the mass of displaced CSF, $x_{CSF}(t)$ is the displacement of CSF, ω is the angular heart frequency, F_0 is the amplitude of the arterial pulsations, R is a resistive damping parameter, and k_E is the elastic constant of the intracranial contents. Since MRI techniques are capable of measuring CSF velocity, v_{CSF}, they differentiate to get

$$m_{CSF}\,\ddot{v}_{CSF}(t) + R\dot{v}_{CSF}(t) + k_E\,v_{CSF}(t) = \omega F_0 \cos(\omega t), \tag{2.3}$$

which has the oscillatory long-time solution

$$v_{CSF}(t) = \frac{F_0 \sin(\omega t - \theta)}{\sqrt{R^2 + \left(\omega m_{CSF} - \frac{k_E}{\omega}\right)^2}}, \tag{2.4}$$

where θ is the phase angle between the arterial and CSF oscillations given by

$$\theta = \arctan\left(\frac{\omega^2 m_{CSF} - k_E}{\omega R}\right).$$

Forcing θ to be zero to ensure synchronous arterial and CSF pulsations results in the relation

$$\omega^2 = \frac{k_E}{m_{CSF}}. \tag{2.5}$$

This synchronous state is what they call the natural state of resonance [32]. Finally, Egnor *et al.* [33] extended this model using an analogous RLC circuit, and concluded that ventricular dilation in communicating hydrocephalus is a result of the redistribution of intracranial pulsations.

This synchronous state, however, is not resonance, since resonance requires a large amplitude response in time and this does not occur in the intracranial compartment or in their solution, (2.4). Tenti *et al.* [122] argued that, assuming

(2.5) holds, if the heart rate is increased, say by physical exercise, then assuming the mass of CSF is approximately constant, the intracranial elastic constant must also increase. If the elasticity is allowed to change in time, $k_E = k_E(t)$ and their solution (2.4) and conclusions are no longer valid. Furthermore, their model cannot explain why everyone does not develop hydrocephalus if ventriculomegaly results from mere changes in the heart rate away from this natural frequency.

In 2005, Linninger *et al.* [68] modelled pulsatile CSF using the Navier-Stokes equations and brain parenchyma using linear elasticity theory. They assumed no absorption of CSF by the parenchyma. Thus, the interaction between pulsatile CSF and elastic parenchyma reduced, once again, to a damped linear oscillator. In 2007, they extended this model by allowing CSF not only to flow through the parenchyma, but also to be produced in the parenchyma [67]. This model predicted slightly higher pressures inside the tissue than in the ventricles or SAS. They were able to simulate hydrocephalus by decreasing the CSF absorption, the cranial compliance[1], and the parenchyma permeability and porosity parameters. These changes caused the ICP pulsations to be larger in amplitude and the ventricles to be larger in volume than the normal brain simulation. The model does not, however, demonstrate the significance of the CSF pulsations in ventriculomegaly.

Tully and Ventikos [126] also used poroelasticity and computational fluid dynamics to examine the effect of CSF pulsations and aqueduct stenosis on the development of hydrocephalus. While they did allow for fluid flow through the poroelastic material, they did not analyze the effect of the pulsations on the internal stresses or shear flow induced stresses. Nevertheless, they concluded that the pulsations have negligible effect on the displacement of the parenchyma and thus on the development of hydrocephalus.

Critiques

There are several problems with the pulsation-damage theory of hydrocephalus. Perhaps most convincing, as pointed out by Levine [65], is the fact that conditions such as hypercapnia and pseudotumor cerebri, which are known to increase CSF pulsatility, are not associated with hydrocephalus. Also pointed out by Levine [65] is the following contradiction: if ventricular expansion occurs due to tissue damage, and the propagation of this damage into the parenchyma, then how can the relatively quick reduction of ventricle volume observed after shunt treatment be explained? Furthermore, if the pulse amplitudes are the same in the ventricles and the SAS then the pulsation-damage theory cannot explain why the ventricles enlarge and the SAS does not. One reason for this could be a small difference between the pulse amplitudes of the ventricles and SAS. Large differences cannot occur as evidenced by experiment [68]. Levine

[1]The author believes that the hydrocephalus simulations of [67] used a decreased value of the parameter β, entitled "inertia resistance of the tissue", and that a typo exists in Table II of the article.

calls these potential small differences in pulse amplitude *mini-gradients* and their effect will be investigated in Chapter 4. Finally, the most obvious problem with this theory is that if ventriculomegaly is caused by the sole actions of the CSF pulsations on the ependyma and parenchyma then why do not we all have hydrocephalus?

2.3.2 Parenchyma Fluid Absorption

The second theory for the pathogenesis of communicating hydrocephalus was first proposed in a short paper from 2002 by Peña *et al.* [93]. They hypothesized that ventriculomegaly may be caused by the reversal of CSF flow into the parenchyma, instead of out of the parenchyma, combined with a reduced tissue elasticity or *Young's modulus* (rigidity under tensile strains).

Experimental Evidence

Dye or radio-labelled albumin injected into a ventricle was later found in the brain tissue and blood [82]. This suggests that a bulk flow of CSF from the ventricles into the parenchyma exists and that fluid absorption might also occur via the capillaries of the brain [64]. Ventricle perfusion experiments suggest that there is a reversal of the normal transependymal flow, and that interstitial fluid may flow from the ventricles into the brain tissues [104]. In experiments where the aqueduct was occluded to isolate the ventricles from the subarachnoid space, CSF absorption was found to balance CSF production [12]. Finally, perivascular spaces have been shown to serve as conduits to transport cerebral interstitial fluid to both blood and lymph drainage sites [21]. Unfortunately, there is evidence both for and against absorption of CSF by the parenchyma [64], with perhaps the strongest argument against absorption being the presence of edema, or fluid build-up, in the periventricular tissue.

The *pressure volume index* (PVI) is a tool used to quantify the health of the cranial compartment. It is defined as the volume of fluid necessary to raise the ICP by a factor of 10 and it is measured by injecting mock CSF into the ventricles while recording the immediate peak pressure response. Pang and Altschuler [91] measured the pressure volume index in patients with low pressure hydrocephalus and found it to be abnormally high. They argued that since the "give" of the cranium is negligible in adults and the expansion of the venous pool is unlikely, the only explanation for the large PVI is a change in the viscoelastic properties of the brain tissue. Regardless of this conclusion, their argument is flawed since Walsh and Schettini showed that there is no correlation between the elastic properties of brain tissue and elastance, or by extension, the pressure-volume index [128]. Chapter 6 of this Thesis presents evidence that the elastic properties of brain tissue are age-dependent and it is theorized that a reduced elastic modulus may be a contributing factor to ventricular expansion.

Recent research from Johnston and collaborators [86] indicates a possible molecular mechanism for the pathogenesis of hydrocephalus. An injection of

antibodies to β_1-integrins was made to the ventricles of rats while measurements of the periventricular tissue pressure were obtained. They found that the antibodies diffused into the tissue and caused a temporary drop in the tissue pressure as well as ventricular enlargement. This problem was discussed during the OCCAM-Fields-MITACS Biomedical Problem Solving Workshop held in Toronto, Ontario, 2009. The hypothesis formed by the contributors, including the author of this Thesis, is that since the antibodies temporarily inhibit the ability of cells to bind with the ECM, a structural relaxation in the ECM is created which may degrade the elastic modulus and lower the interstitial fluid pressure of the tissue [9]. This exciting work suggests a possible molecular mechanism which may alter the microstructure of brain tissue and thus may be an important factor in the pathogenesis of communicating hydrocephalus.

The Absorption-Degradation Hypothesis

This relatively recent theory for communicating hydrocephalus is based on the belief that the brain tissue surrounding the ventricles is able to absorb CSF. This absorption may be driven by either osmotic or hydrostatic pressure gradients at the capillaries. Whether or not it can be attributed to ECM restructuring, a lower hydrostatic pressure is assumed to exist inside the tissue compared to the ventricles or SAS. This *intramantle* pressure gradient (from ventricle and SAS to the inside of the tissue) drives CSF into the parenchyma for absorption. A small *transmantle* pressure gradient (from ventricle to SAS) must also exist to ensure the ventricles enlarge and the SAS compresses. The result is tissue compression, especially if the Young's modulus is reduced due to tissue degradation.

Modelling Attempts

Peña *et al.* hypothesized that communicating hydrocephalus can be caused by the flow of CSF into the parenchyma, and of CSF absorption by the parenchyma, as well as a reduced tissue elasticity [93]. Using Biot's theory of consolidation to govern the tissue motion, they solved the poroelasticity equations on a finite element mesh generated from a brain MR image. Their "reduced" Young's modulus values of 1 kPa for white matter and 5 kPa for gray matter, are small in comparison to some estimates of brain tissue elasticity (10 kPa [59] or 21 kPa [121]) but large in comparison to other estimates (584 Pa [120]). While the ventricle and SAS pressures were defined to be 10 mm Hg, the tissue pressure was defined to be 7.5 mm Hg. Unfortunately, the paper does not discuss the details of their mathematical model and so it is unclear how they enforced this tissue pressure. It is mentioned, however, that they do not consider venous pressures and thus they do not model capillary absorption. Nevertheless, their work was the first to propose the potential existence of an intramantle pressure gradient instead of the customary transmantle pressure gradient.

Levine [64] examined the parenchyma absorption hypothesis using a poroelastic model with varying levels of seepage of CSF into the parenchyma as well

as varying levels of absorption by the parenchyma. Fluid absorption by the capillaries was assumed to be proportional to the net osmotic and hydrostatic pressures according to Starling's Law. Without the existence of permanently raised ICP, i.e. for NPH, Levine concluded that CSF seepage into the tissue and efficient absorption by the parenchyma are sufficient to cause ventriculomegaly. His theory, however, requires an initial increase in ICP to compress the brain tissue, expand the ventricles, initiate the flow of CSF into the parenchyma, and initiate the CSF absorption mechanism.

The molecular mechanism proposed by Johnston and colleagues [86] explains the flow of CSF into the parenchyma without the need for an increased ICP. As well, the absorption mechanism may be triggered by osmotic pressure changes that result from the antibody presence. A preliminary mathematical model of this mechanism was proposed by the OCCAM-Fields-MITACS Biomedical Problem Solving Workshop group [9]. Here, poroelasticity theory was used with parameters such as the Young's modulus and permeability made to vary with the antibody concentration. Parenchymal absorption of CSF was also made to depend on the concentration of antibodies. This preliminary model still awaits refinement and numerical simulation.

Critiques

It is unclear why, in the model proposed by Peña *et al.* [93], the ventricles enlarge more than the SAS if the pressures are defined to be the same in both of these regions. Recall that they prescribed pressures of 10 mm Hg in the ventricles and SAS and 7.5 mm Hg in the parenchyma. Linninger *et al.* [68] showed that no significant (greater than 1 mm Hg) pressure gradients exist between the ventricles, parenchyma, or SAS. Thus, only small pressure gradients, on the order of 1 mm Hg or less, can exist as either intramantle or transmantle gradients. If an intramantle pressure gradient exists to drive CSF into the parenchyma for absorption, then there must also be a small transmantle pressure gradient to explain the ventricular expansion and the SAS compression. The ability of such a small pressure gradient to enlarge the ventricles enough to cause hydrocephalus is discussed in Chapter 7.

2.4 Modelling Approaches of this Thesis

The main intent of this Thesis is to analyze the effect of the CSF pulsations in order to determine their role in the pathogenesis of hydrocephalus. To complete this task, several mathematical models are used. Mathematical models have been used to study hydrocephalus since the pioneering work of Hakim *et al.* [50, 51] in the 1970's. Models of hydrocephalus allow for the investigation of mechanical stresses and the long-term effects of abnormalities in the dynamics of CSF and in the mechanical properties of the tissue. Most models to date, however, have focused on the bulk flow of CSF instead of also considering its pulsatile nature. The ultimate goal of a mathematical model is to elucidate

the pathogenesis of the condition it describes by proposing hypotheses which can be experimentally verified. A successful model of hydrocephalus should be able to explain or demonstrate most of the experimental observations discussed above as well as to deepen our understanding of ventricular enlargement and to improve treatment strategies.

In the literature, there are two main approaches to the mathematical modelling of hydrocephalus. The first approach uses time-dependent models such as pressure volume models [71, 115] and the analogous electrical circuit models [32, 33, 57]. The second approach uses time- and space-dependent mechanical models such as those based on the poroelastic [64, 67, 85, 93, 118, 121, 126] or viscoelastic theories [29, 31, 113, 114, 132].

2.4.1 Time-Dependent Models

The Monro-Kellie hypothesis simplifies the dynamics of the cranium to an underlying competition for space between CSF, blood, and brain parenchyma. This hypothesis leads to pressure volume models where the CSF is contained within one compartment, the outside of which represents the brain parenchyma and SAS [115]. Analogous electric circuit models have been presented as extensions of the pressure volume concept [32, 33, 57]. As mentioned earlier, the relationship between pressure and volume is called compliance. Several forms of the cranial compliance function have been proposed [71] but they provide little information on the behaviour of the brain [115]. Many proponents of pressure volume models have erroneously believed that cranial compliance and tissue elasticity are related [91]. Walsh and Schettini [128], however, showed that there is in fact no relationship between these two parameters. They measured brain elasticity and intracranial compliance as the intracranial pressure was increased by incrementally inflating a ventricular balloon. These measurements showed that compliance decreased with increasing pressure but that tissue elasticity remained essentially constant.

Numerous models of hydrocephalus incorporating both time- and space-dependencies have been proposed and are discussed in the next section. Unfortunately, these models usually involve systems of partial differential equations which require several parameters making them much more complex than the tantalizingly simple ordinary differential equation models discussed here. In fact, in Chapter 3 we will demonstrate that these simple time-dependent DE models are incapable of representing the complex dynamics of the cranium and that they provide little insight towards a more fundamental understanding of the development of hydrocephalus.

2.4.2 Mechanical Models

Continuum mechanics provides the framework necessary to derive time- and space-dependent mathematical models of hydrocephalus. The theory of porous

media was originally developed for the study of hydrogeology, such as earthquakes and oil extraction [16]. In 1941, Biot [15] used phenomenologically-based assumptions to derive his theory of consolidation which describes the mechanics of a porous elastic solid saturated with a viscous fluid. Later, Burridge and Keller [16] showed that in the limit where the dimensionless viscosity for the small scale was order unity, Biot's equations could be obtained directly from the microstructure of the material by averaging over the fast spatial variations. In the other limit, where the dimensionless viscosity for the large scale was order unity, they were able to derive equations describing a viscoelastic material.

The modelling approach chosen to best describe the behaviour of brain tissue depends on the application being studied. Poroelastic models are capable of describing the fluid-solid interactions and can account for the intrinsic porosity of brain tissue. Viscoelastic models, on the other hand, are capable of describing the strain-rate dependence of brain tissue. The characteristic time scale of the application is a good indication of which modelling approach is appropriate. Impacts are usually modelled with viscoelasticity while long-term processes are modelled using poroelasticity (or mixture theory) which accounts for the interstitial fluid movement [61]. Franceschini *et al.* [40] found that the drained behaviour of brain parenchyma should be treated as a nearly incompressible nonlinear material, capable of permanent deformations, and that it is qualitatively similar to rubber-like materials. Kyriacou *et al.* [61] compared viscoelastic and poroelastic models of brain tissue and they recommended viscoelastic models for short time scale phenomena and poroelastic models for long time scale phenomena. For hydrocephalus, generally considered a long time scale phenomenon, a poroelastic model was recommended [61]. Franceschini *et al.* [40] also recommend a poroelastic model for brain tissue in situations where substantial volumetric deformations occur (i.e. hydrocephalus).

Unfortunately, the use of poroelastic and viscoelastic models are hindered by the difficulties associated with accurately measuring the required model parameters, such as the permeability, and the viscoelastic behaviours, such as creep and relaxation, of brain parenchyma. In this Thesis, in order to analyze the effect of CSF pulsations, a short time scale phenomenon, a poroelastic model is used to analyze the effect of the pulsations in terms of the fluid-tissue interactions. Then, viscoelastic models, which are more appropriate for short time scale phenomena, are used to examine the tissue deformations and stresses. A brief discussion of both poroelastic and viscoelastic models of brain biomechanics is presented below.

Poroelasticity Theory

In 1976, Hakim *et al.* [51] introduced a mechanical model which described brain parenchyma as a porous viscoelastic sponge. They claimed that the tissue was able to compress in response to a transmantle pressure gradient by collapsing the sponge cells. Nagashima *et al.* [85] extended this model by applying Biot's theory of consolidation [15] to describe the porous matrix, or tissue, which is

saturated by the viscous fluid, or CSF. Under loading conditions, deformations of a porous medium are accompanied by fluid flow through the medium. This is consistent with the observed behaviour of biological tissues, which are generally believed to be biphasic [59]. In fact, this biphasic behaviour explains why hyperosmotic drugs, such as mannitol, are useful in alleviating elevated intracranial pressure by reducing the fluid volume of the brain. If there was no underlying relationship between the hydrated nature of the brain and its solid tissue matrix, the drug would not be able to relieve the herniation that can occur at the foramen magnum [40].

The application of Biot's theory of consolidation to brain biomechanics initiated the widespread use of poroelasticity theory in the hydrocephalus modelling literature [59, 64, 93, 117, 118, 121, 126, 134]. In these models, the brain is assumed to be a porous linear elastic sponge saturated and contained in a viscous incompressible fluid similar to water. Poroelastic models account for the interaction of CSF with the brain parenchyma and thus are capable of describing the consolidation effects associated with high values of mean stresses applied for long times [40], as occur, for example, in the development of hydrocephalus. In Chapter 4, a poroelastic model is used to analyze the fluid-solid matrix interactions associated with CSF pulsations in order to determine their role in ventriculomegaly.

Viscoelasticity Theory

Elastic behaviour occurs when the stress depends only on the strain and it is characterized by instantaneous deformation upon loading as well as an instantaneous return to the original state with unloading. Viscoelastic behaviour occurs when the stress depends on both the strain and the strain history [61]. Such materials display both elastic and viscous characteristics. Viscous behaviour is characterized by strains that grow linearly with the applied stress. The result of combining these two characteristics is that viscoelastic materials display curious behaviours such as creep, relaxation, and hysteresis. Creep is the process of continued straining in response to the application of a constant stress, relaxation is the process of the material stress decaying in response to a constant strain, and hysteresis describes the result of mechanical energy dissipation during cyclic loading, i.e. the loading curve takes a slightly different path than the unloading curve. Perhaps most important to the analyses in this Thesis, is that the effective stiffness of a viscoelastic material depends on the rate at which the load is applied.

Since brain tissue displays such a strong strain-rate dependence, many constitutive equations have been proposed in the literature in an attempt to describe this behaviour mathematically [28, 29, 36, 43, 75, 79, 80, 90, 129]. Nonlinear viscoelastic constitutive equations, such as the hyper-viscoelastic model presented in Chapter 7, are capable of more accurately predicting large material deformations than linear viscoelastic or poroelastic models. This is due to the assumption of small strains in all linear models. Fractional derivatives have

recently been incorporated into the constitutive relations describing brain tissue [23, 132, 66]. This addition requires the materials entire stress-strain history to be known in order to determine the current stress-strain state. The advantage of fractional derivatives is that they are capable of describing the complex behaviour of polymer-like materials, such as brain tissue, with a relatively small number of model parameters. In Chapter 5, a fractional viscoelastic model is used to analyze the effect of CSF pulsations on ventricular expansion. Chapter 6 determines age-appropriate model parameters of this fractional viscoelastic model and reanalyzes the effects of the CSF pulsations. And finally, in Chapter 7, a fractional hyper-viscoelastic model is used to analyze the ability of small hydrostatic pressure gradients to enlarge the ventricles in infant hydrocephalus.

Chapter 3

A Pressure Volume Model for Pulsatile CSF Dynamics

In this Chapter, we refute the claim, based on the analysis of pressure volume models, that the relationship between arterial-ICP synchronicity and hydrocephalus is causal. We suggest instead that both are consequences of altered cranial compliance and resistance to CSF absorption. To conclude the Chapter, we claim that pressure volume models, and in fact all such spatially averaged time-dependent models (including analogous circuit models), are too simple to account for the complex CSF dynamics observed in the cranium, especially during the development and treatment of hydrocephalus.

A complex relationship exists between intracranial pressure, intracranial compliance, and hydrocephalus. Hydrocephalus is believed to reduce intracranial compliance by restricting the cerebral vasculature and compressing the brain parenchyma and SAS, thus limiting the volume compensatory mechanisms of the cranium. Several theories exist claiming that this change in compliance causes the ventricles to expand in hydrocephalus [46, 47, 116]. Experiments show that in patients with reduced compliance as a result of hydrocephalus, the amplitude of ICP pulsations increases but decreases back to normal after shunt insertion [108, 116], which is believed to increase compliance by creating a new volume-compensatory mechanism. As demonstrated in this Chapter, pressure volume models are capable of predicting this phenomenon; decreasing compartment compliance causes increased pressure amplitude but not increased mean pressure in the model predictions; however, the level to which the compliance must be reduced is not physical.

Cranial compliance is related to the pressure volume index and mean ICP. A reduced cranial compliance corresponds to an elevated elastance, that is, a greater rise in pressure is the result of the same change in volume. The PVI of hydrocephalic patients, however, may be elevated or reduced compared to a normal PVI since it depends on the mean ICP. For reference, a mean CSF pressure of 13.2 mm Hg, a mean PVI of 25.9 ml, and a mean compliance of 0.85 ml/mm Hg

were found for normal adults [110]. In a study of hydrocephalic patients with a mean ICP of 31.7 mm Hg, a mean PVI of 24.1 ml and a mean compliance of 0.33 ml/mm Hg were found [107]. In the same study, hydrocephalic patients with a mean ICP of 7.8 mm Hg were found to have a mean PVI of 12.7 ml and a mean compliance of 0.71 ml/mm Hg [107]. Thus the hydrocephalic patients with elevated ICP had a PVI near normal and a reduced compliance, whereas the patients with normal ICP had a reduced PVI and only a slightly reduced compliance. Hydrocephalus patients, however, do not always present with reduced cranial compliance. In low-pressure hydrocephalus patients, mean ICP of 4.4 mm Hg, the mean PVI was measured to be 43.9 ml [91], which corresponds to a compliance of 4.3 ml/mm Hg. Similarly, in hydrocephalic infants, a mean ICP of 11.7 ml/mm Hg and a mean PVI of 28.1 ml [109] were found; this corresponds to a compliance of 1.0 ml/mm Hg. Unfortunately, from a modelling perspective, the mean ICP pulse amplitudes were not reported in any of these studies.

Mean ICP is affected by the resistance to fluid flow, sometimes called resistance to CSF absorption or resorption. It is a measure of the difficulty at which CSF flows from the ventricles to the SAS and finally to the venous system. If a linear relationship is assumed between the amount of CSF absorbed and the pressure difference between the ventricular CSF and the venous blood, then the resistance to CSF absorption can be defined as the ratio of the change in this pressure difference to the change in the rate of absorption [64]. Therefore, if CSF absorption is impaired, resistance to CSF absorption increases, and ICP must increase to maintain the balance of production and absorption. The mean resistance to absorption was measured to be 2.8 mm Hg/ml/min in healthy adults with a mean ICP of 11.7 mm Hg [110]. In hydrocephalic patients, the mean resistance among those with an ICP above 15 mm Hg was 38.8 mm Hg/ml/min, and the mean resistance among those with an ICP below 15 mm Hg was 23.5 mm Hg/ml/min [107]. In hydrocephalic infants, the mean resistance was found to be 7.2 mm Hg/ml/min when the mean ICP was 11.7 mm Hg [109].

The synchrony between arterial and CSF pressure pulsations has been demonstrated experimentally [46] as has the effect these pulsations seem to have on the observed enlargement of the ventricles [11, 133]. According to the theory proposed by Egnor *et al.* based on an RLC circuit model [32], development of hydrocephalus is due to the lack of synchrony between the CSF and the cerebral blood pulsations. They claim that decreased intracranial compliance introduces a phase lag in the ICP pulse, and the existence of such a phase lag has been observed in some animal experiments [101].

In this Chapter we demonstrate that this lack of synchrony is not the cause of hydrocephalus, but rather that it may be related to variations in the compliance and resistance to fluid flow. Analysis of the mathematical model reviewed in this Chapter will show that when intracranial compliance decreases, the ICP and arterial pressure pulses become synchronous. Model predictions that match the amplitude of observed pressure pulsations only occur, however, when the

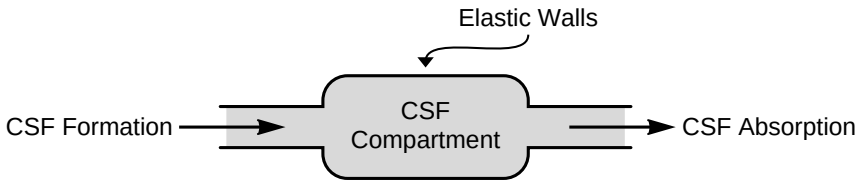

Figure 3.1: A one compartment model for CSF with compliant walls.

intracranial compliance is reduced to an unphysical level. The requirement of an unphysical compliance and the lack of spatial dependence indicate that pressure volume models, in general, and analogous circuit models in particular, simplify the dynamics of the cranium to the point where they are not longer capable of accurately describing the behaviour of cranial CSF. Furthermore, in hydrocephalus, where increased CSF pressure amplitudes occur with any combination of an increased or decreased mean ICP and PVI, the dynamics are too complex for these simple models to accurately describe.

3.1 Pressure Volume Model Formulation

Sivaloganathan *et al.* [115] provide a comprehensive review of time-dependent mathematical models describing CSF dynamics. They propose a simple differential equation that encompasses all of the single compartment models found in the literature. Here, we modify their CSF source term to incorporate the effect of arterial pulsations on CSF dynamics. A schematic of the CSF compartment model is shown is Figure 3.1.

The governing equation, which describes the dynamics of the CSF compartment is derived from the principle of conservation of mass. For constant density, this requires that the rate of change of volume must be equal to the difference between the rate of formation, $I_f(t)$, and the rate of absorption, $I_a(t)$, that is,

$$\frac{\mathrm{d}V}{\mathrm{d}t} = I_f(t) - I_a(t). \tag{3.1}$$

From infusion studies, the absorption term is assumed to have the form [115]

$$I_a(t) = \frac{1}{R_a}\left(P(t) - P_{ss}\right), \tag{3.2}$$

where R_a is the resistance to CSF flow, $P(t)$ is the spatially-averaged CSF pressure, and P_{ss} is the pressure in the sites of CSF absorption (typically the sagittal sinus [110] and nasal lymphatics [58, 92, 100]). The formation rate is assumed to have the form

$$I_f(t) = I_f^{(e)} + S(t), \tag{3.3}$$

where $I_f^{(e)}$ is the bulk formation rate and $S(t)$ is the CSF source term which will incorporate the effect of the pulsatile blood flow into the model. Since CSF is essentially incompressible, the rate of volume change can be related to the rate of change of pressure using the chain rule and the compliance function $C(P) = \frac{\mathrm{d}V}{\mathrm{d}P}$. Using the chain rule as well as (3.1), (3.2), and (3.3) results in the model equation (3.4), which describes a CSF compartment with compliant walls, a source, and a sink,

$$C(P)\frac{\mathrm{d}P}{\mathrm{d}t} + \frac{1}{R_a}\big(P(t) - P_{ss}\big) = I_f^{(e)} + S(t). \tag{3.4}$$

As blood flows into brain parenchyma, the volume of the parenchyma expands and, as a result, some CSF is pushed into the compartment out of the extracellular space of the brain tissue and choroid plexi. This increase in CSF volume results in an increase in CSF pressure which pushes back on the parenchyma, resulting in a reduction in brain tissue volume as the blood leaves. Following a suggestion of Fung [42], we assume the CSF formation source term to have the following form,

$$S(t) = a\sin^2(\omega t), \tag{3.5}$$

where a is the peak-to-peak amplitude of the non-zero average pulsations and 2ω is the angular frequency of the heart beat in radians per minute. The value $\frac{1}{2}a$ is the volume of CSF displaced due to blood flow through the brain parenchyma per minute. Substituting this source term into (3.4), the model equation becomes

$$C(P)\frac{\mathrm{d}P}{\mathrm{d}t} + \frac{1}{R_a}\left(P(t) - P_{ss}\right) = I_f^{(e)} + a\sin^2(\omega t). \tag{3.6}$$

3.2 Numerical Simulations

Equation (3.6) describes the dynamics of pulsatile CSF in a compliant compartment. Two cases of particular forms of the compliance function will be analyzed: first, the simple case where the compliance is constant, and second, the case where the compliance function has a particular phenomenological form.

3.2.1 Constant Compliance

As a first approximation, the compliance of the compartment is assumed to be constant, $C(P) = C_0$, and so (3.6) becomes

$$C_0\frac{\mathrm{d}P}{\mathrm{d}t} + \frac{1}{R_a}\left(P(t) - P_{ss}\right) = I_f^{(e)} + a\sin^2(\omega t). \tag{3.7}$$

With the initial condition, $P(0) = P_0$, the differential equation can be solved using Laplace Transforms. Introducing a characteristic time of $\tau_0 = C_0 R_a$, the

CSF pressure is given by

$$P(t) = \left(P_0 - R_a I_f^{(e)} - P_{ss} - \frac{aR_a}{2}\frac{4\omega^2\tau_0^2}{1+4\omega^2\tau_0^2}\right) \mathrm{e}^{-\frac{t}{\tau_0}} + \left(R_a I_f^{(e)} + P_{ss} + \frac{aR_a}{2}\left(1 - \frac{1}{\sqrt{1+4\omega^2\tau_0^2}}\right)\right) + \frac{aR_a}{\sqrt{1+4\omega^2\tau_0^2}} \sin^2\left(\omega t - \frac{1}{2}\arctan(2\omega\tau_0)\right). \tag{3.8}$$

The first bracketed terms give the transient response, or the effect of the initial condition. Since we are only interested in the long-time effect of the arterial pulsations on the CSF dynamics, we neglect the transient terms leaving only constant terms and a term with the same form as the pulsation source. The phase of the CSF pulsations with respect to the source term (3.5) is given by

$$\phi = \frac{1}{2}\arctan(2\omega\tau_0), \tag{3.9}$$

and upon inspection, three interesting cases of the phase lag emerge:

1. if $2\omega\tau_0 \ll 1$ then $\phi \approx 0$,
2. if $2\omega\tau_0 \approx 1$ then $\phi \approx \frac{\pi}{8}$, and
3. if $2\omega\tau_0 \gg 1$ then $\phi \approx \frac{\pi}{4}$.

Thus, if the characteristic frequency, $\frac{1}{\tau_0}$, is much larger than the angular heart frequency (2ω) then the CSF pressure pulsations will be in phase, or synchronous, with the blood pulsations. Otherwise, the CSF pressure pulsations will lag the blood pulsations. Furthermore, decreasing the phase shift to zero requires decreasing the characteristic time scale, τ_0, by decreasing the compliance and/or decreasing the resistance to fluid flow.

The parameter values used to numerically simulate the pressure in a normal adult cranium are listed in column one and three of Table 3.1. Column two will be used in the criteria enforcing simulation discussed later. Typical values of P_{ss} (taken as the sagittal sinus pressure), R_a, and C_0 for a normal human adult were found by Shapiro *et al.* [110]. The rates of CSF formation, $I_f^{(e)}$ and a, are based on a daily production rate of 500 ml, and the angular frequency is based on a heart rate of 70 beats/min.

The result of simulating the CSF pressure using the normal adult parameter values of Table 3.1 is shown in Figure 3.2a. The resulting pressure pulsations are very small, and would most likely not be visible in a typical intracranial pressure measurement. This does not accurately represent actual observed measurements where the pulsations are approximately 5 mm Hg in peak-to-peak amplitude [110].

Using the equation for CSF pressure (3.8), parameter values can be derived which produce more accurate predictions compared to observed measurements. The following criteria for CSF pressure are imposed:

1. CSF and arterial pulsations should be synchronous (zero phase shift),
2. pulsations should have a peak-to-peak amplitude of 5 mm Hg, and
3. the average long-time CSF pressure should be 13.5 mm Hg.

The first criterion implies that $2\omega C_0 R_a \ll 1$, thus we require:

$$C_0 = \frac{1}{10}\frac{1}{2\omega R_a}. \tag{3.10}$$

It follows that the long-time behaviour of the CSF pressure can be expressed as $P(t) = R_a I_f^{(e)} + P_{ss} + aR_a \sin^2(\omega t)$. Therefore, imposing a peak-to-peak amplitude of 5 mm Hg implies

$$aR_a = 5, \tag{3.11}$$

and imposing a long-time average CSF pressure of 13.5 mm Hg implies

$$R_a I_f^{(e)} + P_{ss} + \frac{1}{2}aR_a = 13.5. \tag{3.12}$$

Table 3.1: Parameter values for the constant compliance pressure predictions of an adult cranium shown in Figure 3.2.

Normal Adult Values [110]	Criteria Values	Assigned Values
$C_0 = 0.85$ ml/mm Hg	$C_0 = 3.0 \cdot 10^{-5}$ ml/mm Hg	$I_f^{(e)} = 0.01$ ml/min
$R_a = 2.8$ mm Hg/ml/min	$R_a = 7.5$ mm Hg/ml/min	$a = 0.67$ ml/min
$P_{ss} = 12.2$ mm Hg	$P_{ss} = 10.9$ mm Hg	$\omega = 70\pi$ rad/min

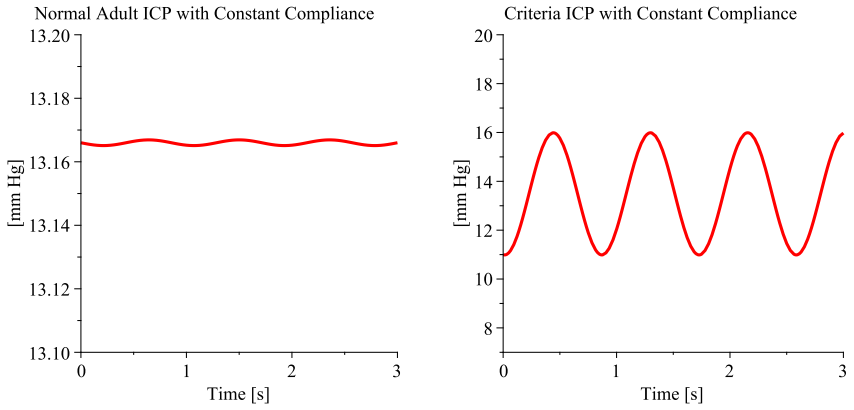

Figure 3.2: CSF pressure predictions for a constant compliance compartment using normal human adult parameter values (a), and using parameter values determined by the imposed criteria (b).

Solving these criteria along with the CSF production requirement of 500 ml/day results in the new parameter values listed in the second column of Table 3.1.

Figure 3.2b shows the CSF pressure predicted by these new parameter values. The simulation resembles intracranial pressure measurements for normal humans presented in [110]. The values for the resistance to fluid flow, R_a, and the site of absorption pressure, P_{ss}, determined by the criteria, are close to those measured by Shapiro *et al.* [110]; however, in order for this simple pressure volume model to accurately predict normal CSF dynamics, the compliance of the CSF compartment needs to be on the order of 10^{-5} ml/mm Hg. This is approximately 5 orders of magnitude smaller than the compliance measured by Shapiro. Furthermore, the phase shift predicted by this model using the normal adult parameter values is $\phi \approx 0.78 \approx \frac{\pi}{4}$ rad whereas the phase shift using the parameter values determined by the imposed criteria is $\phi \approx 0.05$ rad. Thus using normal adult parameter values, this pressure volume model does not accurately represent the observed dynamics of intracranial CSF.

3.2.2 Phenomenological Compliance

In 1978, Marmarou *et al.* [71] showed that the CSF pressure volume curve is exponential in shape and that the compliance of the compartment should decrease as CSF pressure increases. They expressed this relationship by defining the compliance function as

$$C(P) = \frac{1}{kP}, \tag{3.13}$$

where $k = \frac{1}{0.4343\text{PVI}}$ and PVI is the pressure volume index. Using the compliance function (3.13) in the general model (3.6) results in the following nonlinear differential equation

$$\frac{1}{kP(t)}\frac{\mathrm{d}P}{\mathrm{d}t} + \frac{1}{R_a}\left(P(t) - P_{ss}\right) = I_f^{(e)} + a\sin^2(\omega t). \tag{3.14}$$

This Riccati equation with the initial condition $P(0) = P_0$ can be solved by changing the dependent variable to $p(t)$ via, $p(t) = \frac{1}{P(t)}$, and then using the integrating factor method. Returning to the original pressure variable, $P(t)$, gives

$$P(t) = \frac{P_0 \exp\left(k\left(I_f^{(e)} + \frac{P_{ss}}{R_a} + \frac{a}{2}\right)t - \frac{k}{4\omega}a\sin(2\omega t)\right)}{1 + k\frac{P_0}{R_a}\int_0^t \exp\left(k\left(I_f^{(e)} + \frac{P_{ss}}{R_a} + \frac{a}{2}\right)s - \frac{k}{4\omega}a\sin(2\omega s)\right)\mathrm{d}s}. \tag{3.15}$$

Figure 3.3a shows the CSF pressure predicted for a normal adult cranium at large times where the initial condition no longer affects the solution. Normal adult CSF pressure was computed using the parameter values from columns one and three of Table 3.2. The resistance to flow, pressure volume index, and absorption site pressure are measurements from Shapiro *et al.* [110] for normal adult craniums. The long-time CSF pressure, approximately 13.167 mm Hg,

Table 3.2: Parameter values for the phenomenological compliance pressure predictions shown in Figure 3.3.

Normal Adult Values [110]	Criteria Values	Assigned Values
$R_a = 2.8$ mm Hg/ml/min	$R_a = 7.5$ mm Hg/ml/min	$I_f^{(e)} = 0.01$ ml/min
$PVI = 25.9$ ml	$PVI = 0.001$ ml	$a = 0.67$ ml/min
$P_{ss} = 12.2$ mm Hg	$P_{ss} = 10.9$ mm Hg	$P_0 = 13.5$ mm Hg
		$\omega = 70\pi$ rad/min

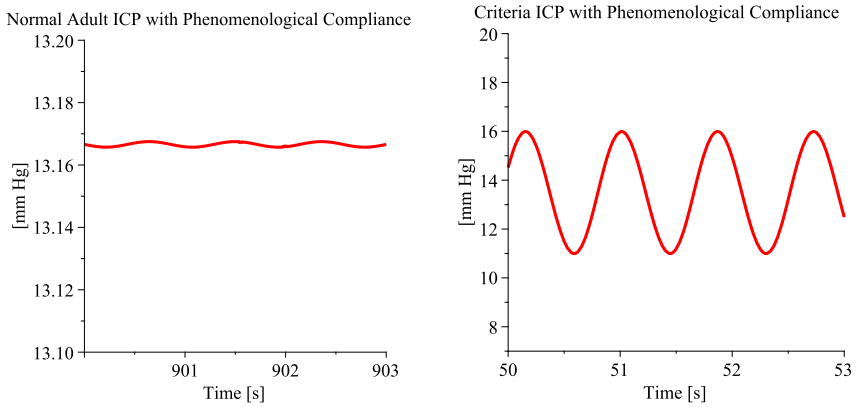

Figure 3.3: CSF pressure predictions for a compartment with a phenomenological compliance function using normal human adult parameter values (a), and using parameter values determined by the imposed criteria (b).

corresponds to a compliance of about 0.85 ml/mm Hg; however, this compliance is too large and CSF pressure pulse amplitudes on the order of 5 mm Hg peak-to-peak do not occur.

In order for the model to produce such observed pulsations in the CSF pressure, the compliance, and thus the pressure volume index, must decrease. By trial and error, a value of PVI = 0.001 ml along with the other criteria parameter values listed in Table 3.2 were found to produce pulsations with a peak-to-peak amplitude of about 5 mm Hg. This pressure volume index and an average pressure of about 13.5 mm Hg correspond to a compliance of approximately $C = 3.0 \cdot 10^{-5}$ ml/mm Hg. Hence, a compliance on the order of 10^{-5} is required to give rise to the observed pressure pulsations. This value is far smaller than any experimentally measured value of compliance [91, 107, 109, 110]. The pressure predicted using the criteria and assigned parameter values of Table 3.2 is shown in Figure 3.3b. CSF pressure pulsations are visible with a peak-to-peak amplitude of about 5 mm Hg and an average pressure of about 13.5 mm Hg.

3.3 Discussion

Assuming that the pressure volume index is 25.9 ml [110] and that CSF pressure fluctuates from 11 to 16 mm Hg in a normal human adult, implies that the compliance of the CSF compartment varies from 0.7 to 1.0 ml/mm Hg, using the phenomenological form (3.13). Thus, to a first approximation, the compliance of the CSF compartment can be considered constant. Analysis of this constant compliance case, Section 3.2.1, shows that the phase difference between the CSF pulsations and the arterial forcing depends on the compliance and the resistance to fluid flow. Assuming the pulsations are initially synchronous ($2\omega C_0 R_a \ll 1$), increasing either the compliance, C_0, or the resistance to fluid flow, R_a, introduces a phase shift. Using the measured values of compliance and resistance for normal adults [110], this model predicts a phase shift of $\frac{\pi}{4}$ rad. Thus, the synchrony between CSF and arterial pressure pulsations is due to a balance between the cranial compliance, the resistance to CSF absorption, and the angular frequency of the heart. Large disruptions in this balance are required to break this synchrony, since if $2\omega C_0 R_a \ll 1$, then doubling the heart rate will give $2(2\omega C_0 R_a) \ll 2$, and in the worst case this may be considered as $2(2\omega C_0 R_a) \leq 1$, which corresponds to a phase shift of at most $\frac{\pi}{8} \approx 0.39$, and so this may still be considered an approximately synchronous state.

The constant compliance analysis also shows that experimentally determined compliance values are too large to permit intracranial pressure measurements with visible pulsations (pulse amplitudes larger than the sensitivity of the sensors which are on the order of 1 mm Hg) in this class of models. In order for CSF pressure pulsations with an amplitude similar to experimental observations to be visible in the model predictions (5 mm Hg peak-to-peak amplitude), a compliance on the order of 10^{-5} was required. This compliance is small enough that the compartment can essentially be considered rigid. Pressure pulsations during hydrocephalus have been measured to be about 10 mm Hg peak-to-peak [35] which would require an even smaller cranial compliance. The model predictions demonstrate that with a compliance value on the order of experimentally measured values (0.85 ml/mm Hg [110]), the compartment walls absorb the effect of the source pulsations and the CSF pressure remains approximately constant.

The criteria imposed to force the model predictions to match experimental measurements also required the resistance to fluid flow to increase slightly from 2.8 to 7.5 mm Hg/ml/min and the pressure in the absorption sites to decrease slightly from 12.2 mm Hg to 10.9 mm Hg. Both of these altered values, however, still lie within the physical range associated with the model parameter [22, 110]. Resistance to fluid flow has been shown to increase nonlinearly with age [22], and is related to a decrease in the CSF production rate that occurs in elderly people [73]. Measurements of the resistance to flow in hydrocephalic patients ranged from 23.5 in patients with elevated ICP to 38.8 mm Hg/ml/min in patients with NPH [107]. Commonly found in the elderly population, NPH was hypothesized by Bateman [7] to be the result of low intracranial compliance and high impedance (which corresponds to a high resistance to fluid flow). From the

analysis of the pressure volume model presented here, the combination of a low intracranial compliance and a slightly increased resistance was shown to produce large amplitude pulsations without a jump in the mean ICP. This reproduces the conditions observed in NPH patients; however, the pressure volume index of low or normal pressure hydrocephalus patients were measured to range from 39.2 to 48.5 ml [91] which are both much larger than the value required for the simulation (0.002 ml).

It should be noted here that some experimentalists refer to a stiffening of brain tissue with age. This stiffening does not refer to changes in the mechanical parameters of brain tissue, but rather it may refer to a reduced cranial compliance due to the reduced elastic properties of the vessel walls and the decreased CSF circulation that occur with age. In this state, the brain tissue may appear to be *stiffer* because changes in the intracranial pressure result in essentially no change in the CSF volume due to the decreased compliance and limited compensatory mechanisms of the compartment. This does not give any information about the mechanical parameters of brain tissue, such as the Young's Modulus, which, as will be discussed in Chapter 6, is hypothesized to decrease with age, meaning the brain tissue actually gets *softer*. This confusion is enhanced by the term elastance, which was once thought to be a measure of brain tissue elasticity; it was later shown otherwise, that the concepts are independent [128].

Including the phenomenological form of the compliance function in the model, Section 3.2.2, and using an experimentally measured value for the pressure volume index (25.9 ml [110]), the model developed here predicts a compliance of approximately 0.85 ml/mm Hg and very small pulsations in the CSF pressure. Reducing the pressure volume index to 0.001 ml, along with slightly increasing the resistance to flow and slightly decreasing the absorption site pressure, however, results in a compliance of approximately 10^{-5} ml/mm Hg (a reduction of about 5 orders of magnitude) and predicted CSF pulsations with an amplitude of approximately 5 mm Hg peak-to-peak.

Shapiro *et al.* [110] measured the mean compliance to be 0.34 ml/mm Hg in infants and 0.62 ml/mm Hg in older children which are both smaller measurements than the mean compliance of 0.85 ml/mm Hg found for normal adults, but not small enough to produce observable pressure pulsations according to this model. This seems to indicate that the compliance of the cranium may depend on age via the growth and development of brain tissue and the resulting changes in the tissue's mechanical properties. These differences, however, are more likely attributable to the small venous blood volume in infant craniums [110]. Large venous pools in adult craniums have more blood volume to displace during the CSF bolus injection of a pressure volume index measurement. This larger displaced volume will result in a larger PVI measurement and thus a larger compliance. Even though the cranial sutures are open in infants, the force exerted by the CSF bolus injection is too small to affect the brain tissue or the surrounding unfused skull plates [110].

If this simple mathematical model correctly represents the dynamics of CSF in the cranium, then the conclusion of this analysis must be that the experi-

mentally measured values of the cranial compliance and of the pressure volume index are incorrect and off by five orders of magnitude. Assuming this not to be the case, we must conclude that this simple model, and in fact all such single-compartment models, are incapable of accurately representing the complex intracranial CSF dynamics. All single-degree-of-freedom models, including the popular RLC circuit models, simplify the relationship between intracranial pressure, intracranial compliance, and the development of hydrocephalus, to the extent where they are no longer capable of accurately predicting the dynamics of cranial CSF.

An important aspect of CSF dynamics that is lost in these models is the spatial dependence of the flow. Recent measurements show that the velocity of CSF ranges from 1 to 3 mm/s in the lateral ventricles and from 5 to 10 mm/s in the third ventricle and aqueduct [46]. Measurements of CSF velocities in the foramen magnum have been reported as large as 44 mm/s [13] and 50 mm/s [46]. According to Poiseuille's Law, fluid velocity is proportional to the pressure difference between the flow origin and the flow destination. Given that the CSF velocity varies drastically within the cranium, we must infer that CSF pressure varies spatially. This implies that a mathematical model capable of describing CSF dynamics must depend on both time and space. The analysis presented in this Chapter demonstrates that a much more complex relationship exists between the CSF flow and intracranial compliance than can be captured by simple spatially-averaged time-dependent models. This complex relationship requires more sophisticated mathematical models, in particular, models that incorporate spatial dependencies.

Chapter 4

A Poroelastic Analysis of CSF Pulsations and Hydrocephalus

In this Chapter, we use poroelasticity theory to blend the dynamics of the pulsatile CSF and the soft brain tissue in an attempt to determine the significance of intracranial pulsations on ventricular enlargement. Specifically, we examine the pulsation-damage hypothesis for ventricular enlargement. Poroelasticity theory, while simplifying the viscoelastic behaviour of brain tissue, enables the interaction between the fluid and solid phases that occur in brain tissue to be taken into account in the subsequent analysis.

Again, the pulsation-damage hypothesis assumes the following simplified explanation for the mechanism of pressure pulse generation in the cranium. In systole, the choroid plexus becomes enlarged due to an influx of arterial blood. This expanded tissue pushes on the ventricular CSF and, since CSF is an incompressible fluid, the pressure pulse is transmitted without attenuation or phase lag to the ventricle walls and brain parenchyma. The pulse is finally absorbed by the subarachnoid space, dura, and skull. In diastole, the choroid plexus decreases in volume which causes a depressurization of the ventricle wall. This cycle repeats with the angular frequency of the heart. In theory, a small amount of CSF may oscillate across the ventricle wall with each heart beat. These constant oscillations may generate large shear stresses in the ventricle wall which may explain the ependymal damage observed in hydrocephalus. As the cells closest to the ventricles become damaged, these stresses may have an impact further into the parenchyma, and over long times, this propagating damage forms the basis of the pulsation-damage hypothesis of the ventricular expansion observed in hydrocephalus [11, 49].

Recall also, that in opposition to this hypothesis, Levine [65] described three main problems with the theory. First, many conditions that increase pulsatility,

such as hypercapnia, or reduce cranial compliance, such as pseudotumor cerebri, are not associated with the development of hydrocephalus. Second, because the theory explains ventricular expansion via tissue damage it cannot account for the relatively quick reduction of ventricular volume observed after shunt treatment. And third, unless a pulse amplitude gradient is assumed, the pulsation theory cannot explain why periventricular tissues are more affected than cortical tissues. Levine continued to show that these pulse gradients cannot be large, and that only what he terms *mini-gradients* can exist.

Recent measurements by Eide *et al.* [34, 35] suggest that a small difference in pulse amplitude may exist between the ventricles and the parenchyma or SAS. Measurements from six patients with either non-communicating or communicating hydrocephalus showed elevated pressure pulse amplitudes in the lateral ventricles compared to the brain parenchyma [35]. The difference in peak-to-peak amplitude ranged from 0.4 to 2.6 mm Hg. In another study involving ten patients with idiopathic normal pressure hydrocephalus, measurements of the pressure in the parenchyma and the epidural space showed no significant difference between the wave amplitudes [34]. This suggests that the small pulse amplitude pressure gradient may be intramantle as opposed to the traditional view of a transmantle pressure gradient.

After Hakim *et al.* [51] described brain tissue as a microscopic sponge of viscoelastic material saturated by biological fluids, mathematical models of hydrocephalus based on Biot's theory of consolidation [15] (or poroelasticity theory) became prominent in the literature [59, 85, 121] . Common modifications of these models include incorporating variations in the permeability of the elastic matrix [84, 112, 118] and coupling the poroelastic equations with the Navier-Stokes equations to describe the fluid flow in the ventricles, SAS, and aqueduct [67, 117, 126]. Another modification [83] introduced elastic nonlinearity and a plastic behaviour by incrementally updating the Young's modulus, stress, and pressure of the material. Other models have incorporated absorption of cerebrospinal fluid by the parenchyma [64, 93] which creates an intramantle pressure gradient. Most of these modifications lead to complicated systems of PDEs that must be solved using computational methods.

Again, a few attempts have been made to incorporate the pulsations of the cerebrospinal fluid into the poroelastic model. Tully and Ventikos [126] coupled the poroelastic equations describing the parenchyma with computational fluid dynamics describing the flow through the aqueduct to investigate the affect of aqueduct stenosis on the development of hydrocephalus. They allowed pulsations in both the ventricle and subarachnoid space and showed that these pulsations have negligible effect on the displacement of the parenchyma. Linninger *et al.* [67] incorporated pulsations of the CSF into their computational fluid dynamics model for fluid flow in the cranium. They allowed for fluid production by the parenchyma which predicted higher pressures in the tissue than in the ventricles or SAS. This pressure difference seems contrary to the mechanics required to compress brain tissue as the ventricles expand in communicating hydrocephalus. Both of these models required solving the poroelastic equations using numerical techniques.

In this Chapter, we analytically investigate both the displacement and fluid filtration that result from CSF pulsations and pay specific attention to the interaction between the fluid and solid motions near the ventricles. Numerical predictions of the displacement, filtration velocity, and pressure in the parenchyma are presented and a parameter sensitivity analysis is performed. This analysis suggests that the cellular damage observed in the periventricular area of a hydrocephalic brain may be caused by the stresses induced by the CSF pulsations, especially with the combined effect of a reduced Young's modulus and an increased ventricular pressure wave amplitude. A model of the fluid flow in a pore of the parenchyma is developed to estimate the shear applied to the walls of the pore by the fluid motion. This shear force is found to be negligible when compared to the shear required to detach a cell from a substrate or to break a single adhesion bond. Thus, only the stress induced in the parenchyma by the continuous cycle of compression and expansion remains as the possible source of the hypothesized damaging shear forces.

4.1 Poroelastic Model Formulation

A simplified view of brain parenchyma is to think of the brain as a porous linearly elastic solid saturated in a viscous incompressible fluid. The macroscopic behaviour of biphasic materials are captured by Biot's theory of consolidation [15]. Following the work of Kenyon [60] and Tenti *et al.* [123] we study the problem on a simple model geometry for which analytic solutions can be found. Thus, we model the brain as a thick-walled cylinder (see Figure 4.1): the interior represents the ventricles whilst the exterior represents the SAS and skull, and the thick wall represents the brain parenchyma. By assuming that the ends of the cylinder are tethered, we enforce planar strains (with no coupling in the axial direction) and simplify the governing equations.

The intricate network of cells and ECM that comprise brain parenchyma make the pore structure extremely complex and impossible to determine *a priori*. Poroelasticity theory mathematically homogenizes, or smears, the elastic solid and viscous fluid together. As a result, at each point in the domain the solid and fluid phases exist simultaneously. The constitutive equations derived below refer to the macroscopic behaviour of the homogenized fluid-solid composite.

4.1.1 Equation of Motion

Let $\vec{u}$ be the displacement, ρ be the density, and $\mathbf{T}$ be the second order total stress tensor of the homogenized porous material. By conservation of momentum, the equation of motion is

$$\rho \frac{\partial^2 \vec{u}}{\partial t^2} = \nabla \cdot \mathbf{T}, \tag{4.1}$$

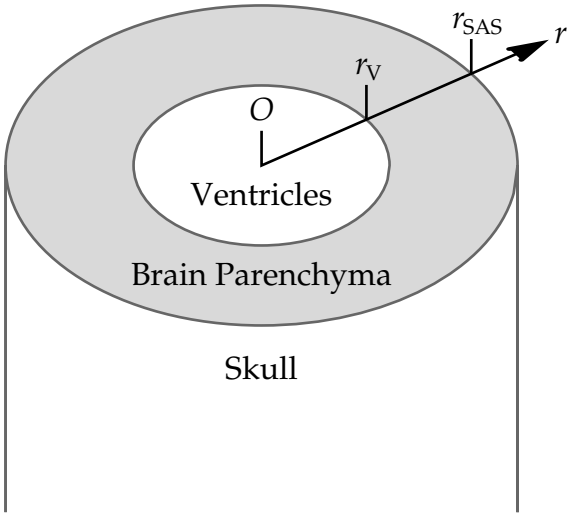

Figure 4.1: Diagram of the thick-walled cylinder model geometry.

where the total stress tensor is assumed to have the form

$$\mathbf{T}_{ij} = -p\boldsymbol{\delta}_{ij} + \boldsymbol{\tau}_{ij}. \tag{4.2}$$

Here p is the pressure of the fluid in the pores of the material, $\boldsymbol{\delta}$ is the Kronecker delta function, and $\boldsymbol{\tau}$ is the Terzaghi or "effective" stress tensor given by

$$\boldsymbol{\tau}_{ij} = \lambda \mathbf{e}_{kk}\boldsymbol{\delta}_{ij} + 2G\mathbf{e}_{ij}, \tag{4.3}$$

where Einstein's notation has been used, λ and G are the Lamé coefficients of linear elasticity for the homogenized porous medium, and $\mathbf{e}$ is the linear strain tensor defined by

$$\mathbf{e}_{ij} = \frac{1}{2}\left(\frac{\partial u_i}{\partial x_j} + \frac{\partial u_j}{\partial x_i}\right). \tag{4.4}$$

The Terzaghi stress tensor (4.3) relates the effective stress to the strain of the porous material saturated with fluid. In classical continuum mechanics, the stress tensor refers only to the solid [121]. Deformations of the fluid saturated porous material are caused by the intergranular forces of the solid. Terzaghi's effective stresses, or contact stresses, are a measure of these intergranular forces, and so deformations of the solid are determined solely by the effective stresses [127]. The fluid pore pressure acts in the fluid and in the solid equally. Therefore, the total stress is the sum of the pore-pressure-induced stress and the effective stress, as in (4.2).

Substituting (4.2), (4.3), and (4.4) into (4.1) gives the equation of motion

$$\begin{aligned}\rho\frac{\partial^2 u_i}{\partial t^2} &= \frac{\partial}{\partial x_j}\left(-p\boldsymbol{\delta}_{ij} + \lambda \mathbf{e}_{kk}\boldsymbol{\delta}_{ij} + 2G\frac{1}{2}\left(\frac{\partial u_i}{\partial x_j} + \frac{\partial u_j}{\partial x_i}\right)\right) \\ &= -\frac{\partial}{\partial x_i}p + \lambda\frac{\partial}{\partial x_i}(\nabla\cdot\vec{u}) + G\nabla^2 u_i + G\frac{\partial}{\partial x_i}(\nabla\cdot\vec{u}),\end{aligned}$$

which can be written in vector form as

$$\rho\frac{\partial^2\vec{u}}{\partial t^2} = -\nabla p + (\lambda + G)\nabla(\nabla\cdot\vec{u}) + G\nabla^2\vec{u}. \tag{4.5}$$

The Lamé elasticity coefficients represent the mechanical properties of the fluid-saturated porous solid. Initially, the development of hydrocephalus may be thought of as a loading of the brain parenchyma by an increase in ventricular pressure occurring at a constant pore pressure [121]. This situation is similar to what Biot and Willis [14] described as a jacketed test: a porous solid, contained in an impermeable jacket, is loaded by increasing external fluid pressure at a constant pore pressure. The material coefficients measured during this test are referred to as jacketed or drained quantities, although, a dry sample may not necessarily have the same properties as a saturated one [14]. Thus, the elasticity coefficients in (4.5) are jacketed quantities.

4.1.2 Darcy's Law and Mass Conservation

Darcy's Law is a phenomenologically derived equation relating fluid flow through a porous medium to the pressure gradient driving the flow. Filtration velocity, $\vec{W}$, is the velocity of the fluid relative to the solid and is given by

$$\vec{W} = -\frac{k}{\mu}\nabla p, \tag{4.6}$$

where k is the permeability of the solid (a measure of the ability of the medium to transmit fluids) and μ is the viscosity of the fluid (a measure of the resistance of a fluid to deformation under shear stress). Using (4.6), the equation of motion (4.5) becomes

$$\rho\frac{\partial^2\vec{u}}{\partial t^2} = \frac{\mu}{k}\vec{W} + (\lambda + G)\nabla(\nabla\cdot\vec{u}) + G\nabla^2\vec{u}. \tag{4.7}$$

Finally, conservation of mass requires that the continuity equation holds, that is

$$\frac{D\rho}{Dt} + \rho\nabla\cdot\vec{V} = 0,$$

where $\frac{D}{Dt}$ is the material derivative and $\vec{V}$ is the velocity of the homogenized (fluid and solid) material. Since the material is composed of elastic-solid and viscous-fluid incompressible elements, the velocity can be written as

$$\vec{V} = \vec{W} + \frac{\partial\vec{u}}{\partial t},$$

and the continuity equation becomes

$$\nabla \cdot \left(\vec{W} + \frac{\partial \vec{u}}{\partial t} \right) = 0. \tag{4.8}$$

Equations (4.7) and (4.8) form a closed system of PDEs for the displacement and filtration velocity.

Moving to the cylindrical coordinate system with planar strain, the displacement, velocity, and pressure fields reduce to depend only on the radial position r and the time t. That is, $\vec{u} = (u(r,t), 0, 0)$, $\vec{W} = (W(r,t), 0, 0)$ and $p = p(r,t)$. An expression for the filtration velocity, $W(r,t)$, can be found by integrating the continuity equation (4.8), giving

$$W(r,t) = \frac{1}{r} c_0(t) - \frac{\partial u}{\partial t}(r,t), \tag{4.9}$$

where $c_0(t)$ is an arbitrary function of time.

The pore pressure is assumed to have a static (constant) and a dynamic (time and space dependent) component, $p(r,t) = p_s + p_d(r,t)$. Using Darcy's Law (4.6) and the expression for filtration velocity (4.9) gives

$$\nabla p_d(r,t) = -\frac{\mu}{k} W(r,t) = -\frac{\mu}{k} \left(\frac{1}{r} c_0(t) - \frac{\partial u}{\partial t}(r,t) \right). \tag{4.10}$$

The equation for pressure (4.10) and the equation of motion (4.7), written in cylindrical coordinates, give the following coupled system of PDEs which govern the displacement of the homogenized solid and the dynamic pore pressure

$$\frac{\partial^2 u}{\partial t^2} + f_r \frac{\partial u}{\partial t} = f_r \frac{1}{r} c_0(t) + {c_d}^2 \left(\frac{\partial^2 u}{\partial r^2} + \frac{1}{r} \frac{\partial u}{\partial r} - \frac{1}{r^2} u \right) \tag{4.11}$$

and

$$\frac{\partial p_d}{\partial r} = \frac{\mu}{k} \left(\frac{\partial u}{\partial t} - \frac{1}{r} c_0(t) \right), \tag{4.12}$$

where $f_r = \frac{\mu}{\rho k}$ is the relaxation frequency and $c_d = \sqrt{\frac{\lambda + 2G}{\rho}}$ is the propagation speed of the dilatational waves.

4.1.3 Boundary Conditions

Boundary conditions are required to determine the arbitrary constants and functions that arise in the solutions to the above system of PDEs, (4.11) and (4.12). For dynamic pore pressure, we require the amplitude of the parenchyma pressure pulsations at the ventricle boundary ($r = r_V$) to match the amplitude of the ventricular CSF pulsations (p_V). Similarly, the amplitude of the parenchyma pressure pulsations at the SAS boundary ($r = r_{SAS}$) must match the amplitude

of the SAS CSF pulsations (p_{SAS}). Assuming the pressure waves have angular frequency ω, the boundary conditions for the pore pressure are

$$\begin{cases} p_d(r_V, t) = \mathrm{Re}\left(p_V \mathrm{e}^{i\omega t}\right) \\ p_d(r_{SAS}, t) = \mathrm{Re}\left(p_{SAS} \mathrm{e}^{i\omega t}\right). \end{cases} \tag{4.13}$$

Boundary conditions for the displacement are a bit more complicated. Since the parenchyma effectively sits in a fluid filled container, there should be no contact stress in the poroelastic solid at the ventricular and SAS boundaries. This requires enforcing

$$\begin{cases} \left[(\lambda + 2G)\frac{\partial u}{\partial r} + \frac{\lambda}{r}u\right]_{r=r_V} = 0 \\ \left[(\lambda + 2G)\frac{\partial u}{\partial r} + \frac{\lambda}{r}u\right]_{r=r_{SAS}} = 0. \end{cases} \tag{4.14}$$

We solve equations (4.11) and (4.12) by assuming that the solutions are harmonic with frequency ω and have the following forms

$$\begin{aligned} u(r,t) &= \mathrm{Re}\left(U(r)\mathrm{e}^{i\omega t}\right), \\ p_d(r,t) &= \mathrm{Re}\left(P(r)\mathrm{e}^{i\omega t}\right), \\ c_0(t) &= \mathrm{Re}\left(C_0\mathrm{e}^{i\omega t}\right). \end{aligned}$$

Substituting the harmonic forms into the PDEs and solving, the details of which are described in Appendix A, gives $U(r)$ and $P(r)$ as

$$U\big(\xi(r)\big) = -\frac{1}{c_d\alpha\xi}C_0 + \frac{c_d}{f_r}\big(C_1J_1(\xi) + C_2Y_1(\xi)\big), \tag{4.15}$$

$$P\big(\xi(r)\big) = -\frac{\omega^2\mu\ln(\frac{1}{\alpha}\xi)}{kf_r^2\alpha^2}C_0 - \frac{i\omega\mu c_d^2}{kf_r^2\alpha}\big(C_1J_0(\xi) + C_2Y_0(\xi)\big) + \mu f_r C_3, \tag{4.16}$$

where $\alpha = \sqrt{\frac{\omega^2}{f_r^2} - i\frac{\omega}{f_r}}$, $\xi(r) = \frac{\alpha f_r}{c_d}r$, and J_n and Y_n are the Bessel Functions of order n. The constants C_0, C_1, C_2, and C_3 are determined by the boundary conditions and can be found by solving the matrix equation $\mathbf{A}\vec{x} = \vec{b}$, where

$$\begin{aligned} \vec{x} &= [\ C_0 \quad C_1 \quad C_2 \quad C_3\ ]^T, \\ \vec{b} &= [\ p_V \quad p_{SAS} \quad 0 \quad 0\ ]^T, \end{aligned}$$

and the matrix $\mathbf{A}$ is

$$\mathbf{A} = \begin{bmatrix} \frac{-\omega^2\mu\ln(\frac{\xi_V}{\alpha})}{kf_r^2\alpha^2} & \frac{-i\omega\mu c_d^2}{\alpha k f_r^2}J_0^V & \frac{-i\omega\mu c_d^2}{\alpha k f_r^2}Y_0^V & \mu f_r \\ \frac{-\omega^2\mu\ln(\frac{\xi_{SAS}}{\alpha})}{kf_r^2\alpha^2} & \frac{-i\omega\mu c_d^2}{\alpha k f_r^2}J_0^{SAS} & \frac{-i\omega\mu c_d^2}{\alpha k f_r^2}Y_0^{SAS} & \mu f_r \\ \frac{f_r}{\alpha c_d^2\xi_V} & \frac{M\xi_V}{2G}J_0^V - J_1^V & \frac{M\xi_V}{2G}Y_0^V - Y_1^V & 0 \\ \frac{f_r}{\alpha c_d^2\xi_{SAS}} & \frac{M\xi_{SAS}}{2G}J_0^{SAS} - J_1^{SAS} & \frac{M\xi_{SAS}}{2G}Y_0^{SAS} - Y_1^{SAS} & 0 \end{bmatrix},$$

where $M = (\lambda + 2G)$, $\xi_V = \frac{\alpha f_r}{c_d} r_V$, $\xi_{SAS} = \frac{\alpha f_r}{c_d} r_{SAS}$, and the notation $\mathcal{F}_n^B = \mathcal{F}_n(\frac{\alpha f_r}{c_d} r_B)$ with $n = 0$ or 1, $B = V$ or SAS, and $\mathcal{F} = J$ or Y, has been used for convenience. Finally, the filtration velocity can be found from (4.9) as

$$W(r,t) = \frac{1}{r}\,\mathrm{Re}\left(C_0 \mathrm{e}^{i\omega t}\right) - \mathrm{Re}\left(i\omega U(r)\mathrm{e}^{i\omega t}\right). \tag{4.17}$$

4.2 Numerical Simulations

The values of C_0, C_1, C_2, and C_3 are expressed in terms of nonlinear combinations of the Bessel functions J_0, J_1, Y_0, and Y_1. To numerically simulate the solutions for displacement, filtration velocity, and pressure, the asymptotic expansions for the Bessel functions with large arguments [1] are used and simplifications are made using the forms of the cross-product terms. For details on the numerical computations, including the `MAPLE` code used to compute the solutions, see Appendix A.

Model parameter values are chosen to represent a typical normal pressure hydrocephalic brain. Thus, the average pressure is defined to be normal at 13 mm Hg, but the CSF wave amplitudes are defined to be large at 9.4 and 9.0 mm Hg peak-to-peak at the ventricle wall and cortical surface, respectively. The amplitude difference of 0.2 mm Hg was chosen since it is the smallest measured difference between the ventricular and parenchymal pressures reported by Eide [35]. We will discuss the effect of larger amplitude differences later in this Chapter.

The pressure amplitude prescribed at the outer boundary was chosen to be the same as the pressure amplitude measured in the parenchyma. This choice is justified by the measurements reported by Eide [34] in which no significant difference in wave amplitude was observed between the parenchyma and epidural space. Table 4.1 lists the values of the model parameters used in the numerical simulations. Note that the Lamé coefficients have been replaced by the Young's modulus, E, and Poisson ratio, ν, via the relationships

$$G = \frac{E}{2(1+\nu)} \quad \text{and} \quad \lambda = \frac{E\nu}{(1+\nu)(1-2\nu)}.$$

With these parameter values, the poroelastic model predictions for the pore pressure at the ventricle wall ($r = r_V$), in the middle of the parenchyma ($r = r_m$), and at the cortical surface ($r = r_{SAS}$) are shown in Figure 4.2.

The maximum pressure predicted at the ventricle wall is 17.7 mm Hg, at the SAS boundary it is 17.5 mm Hg, and in the middle of the parenchyma it is 17.48 mm Hg. These model predictions match the finding of Eide [35, 34] wherein a dynamic pressure gradient across the ventricle wall into the parenchyma was observed as well as no significant pressure difference between the parenchyma and the SAS. The pressure gradient from the ventricle to the parenchyma is dynamic, or oscillatory, since in systole the pressure is higher in the

Table 4.1: Parameter values for the poroelastic model representing a normal pressure hydrocephalic brain.

$\mu = 10^{-3}$ Kg m^{-1}s^{-1}	$\rho = 10^{3}$ Kg m^{-3}	$k = 10^{-14}$ m^2 [59]
$E = 21$ kPa [121]	$\nu = 0.4$ [121]	$\omega = 6$ rad s^{-1}
$p_V = \frac{1}{2}9.4$ mm Hg	$p_{SAS} = \frac{1}{2}9.0$ mm Hg	$p_s = 13$ mm Hg
$r_V = 3$ cm	$r_{SAS} = 10$ cm	$r_m = 6.5$ cm

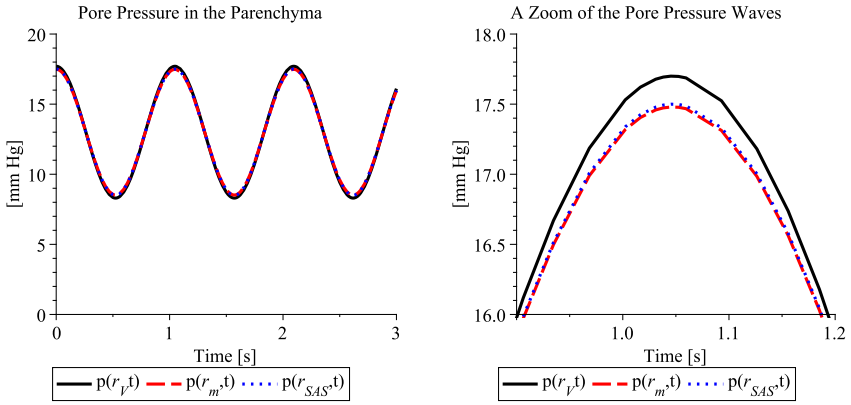

(a) **(b)**

Figure 4.2: Predicted pressure waves in the brain parenchyma at the ventricle wall, in the middle of the parenchyma, and at the cortical surface (a), and a zoom of a systolic peak showing the curve separations (b).

ventricle while in diastole the pressure is higher in the parenchyma. These oscillatory changes in pressure cause the parenchyma to be displaced in a pulsatile manner as shown in Figure 4.3

In systole, the pressure is largest in the ventricle which causes an outward displacement of the parenchyma. The pressure gradient reverses in diastole which results in an inward displacement of the parenchyma. This oscillatory displacement is largest near the ventricle, with a maximum amplitude of 58.8 μm, compared to the maximum displacement amplitude in the middle of the parenchyma, 27.2 μm, or the SAS boundary, 17.7 μm. At any given time, the magnitude of the displacement is greatest at the ventricle boundary and least at the SAS boundary.

The oscillatory pressure gradient and the resulting compression and expansion of the brain parenchyma cause movement of the fluid in and out of the parenchyma at both boundaries, see Figure 4.4. The filtration velocity leads the displacement and pressure waves in phase due to the conflict between the pressure gradient and the compressed or expanded parenchyma, see Figure 4.3b. When the ventricular pressure increases from the average pressure, the pressure

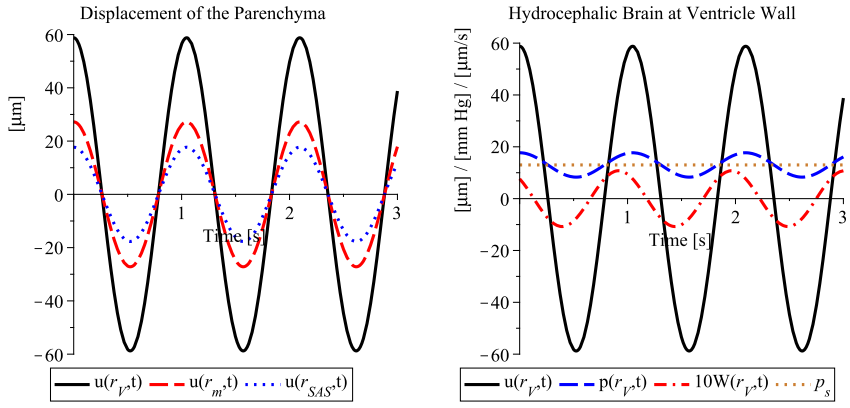

Figure 4.3: Predicted displacement of the brain parenchyma at the ventricle wall, in the middle of the parenchyma, and at the cortical surface (a), and the displacement, pressure, and filtration velocity (scaled to be clearly visible) at the ventricle wall demonstrating the phase differences between the curves (b).

gradient pushes fluid into the parenchyma and it also compresses the parenchyma by displacing it outwards. The resulting compression forces fluid out of the parenchyma into the ventricle. Before the pressure reaches the systolic maximum, the parenchyma becomes compressed enough to resist the flow with enough force to slow the inward flow driven by the pressure gradient. The flow velocity thus peaks before the pressure and displacement waves peak. When the pressure gradient and parenchyma fluid expulsion forces balance, the flow reverses and fluid begins exiting the parenchyma into the ventricle. In diastole, the ventricular pressure drops and the parenchyma expands, and again these two mechanisms compete to control the fluid flow.

Away from the complex filtration at the boundaries, the fluid flow in the middle of the parenchyma is small, obtaining a maximum velocity of approximately 10 pm/s. Figure 4.4 shows the filtration velocity at three points in the parenchyma. The velocity at the cortical surface is completely out of phase with the velocity at the ventricle wall, which is consistent with the directions of the intramantle pressure gradients from the ventricle to the parenchyma and from the SAS to the parenchyma. The highest filtration velocities are seen near the ventricle wall and have a maximum magnitude of approximately 1 μm/s.

4.2.1 Parameter Sensitivity Analysis

The previous numerical simulations used parameter values describing a normal pressure hydrocephalic brain. By reducing the peak-to-peak wave amplitudes in the ventricle and SAS to 5.4 and 5.0 mm Hg, respectively, the same numerics

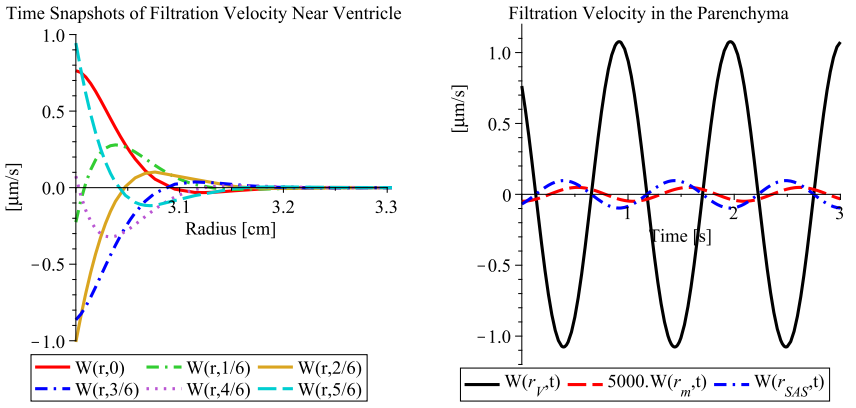

Figure 4.4: Filtration velocity time snapshots in the periventricular tissue (a), and the filtration velocity at the ventricle wall, in the middle of the parenchyma (scaled to be clearly visible), and at the cortical surface (b).

can be used to predict the behaviour of a normal brain. Similarly, by increasing the average pressure to 20 mm Hg, the same numerics can be used to predict the behaviour of an active hydrocephalic brain. Reducing the amplitude of the pressure waves or increasing the average pressure as suggested above, however, has no affect on the model predictions. The displacement and filtration are only dependent on the dynamic pressure gradient caused by the difference between the wave amplitudes of the ventricular and SAS pressures. For instance, if $p_V = p_{SAS}$, then no oscillatory pressure gradient exists and the entire poroelastic material is suspended in a container with a hydrostatic pressure of $p_s + p_V \cos(\omega t)$ mm Hg. Since the hydrostatic pressure acts equally everywhere on and throughout the pores of the material, no displacements or filtration will occur.

Using pressure parameter values that describe a normal brain ($p_s = 13$, $p_V = \frac{1}{2}5.4$, and $p_{SAS} = \frac{1}{2}5.0$ mm Hg), a parameter sensitivity analysis can be conducted to investigate the effect that variations in the elastic constants, the permeability, and the oscillatory pressure gradient, have on the maximum displacement of the parenchyma. The Young's modulus, E, is varied from 500 to 10^6 Pa and the predicted maximum displacements of the ventricle wall, the middle of the parenchyma, and the cortical surface are shown in Figure 4.5a. The Young's modulus of brain parenchyma was estimated by Tenti *et al.* [121] to be about 21 000 Pa. Taylor and Miller [120] estimated the steady-state elastic modulus of the brain to be about 584 Pa for small strain-rate deformations such as hydrocephalus. As the Young's modulus decreases from 21 000 Pa to 500 Pa, the displacement of the parenchyma increases by about two orders of magnitude. For a Young's modulus of 500 Pa, the poroelastic model predicts that the brain parenchyma compresses by about 2 mm during each systolic peak in pressure.

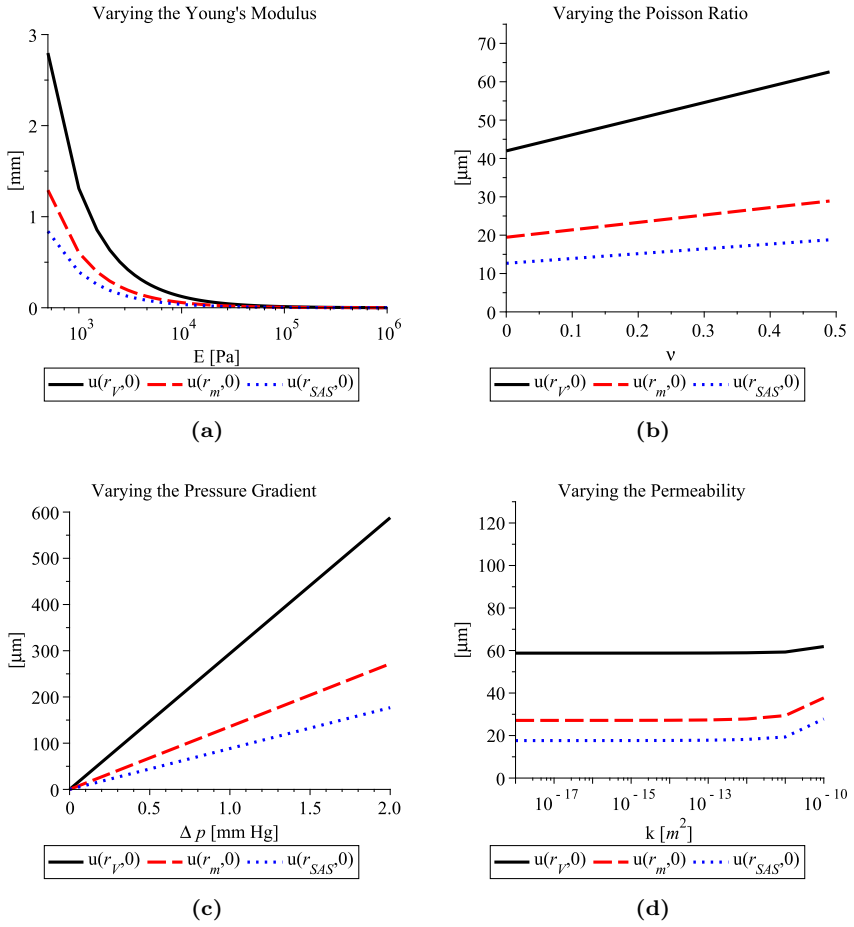

Figure 4.5: Maximum displacement in the parenchyma as the Young's modulus (a), the Poisson ratio (b), the oscillatory pressure gradient (c), and the permeability (d) are varied.

In Figure 4.5b the Poisson ratio is varied from 0 to 0.49, to avoid the well-known numerical instability associated with a Poisson's ratio of 0.5. Variations in the Poisson ratio have a negligible effect on the maximum displacement of the parenchyma. Figure 4.5c shows that the maximum displacement increases linearly with the dynamic pressure difference, $\Delta p = p_V - p_{SAS}$. And Figure 4.5d shows that changes in the permeability have little effect on the displacement until the order of magnitude of 10^{-10} m^2 is reached. Estimates of the permeability of brain tissue are on the order of 10^{-16} to 10^{-14} m^2 [59, 84], so this larger value of permeability does not lie within the physical range of values.

4.2.2 Pore Flow Analysis

The maximum pore velocity predicted by the poroelastic model for flow near the ventricle wall, assuming a 0.4 mm Hg peak-to-peak pressure wave amplitude difference between the ventricles and the SAS, was about 1 μm/s. To determine if this shear flow is sufficient to damage the tissue cells, we use a simple pipe flow model. By assuming the fluid is Newtonian, incompressible, and steady, and by neglecting body forces, the Navier-Stokes equations simplify to the following equation for flow through a straight pore,

$$\nabla q = \mu \nabla^2 v, \tag{4.18}$$

where ∇q is the constant pressure gradient across the length of the pore, μ is the fluid viscosity, and v is the fluid flow along the pore. In a cylindrical pore $v = v(r)$, and the flow is given by

$$v(r) = \frac{\nabla q}{4\mu}(r^2 - R^2), \tag{4.19}$$

where R is the radius of the pore and the following boundary conditions are imposed, $v(R) = 0$ and $\frac{\mathrm{d}v}{\mathrm{d}r}|_{r=0} = 0$.

Since the fluid flow through the porous material is governed by both the pressure gradient and the compression or expansion of the material, the pressure gradient used in this pore flow model, ∇q, is different from the pressure gradient in the poroelastic model. Thus, to determine the pressure gradient ∇q, we require the maximum velocity through the pore to be 1 μm/s. This provides an over approximation of the pressure gradient, $\nabla q = -1.6$ Pa, assuming a 100 μm diameter pore. The flow through the pore is thus given by

$$v(r) = 400(R^2 - r^2), \tag{4.20}$$

where the viscosity of water, $\mu = 10^{-3}$ Pa·s, is assumed. Finally, the shear stress induced on the walls of the pore by a steady flow with a maximum velocity of 1 μm/s is given by

$$\sigma = \mu \left.\frac{\mathrm{d}v}{\mathrm{d}r}\right|_{r=R} = -40 \ \mu\text{Pa}. \tag{4.21}$$

Cells adhere to the extracellular matrix through the binding of integrin receptors to ligands such as fibronectin or collagen. Measurements of cell adhesion strength using shear flows in microfluidic channels average about 84 ± 27 Pa for cells adhered to low concentration collagen- or fibronectin-coated substrates [18]. The smallest observed adhesion strength was about 30 Pa and the largest observed strength was about 210 Pa. This is the force required to completely remove a cell from the substrate. Dong and Lei [26] estimated the force required to rupture one adhesive bond, or to extract a receptor from the cell membrane, as 1 μdyn (or 10^{-11} N). To estimate the shear, we assume this force is distributed over the top half of a cell attached to the pore wall. This provides a lower bound to the shear generated by this force acting directly on the smaller

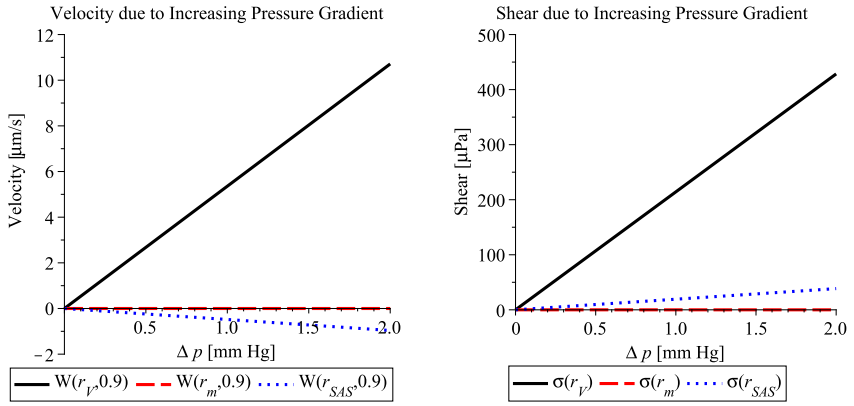

Figure 4.6: Maximum filtration velocity in the parenchyma (a) and the corresponding magnitude of the shear applied to the pore walls (b) as the oscillatory pressure gradient between the ventricles and SAS is varied.

area of an integrin binding site. Assuming a spherical cell of radius 5 μm (the soma of a neuron ranges from 4 to 100 μm in diameter), this force corresponds to a surface shear of about 0.06 Pa. The estimated shear stress imposed by the fluid flow in the periventricular region was about 40 μPa, which is three orders of magnitude smaller than the estimated stress required to break a single adhesive bond.

Figure 4.6a shows the maximum filtration velocity at the ventricle wall, in the middle of the parenchyma, and at the cortical surface as the pressure wave amplitude difference between the ventricles and SAS, $\Delta p = p_V - p_{SAS}$, is increased. Positive velocities represent flow away from the ventricles and negative velocities represent flow towards the ventricles. Figure 4.6b shows the corresponding shear stress magnitude imposed on the wall of a cylindrical pore of radius 50 μm at each of these positions in the parenchyma. The pore pressure gradient ∇q was chosen by requiring the maximum filtration velocity to occur at the centre of the pore for each increment in Δp and for each position in the parenchyma. Even with a 2 mm Hg difference in wave amplitude (4 mm Hg peak-to-peak) the maximum filtration velocity at the ventricle wall is only about 11 μm/s and the shear force is only about 450 μPa. This shear force is still two orders of magnitude smaller than the shear estimated to rupture a single adhesive bond.

4.3 Discussion

The mathematical model presented in this Chapter incorporates the oscillations of CSF into the poroelastic model developed by Tenti *et al.* [121]. The amplitude of the oscillations were chosen to match measurements obtained by Eide [35, 34] from hydrocephalic patients. Maximum displacements, about 60 μm, and maximum filtration velocities, about 1 μm/s, were predicted to occur at the ventricle wall. The displacement was found to be in phase with the pressure pulsations throughout the parenchyma while the filtration velocity was found to lead the pressure wave at the ventricle wall.

From the parameter sensitivity analysis conducted in Section 4.2.1, we can conclude that the Young's modulus and the dynamic pressure gradient are the most significant parameters in the poroelastic model. Measurements of the difference between the ventricular and parenchymal pressure pulsations in hydrocephalic patients ranged from 0.4 to 2.6 mm Hg peak-to-peak [35]. From the predictions of this model, the ventricle wall would displace 60 to 600 μm, respectively, which is an increase by one order of magnitude. Decreasing the Young's modulus from the value estimated by Tenti *et al.* [121], 21 kPa, to the value determined by Taylor and Miller [120], 584 Pa, increases the displacement of the ventricle wall by almost two orders of magnitude.

No difference in displacement or filtration is predicted by this model for changes in the average pressure or the amplitude of the oscillations, provided the wave amplitude difference between the ventricles and the SAS remains constant. As the difference between these two wave amplitudes increases, however, the displacement and filtration both increase. The cyclic compression and expansion that the brain tissue undergoes along with the corresponding inflow and outflow of fluid cause larger than normal shear forces to act on the cells of the ependyma (the lining of the ventricles) and on the cells of the parenchyma close to the ventricles.

In hydrocephalus, the cells of the ependyma are observed to be flattened and stretched, changing from cylindrical and heavily ciliated to cubic with few cilia, and disruptions or gaps are observed in the ependyma lining [101]. To determine the potential of the fluid filtration to cause this damage, we developed a model for flow along a pore of the parenchyma, and estimated the shear force induced on the parenchyma by the filtration. Near the ventricle wall, where the filtration velocity peaks at about 1 μm/s, the shear applied to the pore walls was estimated to be 40 μPa. This is significantly smaller than our estimate of the shear required to break a single adhesion bond, 0.06 Pa, based on the experimental work of Dong and Lei [26]. This analysis indicates that the fluid filtration causes negligible damage to the parenchyma; however, this analysis ignored parenchymal absorption which would increase the fluid filtration through the tissue. Also, the effects of oscillatory shear flows on cell adhesion may differ from steady shear flows, and cell adhesion strength may depend on the substrate used in the experiments (most experiments use collagen which is not found in abundance in brain ECM); to the best of our knowledge, these effects have yet

to be investigated. Nevertheless, since the fluid filtration predicted here causes only negligible shearing on the tissue, only the cyclic compression and stretching of the periventricular area remains as a possible mechanism for the damage observed in hydrocephalus. The compressive and expansive forces are induced by unbalanced pressure wave amplitudes between the ventricles and the parenchyma or SAS, but it remains to be determined how the pulse amplitude in the ventricle becomes increased in the first place.

As was shown in Chapter 3, the amplitude of the CSF pulsations increases as the compliance of the cranium decreases. Mimicking this apparent stiffening of the brain tissue by increasing the Young's modulus, however, reduces the effect of the pulsations by decreasing the resulting displacements. Using the value of the Young's modulus determined by Taylor and Miller [120], 584 Pa, we obtain a prediction of 2 mm of parenchymal compression compared to the 40 μm predicted using the value estimated by Tenti *et al.* [121], 21 kPa. If, for example, the microstructure of brain tissue was somehow altered, causing the Young's modulus to decrease to the value estimated by Taylor and Miller, then the unbalanced pressure pulsations that act on the brain may be more significant to the development of the cellular damage and ventricular enlargement observed in hydrocephalus.

The combined effect of an increased pressure wave amplitude in the ventricles and a reduced Young's modulus will cause larger than normal shear forces to occur in the periventricular area. It should be noted, however, that once a shunt is surgically inserted and CSF is siphoned off into another region of the body, the brain responds by returning, approximately, to it's original shape. With successful shunt treatment, the brain parenchyma is no longer displaced outward into the skull and many, if not all, of the symptoms of hydrocephalus are resolved.

The damage theory of hydrocephalus is based on the assumption that the cellular damage caused by the pulsations induces biological changes in the living tissue, and that these changes permit the parenchyma to be deformed outward. With shunt insertion, the pressure waves of the CSF may be initially truncated due to the opening threshold of the shunt. This truncation would reduce the pulse amplitude of the CSF pressure and reduce the oscillatory motion of the parenchyma. Furthermore, the shunt may also increase the compliance of the cranium by providing another mechanism for CSF removal. Increasing the compliance would decrease the pulse amplitude of the ventricular CSF. The degraded mechanical properties of the tissue may then allow the tissue to return, approximately, to it's original shape. Initially, the tissue may be stretched, but over time, the living cells would respond to this mechanical stimulus and relax into the new arrangement.

If hydrocephalus is caused by a combination of a reduced intracranial compliance (to increase the ventricular pressure wave amplitudes) and a decreased Young's modulus (to enhance the effect that the pulsations have on the parenchyma), then two questions arise. First, what causes the cranial compliance to decrease prior to the development of hydrocephalus? Or, if this is not the rea-

son for the unbalanced ventricular and SAS pressure waves, then what causes the ventricular pressure wave amplitudes to increase? The second question that must be raised is what cellular or chemical changes occur in the tissue to decrease the Young's modulus, making the tissue more susceptible to deformation.

The promising work by Johnston and coworkers [86] provides possible answers to these questions by suggesting a new molecular mechanism that causes the development of intramantle pressure gradients and hydrocephalus. Recall that they were able to induce hydrocephalus in rats by injecting antibodies to β_1-integrins into the ventricles. Amongst other functions, integrins play a key role in the structural integrity of brain tissue; they protrude from cell membranes to adhere the cell to the surrounding extracellular matrix. The antibodies block the binding sites of the integrins which, at a macroscopic scale, is hypothesized to reduce the structural integrity of the tissue, decreasing the Young's modulus, and causing the pore pressure to decrease [9], thus partially creating the necessary conditions discussed above for ventricular expansion.

Chapter 5

A Viscoelastic Analysis of CSF Pulsations and Hydrocephalus

In the previous Chapter, a poroelastic model was developed to determine the effect of CSF pulsations on the development of hydrocephalus. With respect to the pulsation-damage theory of ventricular enlargement, the fluid filtration resulting from the CSF pulsations was found to be negligible compared to the shear stress required to damage tissue at the cellular level. Thus, it is not necessary to consider the fluid phase of brain tissue when investigating the periodic loading caused by CSF pulsations and the possible link to the development of hydrocephalus. Therefore, in this Chapter we present an analysis of the effect of periodic loading on the brain parenchyma using a viscoelastic approach to determine if these pulsations have any significant role in the genesis and evolution of hydrocephalus.

The mechanical behaviour of brain tissue should be modelled differently for different experimental conditions, and in particular, the magnitude of the strain rate should be considered when choosing a mechanical model. Specifically, poroelastic models cannot account for the strong strain-rate dependence observed in the behaviour of brain tissue, but this intrinsic viscoelasticity only influences the short-term response as the effect dissipates over time [17]. Thus, different constitutive relations may be required for the same material depending on the experimental conditions being modelled [61]. The behaviour of brain tissue under impacts, such as the periodic loading due to CSF pulsations, may be better suited to an incompressible viscoelastic approach. In contrast, a poroelastic approach may be better suited to long-time processes where material compressibility results from consolidation effects.

Many linear and nonlinear viscoelastic constitutive equations have been proposed for brain tissue [23, 75, 78, 79, 80, 90, 129]. Sivaloganathan *et al.* [113]

developed a model of hydrocephalus based on the standard linear viscoelastic model and then extended it to include pulsatile ventricular pressure [114]. They found that when both the dilatational and deviatoric effects are assumed to be viscoelastic, the ability to determine model parameters from experimental data is lost due to the large number, and lack of physical interpretations, of these parameters.

The first fractional derivative constitutive models in linear viscoelasticity were proposed by Bagley and Torvik [4, 5, 6] and Rogers [103]: these models were shown to predict adequately the behaviour of polymers. Since then, fractional order models have been shown to describe accurately the creep and relaxation processes in polymeric materials [5, 53], and to characterize the effect of vibrations in the response of viscoelastically damped materials [4, 119]. Fractional order constitutive models have also been shown to incorporate the stochastic (micro-Brownian) motion of chain molecules at the microscopic level into the macroscopic description of the material, and in fact, it has been shown that these models can be derived directly from the molecular theory for polymer solutions [5]. From the observation that brain tissue behaves qualitatively similar to rubber-like materials [40], the success of these models has led to the application of fractional viscoelastic models to describe the mechanical behaviour of brain tissue [23, 66, 132].

Viscoelastic models based on frational calculus arose from the observation that the stiffness and damping properties of viscoelastic materials are proportional to fractional powers of frequency [5]. This observation leads directly to the use of fractional derivatives via the Fourier Transform. Bagley and Torvik [6] developed conditions for the fractional orders of a viscoelastic constitutive equation based on thermodynamic arguments to ensure that the resulting model predicts a non-negative rate of energy dissipation and a non-negative internal work. Later work by Heymans and Bauwens [53] showed that if the constitutive equation is derived directly from a fractional rheological model, where the viscous first order derivative terms are replaced by fractional order derivative terms, then these requirements are automatically satisfied.

The significant difference between integer and fractional order derivatives is that fractional derivatives are non-local operators. The entire history of a causal function is required to determine the fractional derivative via the convolution with a fading memory function. The main advantage of fractional viscoelastic models is the relatively small number of model parameters required to describe adequately the behaviour of polymer-like materials. For example, no relaxation spectrum is required since the model incorporates this type of complexity through only one characteristic time and the fractional differential operator [53]. The physical interpretation of fractional differentiation is still an open question, although one attempt has been made by Podlubny [96] who used two different kinds of time to relate the meaning of fractional derivatives to the meaning of first order derivatives.

Due to the reported success of the fractional Zener viscoelastic model in predicting the creep and relaxation of brain parenchyma [23], we chose this model

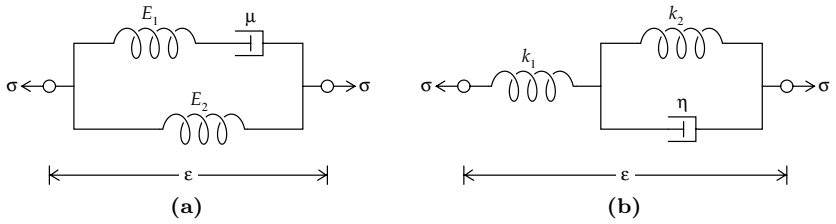

Figure 5.1: Schematics of the Zener viscoelastic model (a) and the standard viscoelastic model (b).

to describe the hydrocephalic brain in the following analysis on the effect of ventricular pulsations. We solve the boundary value problems analytically, for both infant and adult hydrocephalus, and use numerical simulations to demonstrate that the displacement waves arising in adult parenchyma are small in comparison to the displacement waves that present in infant parenchyma. The Chapter concludes with a description of a possible link between parenchyma age and the order of the fractional derivative.

5.1 Fractional Zener Model Formulation

Inspired by the success of fractional order viscoelastic models at predicting the behavior of polymers, Davis *et al.* [23] showed that the fractional Zener linear viscoelastic model performs better than other three- or four-parameter linear viscoelastic models at characterizing the creep and relaxation of brain parenchyma when compared to the experimental data reported by Galford and McElhaney [43]. This may be due to the temporal multi-scaling effect of the fractional order derivative found in the constitutive equation [28, 96]. By definition, the Riemann-Liouville fractional derivative of order α, $0 < \alpha < 1$, of a causal function $f(t)$ is:

$$D^{\alpha} f(t) = \frac{1}{\Gamma(1-\alpha)} \frac{\mathrm{d}}{\mathrm{d}t} \int_0^t (t-s)^{-\alpha} f(s) \mathrm{d}s, \tag{5.1}$$

where $\Gamma(a) = \int_0^{\infty} \mathrm{e}^{-x} x^{a-1} \mathrm{d}x$ is the Eulerian gamma function.

The Zener viscoelastic model consists of an elastic spring, E_1, and a viscous dashpot, μ, in series, all in parallel with another elastic spring, E_2. A diagram of the Zener viscoelastic model is provided in Figure 5.1a. The constitutive equation of the fractional Zener model is:

$$\sigma(t) + \tau^{\alpha} D^{\alpha} \sigma(t) = E_{\infty} \epsilon(t) + E_0 \tau^{\alpha} D^{\alpha} \epsilon(t), \tag{5.2}$$

where $\sigma(t)$ is the stress at time t, $\epsilon(t)$ is the strain at time t, $\tau = \mu / E_1$ is the relaxation time, $E_0 = E_1 + E_2$ is the initial elastic modulus, and $E_{\infty} = E_2$ is the steady-state elastic modulus.

In this Chapter we extend the work presented in [114] by modelling the brain as a homogeneous, incompressible, isotropic, linear viscoelastic solid that obeys the fractional Zener constitutive law. The brain geometry is simplified as a thick-walled tethered cylinder, hence strain can be assumed to be planar. Following [114] and [121], we assume a cylindrical geometry for the brain. Apart from the resulting simplification to one spatial dimension, more amenable to analytic methods, this choice of geometry was motivated by the observation of J. Drake (Chief Neurosurgeon, Hospital for Sick Children, Toronto) [27] that the ventricular configuration in fully developed hydrocephalus is more akin to a cylindrical geometry than a spherical geometry. Nevertheless, this choice does not significantly alter the results and conclusions of this work.

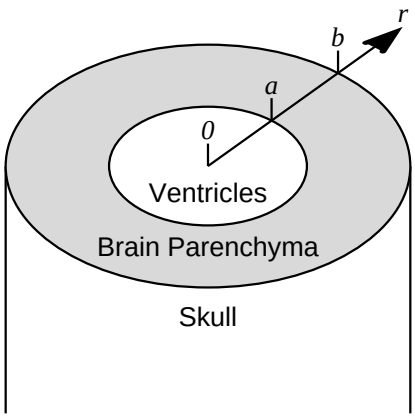

Figure 5.2: Diagram of the simplified cylindrical geometry of the brain.

The inside of the thick-walled cylinder represents the cerebral ventricles, the thick wall represents the brain parenchyma, and the outside represents the subarachnoid space and skull, Figure 5.2. The inner boundary represents the ventricular wall and this is subjected to a pulsatile pressure due to the rhythmic pumping of the heart. The outer boundary represents the cortical surface and is subjected to either a stress-free boundary condition (for infant hydrocephalus where the skull is not yet fixed) or zero displacement (for adult hydrocephalus where the skull is rigid).

We assume that the deviatoric parts of the stress and strain tensors behave according to the fractional Zener constitutive law, and that the dilatational parts obey Hooke's law of linear elasticity. The boundary value problems are then solved and the analytic solutions for the displacement and stress fields are shown to be generalizations of the solutions obtained by Sivaloganathan *et al.* [114], where the brain was modelled as a standard viscoelastic solid, see Figure 5.1b.

5.1.1 Infant Hydrocephalus

Following the approach of Sivaloganathan *et al.* [114], the problem of infant hydrocephalus requires solving the equation of motion,

$$\frac{\partial}{\partial r}\sigma_{rr} + \frac{1}{r}(\sigma_{rr} - \sigma_{\theta\theta}) = 0, \tag{5.3}$$

subject to the boundary conditions

$$\sigma_{rr} = -p_i \quad \text{at} \quad r = a \qquad \text{and} \qquad \sigma_{rr} = 0 \quad \text{at} \quad r = b, \tag{5.4}$$

where p_i is the difference between the ventricular CSF pressure and the subarachnoid space CSF pressure. The zero-stress boundary condition (as used in [64, 114, 121]) is a weak condition which avoids the much more complex free boundary value problem. We assume that the infant brain is encased in a thin elastic membrane representing the soft skull, cartilage, and skin. Since large deformations to this elastic membrane, in an infant with hydrocephalus, occur very slowly over large time scales, and the analysis presented in this Chapter is done for short time scales (on the order of the heart beat), this zero-stress boundary condition is valid.

In the linear elastic case, the boundary value problem (5.3)-(5.4) has the well known solution [38]:

$$\begin{cases} u(r,t) = p_i(t)\left(\frac{a^2}{b^2-a^2}\right)\left(\frac{1+\nu}{E}\right)\left((1-2\nu)r + \frac{b^2}{r}\right) \\ \sigma_{rr}(r,t) = p_i(t)\frac{a^2}{b^2-a^2}\left(1 - \frac{b^2}{r^2}\right) \\ \sigma_{\theta\theta}(r,t) = p_i(t)\frac{a^2}{b^2-a^2}\left(1 + \frac{b^2}{r^2}\right). \end{cases} \tag{5.5}$$

To determine the solution to (5.3) for the viscoelastic case, the elastic-viscoelastic Correspondence Principle is used. We first rewrite the constitutive equation (5.2) as

$$P\sigma = Q\epsilon, \tag{5.6}$$

where P and Q are differential operators of the form

$$P = p_0 + \sum_{j=0}^{n} p_{j+1} D^{j+\alpha}, \qquad Q = q_0 + \sum_{j=0}^{n} q_{j+1} D^{j+\alpha},$$

with material parameters p_j and q_j.

By letting s_{ij} and d_{ij} be the deviatoric stress and strain tensors and σ_{ii} and ϵ_{ii} be the dilatational stress and strain tensors, we can rewrite (5.6) as

$$P_1 s_{ij} = Q_1 d_{ij}, \qquad \text{and} \qquad P_2\sigma_{ii} = Q_2\epsilon_{ii}. \tag{5.7}$$

Assuming that the deviatoric response of the brain is described by a fractional Zener viscoelastic model and the dilatational response of the brain is described

by a linear elastic model, the differential operators in (5.7) have the following forms:

$$\begin{aligned} P_1 &= 1 + \tau^\alpha D^\alpha, & Q_1 &= E_\infty + E_0 \tau^\alpha D^\alpha, \\ P_2 &= 1, & Q_2 &= 3K, \end{aligned} \tag{5.8}$$

where K is the bulk modulus of the brain tissue.

The time-dependent viscoelastic Young's modulus and Poisson ratio are [38]

$$E_v(t) = \frac{3Q_1Q_2}{P_2Q_1 + 2P_1Q_2} \qquad \text{and} \qquad \nu_v(t) = \frac{P_1Q_2 - P_2Q_1}{P_2Q_1 + 2P_1Q_2}. \tag{5.9}$$

We substitute $\dfrac{1+\nu}{E} = \dfrac{P_1}{Q_1}$ and $(1-2\nu) = \dfrac{3P_2Q_1}{P_2Q_1 + 2P_1Q_2}$ in (5.5) and take the Laplace Transform (using the notation $\mathcal{L}\{f\} = \bar{f}$) to obtain

$$\bar{u}(r,s) = \bar{p}_i(s) \left(\frac{a^2}{b^2 - a^2} \right) \frac{\bar{P}_1}{\bar{Q}_1} \left(\frac{3\bar{P}_2\bar{Q}_1}{\bar{P}_2\bar{Q}_1 + 2\bar{P}_1\bar{Q}_2} r + \frac{b^2}{r} \right). \tag{5.10}$$

Substituting the Laplace Transform of the differential operators and simplifying gives

$$\begin{aligned} \bar{u}(r,s) = \frac{a^2}{b^2 - a^2} \Bigg[& \left(\frac{3r}{6K + E_0} + \frac{b^2}{E_0 r} \right) \bar{p}_i(s) \\ & + \frac{b^2(E_0 - E_\infty)}{E_0^2 \tau^\alpha r} \bar{p}_i(s) \frac{1}{s^\alpha + \hat{c}} + \frac{3(E_0 - E_\infty) r}{(6K + E_0)^2 \tau^\alpha} \bar{p}_i(s) \frac{1}{s^\alpha + \hat{d}} \Bigg], \end{aligned} \tag{5.11}$$

where $\hat{c} = \dfrac{E_\infty}{E_0} \tau^{-\alpha}$, and $\hat{d} = \dfrac{6K + E_\infty}{6K + E_0} \tau^{-\alpha}$.

The generalized Mittag-Leffler function, defined by

$$E_{\alpha,\beta}(z) = \sum_{k=0}^{\infty} \frac{z^k}{\Gamma(\alpha k + \beta)},$$

satisfies the identity,

$$\int_0^\infty e^{-st} t^{\alpha k + \beta - 1} E_{\alpha,\beta}^{(k)}(\pm c t^\alpha) \mathrm{d}t = \frac{k! s^{\alpha - \beta}}{(s^\alpha \mp c)^{k+1}},$$

where $\alpha, \beta \in \mathbb{C}$, $\mathrm{Re}(\alpha) > 0$, $\mathrm{Re}(\beta) > 0$, and $k = 0, 1, 2, \ldots$ [23, 52]. Thus, the inverse Laplace Transform of $\frac{1}{s^\alpha + c}$ can be expressed in terms of the generalized Mittag-Leffler function as $\mathcal{L}^{-1}\left\{ \frac{1}{s^\alpha + c} \right\} = t^{\alpha - 1} E_{\alpha,\alpha}(-ct^\alpha)$. Taking the inverse Laplace Transform of (5.11) and using the above result we obtain an analytic

expression for the displacement,

$$u(r,t) = \frac{a^2}{b^2-a^2}\Bigg[\left(\frac{3r}{6K+E_0}+\frac{b^2}{E_0 r}\right)p_i(t) + \frac{b^2(E_0-E_\infty)}{E_0^2\tau^\alpha r}p_i(t) * \left(t^{\alpha-1}E_{\alpha,\alpha}\left(-\hat{c}t^\alpha\right)\right) + \frac{3(E_0-E_\infty)r}{(6K+E_0)^2\tau^\alpha}p_i(t) * \left(t^{\alpha-1}E_{\alpha,\alpha}\left(-\hat{d}t^\alpha\right)\right)\Bigg], \tag{5.12}$$

where $*$ denotes the convolution operation over time.

In order to compare this result to the solution presented by Sivaloganathan *et al.* [114], we define the pulsatile boundary condition to be $p_i(t) = p^* \cos\omega t$, with p^* a constant, and choose $\alpha = 1$. To simplify the result, the following property and convolution result are required: the Mittag-Leffler function satisfies $E_{1,1}(z) = E_1(z) = e^z$, and the convolution of a cosine and exponential is

$$\int_0^\infty \cos\left(\omega(t-s)\right)e^{-\delta s}\mathrm{d}s = \frac{1}{1+\frac{\delta^2}{\omega^2}}\left(\frac{1}{\omega}\sin\omega t + \frac{\delta}{\omega^2}\cos\omega t - \frac{\delta}{\omega^2}e^{-\delta t}\right). \tag{5.13}$$

After some manipulation, the fractional Zener viscoelastic model predicts the displacement to be

$$u(r,t) = \frac{a^2p^*}{b^2-a^2}\Bigg\{\left(\frac{3r}{6K+E_0}+\frac{b^2}{E_0 r}\right)\cos\omega t + \frac{b^2(E_0-E_\infty)}{E_0^2\tau r}\cdot\frac{1}{1+\frac{\hat{c}^2}{\omega^2}}\left(\frac{1}{\omega}\sin\omega t + \frac{\hat{c}}{\omega^2}\cos\omega t - \frac{\hat{c}}{\omega^2}e^{-\hat{c}t}\right) + \frac{3(E_0-E_\infty)r}{(6K+E_0)^2\tau}\cdot\frac{1}{1+\frac{\hat{d}^2}{\omega^2}}\left(\frac{1}{\omega}\sin\omega t + \frac{\hat{d}}{\omega^2}\cos\omega t - \frac{\hat{d}}{\omega^2}e^{-\hat{d}t}\right)\Bigg\}, \tag{5.14}$$

which is similar in form to the solution presented by Sivaloganathan *et al.* [114], reprinted later in this Chapter for completeness (5.23).

Finally, the planar stresses in the infant hydrocephalus case are given by

$$\sigma_{rr}(r,t) = \frac{a^2p^*}{b^2-a^2}\cos\omega t\left(1-\frac{b^2}{r^2}\right)$$

and

$$\sigma_{\theta\theta}(r,t) = \frac{a^2p^*}{b^2-a^2}\cos\omega t\left(1+\frac{b^2}{r^2}\right). \tag{5.15}$$

5.1.2 Adult Hydrocephalus

In adult hydrocephalus, the skull is rigid and so the outer boundary condition must be changed from the zero-stress condition of (5.4) to a zero-displacement condition. Thus, we wish to solve (5.3) subject to the boundary conditions

$$\sigma_{rr} = -p_i \quad \text{at} \quad r = a \qquad \text{and} \qquad u = 0 \quad \text{at} \quad r = b. \tag{5.16}$$

In this case, the linear elastic solution is

$$\begin{cases} u(r,t) = p_i(t)\frac{a^2 b(1-2\nu)(1+\nu)}{(a^2+(1-2\nu)b^2)E}\left(\frac{b}{r}-\frac{r}{b}\right) \\ \sigma_{rr}(r,t) = -p_i(t)\frac{a^2}{a^2+(1-2\nu)b^2}\left(1+\frac{b^2(1-2\nu)}{r^2}\right) \\ \sigma_{\theta\theta}(r,t) = -p_i(t)\frac{a^2}{a^2+(1-2\nu)b^2}\left(1-\frac{b^2(1-2\nu)}{r^2}\right). \end{cases} \tag{5.17}$$

As before, we assume the deviatoric response and the dilatational response of the brain can be separated according to (5.7) and (5.8). Using the time-dependent Young's modulus and Poisson ratio defined in (5.9) and the Laplace Transform, we get that

$$\begin{aligned} \frac{(1-2\nu)(1+\nu)}{\left(a^2+(1-2\nu)b^2\right)E} &= \frac{3\bar{P}_1\bar{P}_2}{\left(\bar{P}_2\bar{Q}_1+2\bar{P}_1\bar{Q}_2\right)a^2+3\bar{P}_2\bar{Q}_1 b^2} \\ &= \frac{3\left(s^\alpha+\tau^{-\alpha}\right)}{\left((6K+E_0)a^2+3E_0b^2\right)s^\alpha+\left((6K+E_\infty)a^2+3E_\infty b^2\right)\tau^{-\alpha}}. \end{aligned}$$

By the elastic-viscoelastic Correspondence Principle, the Laplace Transform of the displacement is

$$\bar{u}(r,s) = \frac{3a^2 b\bar{p}_i(s)}{\hat{g}}\left(\frac{b}{r}-\frac{r}{b}\right)\left(1+\frac{(1-\hat{h})}{\tau^\alpha}\frac{1}{s^\alpha+\hat{h}\tau^{-\alpha}}\right), \tag{5.18}$$

where $\hat{f} = (6K+E_\infty)a^2+3E_\infty b^2$, $\hat{g} = (6K+E_0)a^2+3E_0b^2$, and $\hat{h} = \frac{\hat{f}}{\hat{g}}$. Taking the inverse Laplace Transform gives the displacement in terms of the generalized Mittag-Leffler function,

$$u(r,t) = \frac{3a^2 b}{\hat{g}}\left(\frac{b}{r}-\frac{r}{b}\right)\left(p_i(t)+\frac{1-\hat{h}}{\tau^\alpha}p_i(t)*\left(t^{\alpha-1}E_{\alpha,\alpha}\left(-\hat{h}\left(\frac{t}{\tau}\right)^\alpha\right)\right)\right). \tag{5.19}$$

In the infant hydrocephalus case, the planar stresses did not depend on the Young's modulus or Poisson ratio, and thus were the same for both the elastic and the viscoelastic problems. In contrast, the adult hydrocephalus case planar stresses depend on these parameters and thus must be calculated using the elastic-viscoelastic Correspondence Principle. In a similar procedure as above, the planar stresses are

$$\begin{aligned} \sigma_{rr}(r,t) = &-a^2\left(\hat{A}+\hat{D}\frac{b^2}{r^2}\right)p_i(t) \\ &-a^2\left(\hat{A}\hat{C}+\hat{D}\hat{G}\frac{b^2}{r^2}\right)\tau^{-\alpha}p_i(t)*\left(t^{\alpha-1}E_{\alpha,\alpha}\left(-\hat{h}\left(\frac{t}{\tau}\right)^\alpha\right)\right) \end{aligned} \tag{5.20}$$

and

$$\begin{aligned} \sigma_{\theta\theta}(r,t) = &-a^2\left(\hat{A}-\hat{D}\frac{b^2}{r^2}\right)p_i(t) \\ &-a^2\left(\hat{A}\hat{C}-\hat{D}\hat{G}\frac{b^2}{r^2}\right)\tau^{-\alpha}p_i(t)*\left(t^{\alpha-1}E_{\alpha,\alpha}\left(-\hat{h}\left(\frac{t}{\tau}\right)^\alpha\right)\right), \end{aligned} \tag{5.21}$$

where

$$\hat{A} = \frac{6K + E_0}{(6K + E_0)a^2 + 3E_0 b^2}, \qquad \hat{D} = \frac{3E_0}{(6K + E_0)a^2 + 3E_0 b^2},$$
$$\hat{C} = \frac{6K + E_\infty}{6K + E_0} - \hat{h}, \text{ and} \qquad \hat{G} = \frac{E_\infty}{E_0} - \hat{h}.$$

For $\alpha = 1$ and $p_i(t) = p^* \cos \omega t$ these expressions simplify to

$$u(r,t) = \frac{3a^2 b p^*}{\hat{g}} \left(\frac{b}{r} - \frac{r}{b} \right) \Bigg[\cos \omega t + \frac{1 - \hat{h}}{\tau \left(1 + \frac{\hat{h}^2}{\tau^2 \omega^2} \right)} \left(\frac{1}{\omega} \sin \omega t + \frac{\hat{h}}{\tau \omega^2} \cos \omega t - \frac{\hat{h}}{\tau \omega^2} e^{-\hat{h} \frac{t}{\tau}} \right) \Bigg],$$

$$\sigma_{rr}(r,t) = -a^2 p^* \Bigg[\left(\hat{A} + \hat{D} \frac{b^2}{r^2} \right) \cos \omega t + \frac{\hat{A}\hat{C} + \hat{D}\hat{G} \frac{b^2}{r^2}}{\tau \left(1 + \frac{\hat{h}^2}{\tau^2 \omega^2} \right)} \left(\frac{1}{\omega} \sin \omega t + \frac{\hat{h}}{\tau \omega^2} \cos \omega t - \frac{\hat{h}}{\tau \omega^2} e^{-\hat{h} \frac{t}{\tau}} \right) \Bigg],$$

and

$$\sigma_{\theta\theta}(r,t) = -a^2 p^* \Bigg[\left(\hat{A} - \hat{D} \frac{b^2}{r^2} \right) \cos \omega t + \frac{\hat{A}\hat{C} - \hat{D}\hat{G} \frac{b^2}{r^2}}{\tau \left(1 + \frac{\hat{h}^2}{\tau^2 \omega^2} \right)} \left(\frac{1}{\omega} \sin \omega t + \frac{\hat{h}}{\tau \omega^2} \cos \omega t - \frac{\hat{h}}{\tau \omega^2} e^{-\hat{h} \frac{t}{\tau}} \right) \Bigg],$$

which are similar in form to the solutions presented by Sivaloganathan *et al.* [114], reprinted in the next Section.

5.2 Numerical Simulations

We can now compare the displacement of brain parenchyma due to ventricular pulsations in the hydrocephalic brains of infants and adults assuming the fractional Zener viscoelastic model, developed here, to the standard viscoelastic model presented by Sivaloganathan *et al.* [114]. The constitutive equation for the standard viscoelastic model, Figure 5.1b on page 52, is

$$\sigma + \frac{\eta}{k_1 + k_2} \frac{\mathrm{d}\sigma}{\mathrm{d}t} = \frac{k_1 k_2}{k_1 + k_2} \epsilon + \frac{\eta k_1}{k_1 + k_2} \frac{\mathrm{d}\epsilon}{\mathrm{d}t}. \tag{5.22}$$

Davis *et al.* [23] determined the material constants of the fractional Zener viscoelastic model by fitting to the experimentally determined brain tissue relaxation data presented by Galford and McElhaney [43]. They found that the best fit required $E_\infty = 1.612$ kPa, $E_0 = 7.715$ kPa, $\tau = 6.709$ s, and $\alpha = 0.641$ [23].

The model parameters for the standard viscoelastic model can be inferred by equating coefficients between the standard (5.22) and fractional Zener (5.2) constitutive equations. This results in the following relations:

$$k_1 = E_0, \qquad k_2 = \frac{E_\infty E_0}{E_0 - E_\infty}, \text{ and} \qquad \eta = \frac{E_0^2 \tau^\alpha}{E_0 - E_\infty}.$$

The standard viscoelastic model solutions to the equation of motion (5.3) subject to the infant (5.4) or adult (5.16) boundary conditions, derived by Sivaloganathan *et al.* [114] are presented below for completeness. Applying the infant boundary conditions (5.4), the stresses are the same as for the fractional Zener viscoelastic model (5.15) but the displacement is

$$\begin{aligned} u(r,t) = \frac{a^2 p^*}{b^2 - a^2} \Bigg[& \left(\frac{3r}{6K + k_1} + \frac{b^2}{k_1 r} \right) \cos \omega t \\ & + \frac{b^2}{\eta r} \cdot \frac{1}{1 + \frac{\tilde{c}^2}{\omega^2}} \left(\frac{1}{\omega} \sin \omega t + \frac{\tilde{c}}{\omega^2} \cos \omega t - \frac{\tilde{c}}{\omega^2} e^{-\tilde{c}t} \right) \\ & + \frac{3k_1^2 r}{\eta(6K + k_1)^2} \cdot \frac{1}{1 + \frac{\tilde{d}^2}{\omega^2}} \left(\frac{1}{\omega} \sin \omega t + \frac{\tilde{d}}{\omega^2} \cos \omega t - \frac{\tilde{d}}{\omega^2} e^{-\tilde{d}t} \right) \Bigg], \end{aligned} \tag{5.23}$$

where $\tilde{c} = \dfrac{k_2}{\eta}$ and $\tilde{d} = \dfrac{k_1 k_2 + 6K(k_1 + k_2)}{\eta(6K + k_1)}$. For the adult boundary conditions (5.16), the displacement and stresses are

$$u(r,t) = \frac{3a^2 b p^*}{\tilde{g}} \left(\frac{b}{r} - \frac{r}{b} \right) \left[\cos \omega t + \frac{\tilde{j} - \tilde{h}}{1 + \frac{\tilde{h}^2}{\omega^2}} \left(\frac{1}{\omega} \sin \omega t + \frac{\tilde{h}}{\omega^2} \cos \omega t - \frac{\tilde{h}}{\omega^2} e^{-\tilde{h}t} \right) \right],$$

$$\sigma_{rr}(r,t) = -\frac{a^2 \psi_1(r) p^*}{r^2 \tilde{g}} \left[\cos \omega t + \frac{\frac{\phi_1(r)}{\psi_1(r)} - \tilde{h}}{1 + \frac{\tilde{h}^2}{\omega^2}} \left(\frac{1}{\omega} \sin \omega t + \frac{\tilde{h}}{\omega^2} \cos \omega t - \frac{\tilde{h}}{\omega^2} e^{-\tilde{h}t} \right) \right],$$

and

$$\sigma_{\theta\theta}(r,t) = -\frac{a^2 \psi_2(r) p^*}{r^2 \tilde{g}} \left[\cos \omega t + \frac{\frac{\phi_2(r)}{\psi_2(r)} - \tilde{h}}{1 + \frac{\tilde{h}^2}{\omega^2}} \left(\frac{1}{\omega} \sin \omega t + \frac{\tilde{h}}{\omega^2} \cos \omega t - \frac{\tilde{h}}{\omega^2} e^{-\tilde{h}t} \right) \right],$$

where $\tilde{f} = \frac{1}{\eta}\big((6K(k_1 + k_2) + k_1 k_2)a^2 + 3k_1 k_2 b^2\big)$, $\tilde{g} = (6K + k_1)a^2 + 3k_1 b^2$, $\tilde{h} = \frac{\tilde{f}}{\tilde{g}}$, $\tilde{j} = \frac{k_1 + k_2}{\eta}$, $\phi_i(r) = \frac{1}{\eta}\big((6K(k_1 + k_2) + k_1 k_2)r^2 + (-1)^{i+1} 3k_1 k_2 b^2\big)$, and $\psi_i(r) = (6K + k_1)r^2 + (-1)^{i+1} 3k_1 b^2$.

We used `Maple` to perform numerical simulations. Since the arguments of all the generalized Mittag-Leffler functions used in the above solutions are negative, the series that appears in the Mittag-Leffler function definition is an alternating series. The arguments also eventually decrease in magnitude for a fixed maximum time, making it is easy to determine the number of terms required to achieve a desired accuracy (here an accuracy of 10^{-6} is used). The parameter values used in the numerical simulations are recorded in Table 5.1.

Table 5.1: Fractional Zener model parameter values.

$E_0 = 7.715$ kPa [23]	$E_\infty = 1.612$ kPa [23]	$K = 2.1$ GPa
$\alpha = 0.641$ [23]	$\tau = 6.709$ s [23]	$p^* = 667$ Pa
$a = 0.03$ m	$b = 0.1$ m	$\omega = 7$ rad/s

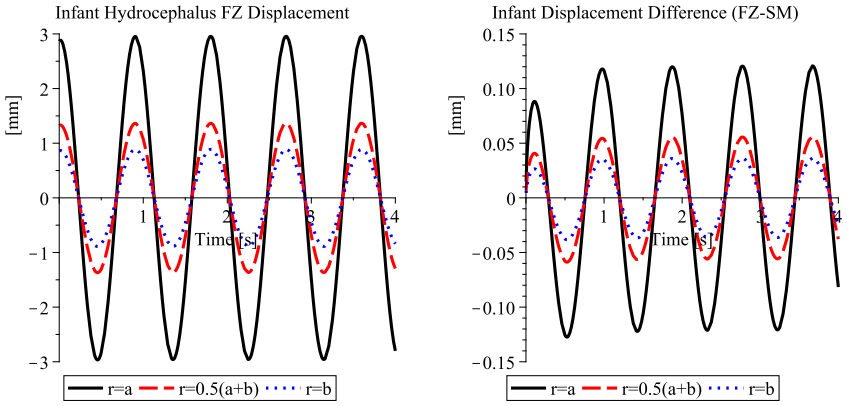

(a) **(b)**

Figure 5.3: Infant hydrocephalus displacement predicted by the fractional Zener (FZ) model (a), and the difference between the fractional Zener model and standard model (SM) displacement predictions (b).

Ventricular boundary pressure pulsations with an amplitude of 5 mm Hg (or 667 Pa) were assumed (10 mm Hg peak-to-peak amplitude). In the case of infant hydrocephalus, Figure 5.3, the predicted amplitude of the displacement waves is about 3 mm at the ventricle wall and the amplitude decreases as the wave propagates through the parenchyma. Comparing the fractional Zener viscoelastic model (FZ) to the standard viscoelastic model (SM) shows deviations of about 0.13 mm in the predicted displacements of the ventricle wall, with the fractional Zener model predicting larger displacement amplitudes than the standard model by about 4.5%. From the ventricle wall ($r = a$) to the cortical surface ($r = b$), there is about a 70% drop in wave amplitude.

For the case of adult hydrocephalus, Figure 5.4, the fractional Zener viscoelastic model predicts similar displacements when compared to the standard viscoelastic model. The maximum difference between the simulated displacements is on the order of 10^{-5} nm. The amplitude of the displacement waves for both models is about 48 nm (or 100 nm peak-to-peak) at the ventricle wall, 15 nm (or 30 nm peak-to-peak) mid parenchyma, and, as expected, zero at the cortical surface. The adult hydrocephalus displacements are much smaller than the predicted displacements in infant hydrocephalus, and are possibly small enough that the pulsations may be considered insignificant.

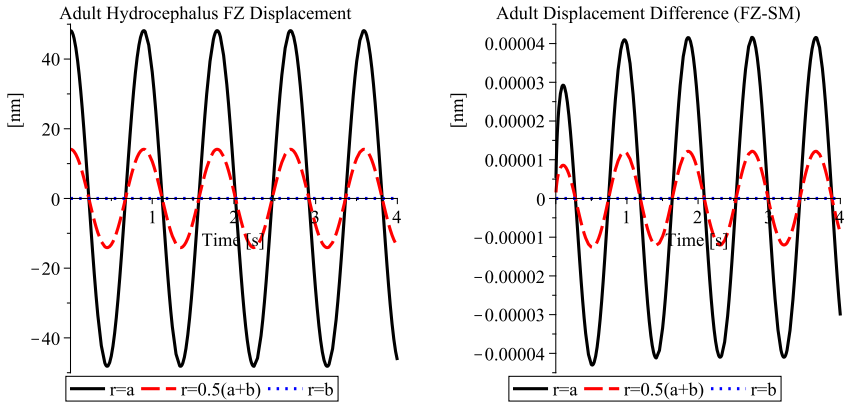

(a) **(b)**

Figure 5.4: Adult hydrocephalus displacement predicted by the fractional Zener (FZ) model (a), and the difference between the fractional Zener model and standard model (SM) displacement predictions (b).

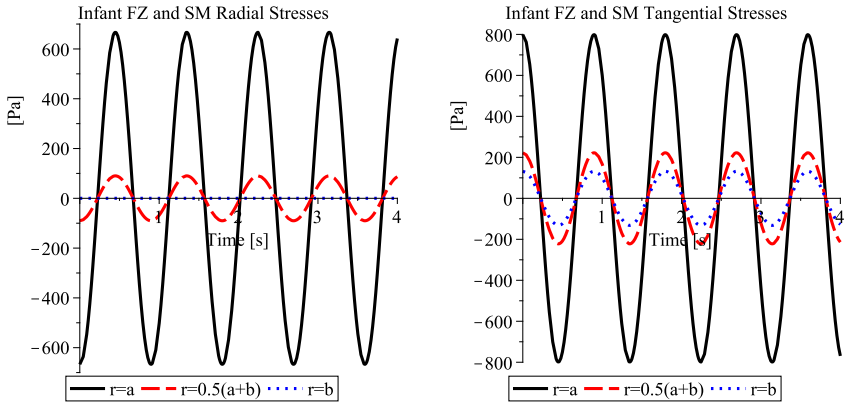

(a) **(b)**

Figure 5.5: Infant hydrocephalus fractional Zener (FZ) and standard model (SM) simulated stresses, radial (a) and tangential (b), at three points in the parenchyma. The two models predict equivalent stresses in the infant case.

The stresses for the case of infant hydrocephalus are shown in Figure 5.5. Recall that the stresses are the same for both models in this case. Maximum stress wave amplitudes (670 to 800 Pa) occur at the ventricle wall and the amplitudes decrease as the waves propagate through the parenchyma. On the cortical surface ($r = b$) the radial stress (σ_{rr}) is zero, but the tangential stress ($\sigma_{\theta\theta}$) is not. Notice also that at the ventricle wall ($r = a$), while σ_{rr} is completely

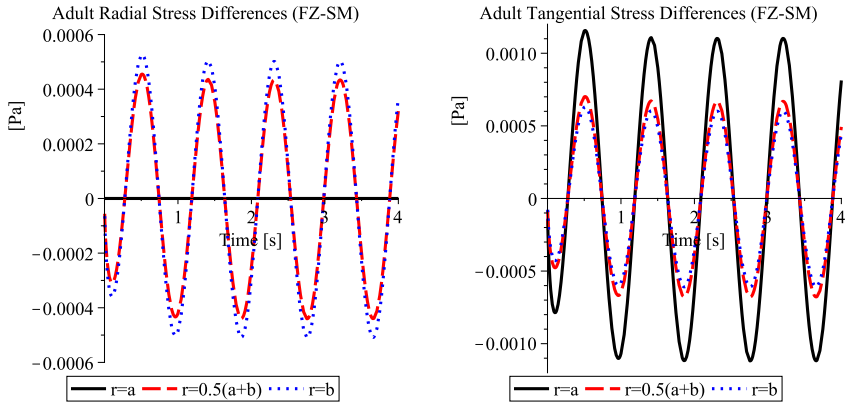

Figure 5.6: The difference between the adult hydrocephalus fractional Zener (FZ) and standard model (SM) simulated radial (a) and tangential (b) stresses at three points in the parenchyma.

out of phase with the applied pressure pulsations ($p^* \cos \omega t$), $\sigma_{\theta\theta}$ is in phase with the pulsations.

Figure 5.6 shows the stress differences between the two models for the case of adult hydrocephalus. The difference is taken as the fractional Zener model stress minus the standard model stress. Radial stress differences are shown in Figure 5.6a and tangential stress differences are shown in Figure 5.6b. The two models seem to produce very similar stress responses, with a difference on the order of 10^{-3} Pa. The amplitude of both the radial and tangential stresses is about 670 Pa throughout the parenchyma.

5.2.1 Incorporating Microstructural Changes

The experiments conducted by Galford and McElhaney [43] are from *in vitro* adult brain tissue samples, and hence the values of the mechanical parameters found by Davis *et al.* [23] do not specifically represent the hydrocephalic adult brain. The parameters for the tissue samples used, therefore, may be different from normal, living brain tissue, hydrocephalic brain tissue, and/or infant brain tissue. Thus, variations in these parameters, especially the fractional order, are possible and the effects of α on the above simulations will now be investigated for the purpose of sensitivity analysis.

It seems reasonable, for now, to assume that the mechanical parameters found by Davis *et al.* [23] adequately describe the properties of adult brain tissue, due to the obvious difficulties involved in conducting experiments *in vivo*. For infantile brain parenchyma, however, the value of α may be significantly different from the value of 0.641 used in the simulations above.

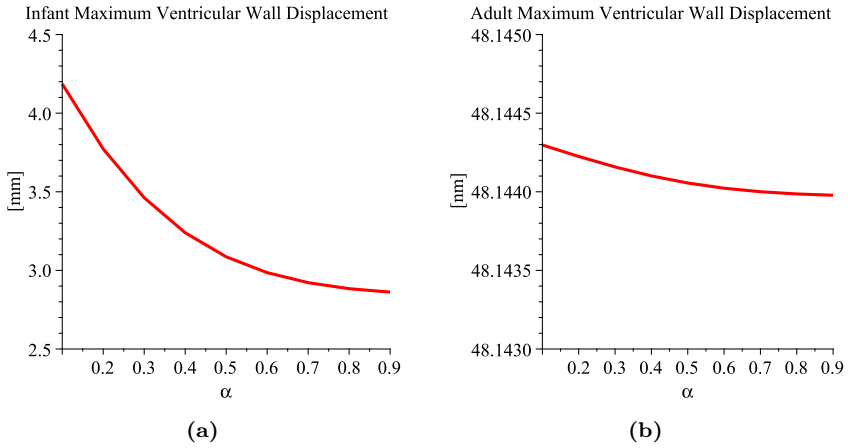

Figure 5.7: Simulated maximum displacement of the ventricle wall ($r = a$) while varying the fractional order α, for infant hydrocephalus (displacements in mm) (a) and adult hydrocephalus (displacements if nm) (b).

Figure 5.7 shows the effect the fractional order α has on the displacement of the ventricle wall. For both infant and adult hydrocephalus, larger displacements of the ventricle wall are predicted for smaller values of α. For infant hydrocephalus, the maximum amplitude for $\alpha = 0.1$ is approximately 4.2 mm which is about 1.5 times the amplitude predicted by the standard viscoelastic model (2.7 mm). Compared to this case, the change in maximum displacement amplitude of the ventricle wall in adult hydrocephalus is quite small (note the different range and units (nm) used in Figure 5.7b).

The process of infant brain growth and development occurs over the first two years of life and is a faster process than adult brain degeneration. The unfused sutures and open fontanel of an infant skull permit this rapid brain growth but they also enable variations in the mechanical properties of the brain to significantly affect tissue motion. In adults, where the sutures are fused and the skull is rigid, brain tissue motion is restricted and hence variations in the fractional order α, while still affecting tissue motion, cannot produce as obvious an effect as they can in infants. The coupling between the fractional order α and the microscopic kinematics of brain tissue will be investigated in the next Chapter.

The predictions shown in Figure 5.7a are quite encouraging. They suggest that the order of the fractional Zener model, α, may be able to capture microstructural changes in the brain parenchyma, and when combined with CSF pulsations, this may lead to ventricular enlargement and the development of hydrocephalus.

Bulk modulus measures a material's resistance to uniform compression. In the previous simulations the bulk modulus of water was used for the bulk mod-

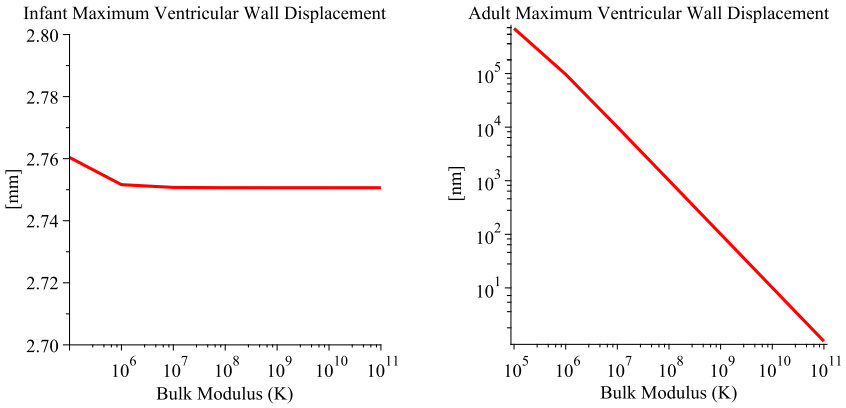

Figure 5.8: Simulated maximum displacement of the ventricle wall while varying the bulk modulus K, for infant hydrocephalus (displacements in mm) (a) and adult hydrocephalus (displacements in nm on a log scale) (b).

ulus of brain tissue since the water content of the brain is approximately 75% for normal adults, and higher when affected by age or health. In this Chapter, the dilatational behaviour of the brain was modelled as an incompressible linear elastic solid, but the value of the bulk modulus for brain tissue, especially infant or hydrocephalic brain tissue, is not clear in the literature (Young's modulus for brain tissue varies from 600 [120] to 21,000 Pa [121] and Poisson ratio varies from 0.35 to 0.4999 [121], or 0.5 if numerical instabilities were not an issue). Thus, the effect of variations in the bulk modulus on parenchyma motion is important to determine.

Figure 5.8 shows how variations in the bulk modulus (K) affect the maximum displacement of the ventricle wall. For infant hydrocephalus, there is a relatively small change in amplitude when the bulk modulus is changed due to the zero-stress boundary condition that represents the ability of the unfused skull to deform. For adult hydrocephalus, the amplitude changes by orders of magnitude (note that a log scale has been used on the vertical axis in Figure 5.8b), indicating that in a rigid skull, variations in the bulk modulus of brain tissue affect the motion significantly.

In infant hydrocephalus, the unfused skull should dampen the effects of variations in the bulk modulus which is consistent with the results in Figure 5.8a. As the adult brain ages, however, the mass of white matter slowly decreases as it is replaced by CSF. This may cause the ventricular CSF pressure to decrease which would result in a decreased bulk modulus. With a decrease in bulk modulus, an aged brain may be more susceptible to the development of hydrocephalus, even under normal pressure conditions.

5.3 Discussion

In this Chapter, the fractional Zener model of viscoelasticity was used to solve the boundary value problems related to infant and adult hydrocephalus. A pulsatile ventricular pressure was applied to the inner boundary to reproduce the effects of the cerebrospinal fluid pulsations in the cranial cavity (which occur due to the beating heart). Parameter values for the fractional Zener model were taken from Davis *et al.* [23] where the model was fitted to experimental relaxation data. The parameter values for the standard model were estimated from this data by comparing the two constitutive equations.

In infant hydrocephalus, zero stress was enforced at the cortical surface ($r = b$) to permit possible movement of the unfused skull. This results in large displacements (about 6 mm peak-to-peak at the ventricle wall ($r = a$) and almost 2 mm peak-to-peak at the cortical surface) predicted by both the fractional Zener and standard viscoelastic models, with the fractional Zener model predicting slightly larger displacements. The stress amplitude predicted by both models at the ventricle wall is about 670 Pa for radial stress, and 800 Pa for tangential stress.

In adult hydrocephalus, zero displacement was enforced at the cortical surface to reflect the fact that the adult skull is rigid and thus constrains brain tissue displacement. Both models predicted peak-to-peak displacements of about 100 nm at the ventricle wall and radial and tangential stress amplitudes of about 670 Pa throughout the parenchyma. The difference between the two models in both the predicted displacement and stresses was negligible.

According to the pulsation-damage hypothesis, the damage observed in the ependyma and periventricular tissues of hydrocephalic brains is caused by the strains induced by large amplitude CSF pulsations [101]. Tissue damage is usually assumed to begin when the *locking* section of a stress-strain curve transitions into the *hardening* section of the curve. Franceschini *et al.* [40] found this transition to occur at a stress of 2.71 kPa for white matter. Their stress-strain curve peaked at 3.43 kPa and the fracture point was 2.52 kPa. The radial and tangential tissue stresses predicted in this Chapter during extension of the parenchyma are 25% to 30% of the transition to hardening threshold found by Franceschini *et al.* [40], and thus are unlikely to cause tissue damage.

During neurosurgery the brain pulses visibly at roughly the frequency of the heart beat with clearly evident large displacements. This observation does not contradict the results of the adult hydrocephalus simulations, Figure 5.4, where extremely small displacements are predicted, since the removal of the skull changes the boundary condition on the cortical surface from zero displacement to zero stress, (i.e. analogous to the case of infant hydrocephalus). Thus, when the skull is closed, only small displacements of the parenchyma can occur, but when the skull is open, displacements large enough to be seen by the human eye ensue as a result of the removal of the restrictive rigid skull.

The pressure amplitude used was 667 Pa (see Table 5.1) or about 5 mm Hg (10 mm Hg peak-to-peak amplitude) which corresponds to pressure pulsation

amplitudes during the induction of hydrocephalus [68] or during hydrocephalus with increased intracranial pressure [35]. Normal brain or shunted hydrocephalic brain CSF pulse amplitudes are on the order of 2.5 mm Hg (or 5 mm Hg peak-to-peak amplitude) [35]. Reducing the model pressure amplitude to 333 Pa will reduce the tissue displacements by 50% indicating that during the onset of hydrocephalus when pulse amplitude is abnormally large, tissue motion is increased especially near the ventricles. This increased motion, when coupled with unhealthy brain tissue (altered mechanical properties), may facilitate the damage to the periventricular region often observed in the hydrocephalic brain.

The parameters of the linear viscoelastic fractional Zener model (see Table 5.1) were based on the *in vitro* experiments with healthy human brain tissue reported by Galford and McElhaney [43]. How these parameter values are altered by hydrocephalus due to microstructural changes in the tissue and compositional changes to the CSF is unknown. Our results show that the order of the fractional derivative, α, in the fractional Zener model can capture the effects of microstructural changes and growth processes in brain parenchyma. A relationship between aging and the bulk modulus is suggested, with results indicating that a decreased bulk modulus may make the brain more susceptible to developing hydrocephalus.

Variations in the bulk modulus clearly have an impact on ventricular distension (Figure 5.8). Thus, it is plausible that, coupled with microstructural changes in the brain tissue induced by molecular mechanisms (Johnston [86]), the mechanical forces generated by CSF pulsations may indeed contribute partially to the progression of hydrocephalus. The work of M. Johnston and coworkers has provided novel insights into interstitial pressure regulation by β_1-integrins and connective tissue elements. Their experimental work demonstrates that the dissociation of β_1-integrins with the surrounding extracellular matrix results in a significant drop in interstitial fluid pressure, thus also contributing to a significant change in the material parameters of the brain parenchyma. Hence even from the perspective of poroelasticity theory, the drop in interstitial fluid pressure results in enhanced movement of CSF from the ventricle into the brain tissue providing a mechanism for brain tissue compression.

In addition, the increased hydrostatic pressure gradient favours capillary fluid filtration (assuming that degradation of the blood brain barrier or heightened osmotic pressure gradients occur as a result of these molecular mechanisms). This then introduces the intriguing possibility that some forms of pediatric hydrocephalus may be treatable through the administration of pharmacological agents rather than through the use of shunts, with their associated problems which are far from resolved. Investigating this possibility is left to future work which would be conducted in collaboration with M. Johnston and colleagues.

From the results discussed in this Chapter, there is little evidence to suggest that the mechanical forces induced by CSF pulsations on their own play any significant role in the development of hydrocephalus. The displacements and stresses of the infant and adult hydrocephalic brains predicted by both the

fractional Zener model and the standard model are arguably negligibly small; however, the standard model is a linear model and the fractional Zener model is based on the linear Zener model, so their abilities to predict the large displacements seen in hydrocephalus are limited. Due to the promising indications of the ability of the fractional Zener viscoelastic model to capture nonlinear effects, the relationship between the fractional order derivative and the growth or aging of the brain parenchyma is investigated in Chapter 6, where the implications that brain growth or aging may have on the significance of the CSF pulsations are also investigated.

Chapter 6

The Effects of Aging on Brain Biomechanics

In this Chapter, we use experimental data for infant and adult brain tissue to determine new parameter values for the fractional Zener, the Zener, and the standard linear viscoelastic models. Using the fractional Zener model developed in the previous Chapter, we use the new parameter values to recompute the displacements and stresses of the infant and adult hydrocephalic brains due to the CSF pulsations.

The mechanical properties of brain tissue are required for mathematical models used in the study of clinical conditions such as hydrocephalus or traumatic brain injury. Due to the complex structure of brain tissue, these properties are difficult to determine experimentally and parameter values for human parenchyma are often inferred from animal experiments. Typically, these properties are assumed to be age-independent, and infant and adult cerebra are treated as mechanically equivalent; however, hydrocephalus seems to occur most commonly in infants or adults over 60 years of age [88] which seems to suggest that brain tissue age may be important in the pathogenesis of hydrocephalus.

The earliest reported experimental data related to mechanical properties of brain parenchyma (conducted by Franke in 1954 [41]), determined the shear viscosity of swine cerebrum. Since then, many researchers have actively contributed to developments in this area [37, 43, 79, 111, 129]. These experiments used either human or animal cerebra but did not distinguish the tissue samples by age. When required, the mechanical properties of infant brain tissue are usually inferred from adult data using a brain mass scaling relationship [124].

The majority of human brain development normally occurs during the *brain growth spurt* which begins four months after conception and ends around age two. The brain growth spurt is a period of extraordinary biochemical activity where new cellular and non-cellular components synthesize in the brain from components that are temporarily allowed to cross the blood brain barrier [25].

Dobbing [25] found that brain growth and development significantly increases the DNA-P content (a measure of total cell number) and the lipid content (due to myelination) of brain tissue. He also found that the water content sharply decreases during this period but stabilizes at the end of the growth spurt. After the age of two, the brain continues to grow until it reaches maturity at which point it begins a slow regression period often leading to senility [25].

Normal brain aging, from infancy to old age, has been found to include the flattening and calcification of the choroid plexus epithelium as well as the thickening of the epithelial basement membrane [98]. These changes in the choroid plexus are thought to reduce CSF production, ion transport, and fluid filtration. Czosnyka *et al.* [22] found that, in patients with NPH, the resistance to CSF flow and the ICP wave amplitude increased with age, while the CSF production rate and cranial compliance decreased with age. In addition, Bateman [7] showed that both the intracranial venous pulse amplitude and the venous mean pressure increase with age. The compositional and physiological changes observed from infancy to old age suggest that the mechanical properites of brain tissue are likely to differ for infant and adult cerebra, and indeed this was shown to be the case by Thibault and Margulies [124].

As described earlier, brain parenchyma is typically modelled as either a poroelastic material saturated by a fluid (as first proposed by Hakim [51]) or as a viscoelastic solid (as in [23, 75, 129]). Quasi-linear viscoelastic models have been proposed [29, 79] but suffer from having a large number of model parameters which must be determined from the limited experimental data. The success in capturing the complex behaviour of brain tissue with a reasonable number of model parameters makes fractional order viscoelastic models ideal for studies involving brain biomechanics. The fractional Zener viscoelastic model was shown by Davis *et al.* [23] to fit the creep and relaxation experimental data of Galford and McElhaney [43] better than other viscoelastic models. The human tissue samples used in [43], however, were not distinguished by age and the strain rates used in their experiments were intentionally large to simulate head impacts. Thus, the suitability of the model parameters fitted to this data is questionable for hydrocephalus or surgery modelling purposes where small strain rates occur [120].

Infant and adult hydrocephalus cases are distinct due to the fusing of the cranial plates that occurs around two years of age. Mathematical models of hydrocephalus handle this by prescribing different boundary conditions. The fusing of the skull and the compositional and microstructural differences between infant and adult brain parenchyma cause the two cases of hydrocephalus to differ considerably in their symptoms and treatment outcomes. Thus, to better understand the pathogenesis of hydrocephalus across the human lifespan, age-dependent mechanical properties of brain tissue should be incorporated into hydrocephalus models.

In this Chapter, we use the age-dependent shear complex modulus data presented by Thibault and Margulies [124] to determine infant and adult brain tissue parameter values for the fractional Zener, the Zener, and the standard

linear viscoelastic models. The fractional Zener model parameter values are then used in numerical simulations of the brain motions due to pulsatile ventricular pressure. The simulations use the model developed in Chapter 5, also presented in [132], and the new predictions are compared to those of the previous Chapter. We suggest a new boundary condition for the infant skull as a more realistic alternative to the stress-free boundary condition normally used. Simulations of this new boundary value problem are presented and compared to the zero-stress solution for infant brain displacement. Parameter sensitivity analyses are performed, and the steady-state elastic modulus is identified as a significant parameter in models of hydrocephalus.

6.1 Age-Dependent Data

The complex modulus of a viscoelastic material describes its behaviour under oscillatory strain. Assuming an ω-periodic strain of amplitude ϵ_0, $\epsilon(t) = \epsilon_0 \mathrm{e}^{i\omega t}$, the long-time stress response is $\sigma(t) = G^*(i\omega)\epsilon_0 \mathrm{e}^{i\omega t}$, where $G^*(i\omega)$ is the complex modulus. Splitting the complex modulus into real and imaginary parts gives

$$G^*(i\omega) = G'(\omega) + iG''(\omega),$$

where G' is the storage modulus and G'' is the loss modulus [19].

Thibault and Margulies [124] studied the effect of age on the mechanical properties of brain tissue. They performed *in vitro* oscillatory shear tests on infant and adult porcine cerebrum and determined the resulting complex moduli using frequencies from 20 to 200 Hz and 2.5% and 5% shear strains. We use the complex modulus for 2.5% shear strain since hydrocephalus develops slowly over time, via the incremental accumulation of small strains [65, 69].

Recently, the effects of age and gender on brain tissue viscoelasticity were investigated by Sack *et al.* [106] using magnetic resonance elastography (MRE). Their method measured the complex modulus of living brain tissue within the closed cranium and with an active cerebrovasculature, which is known to contribute to the stiffness of brain tissue. Using adult volunteers ranging in age from 18 to 88 years and driving frequencies from 25 to 62.5 Hz, they found both the storage and loss moduli decrease with age. Table 6.1 lists the storage and loss moduli for infant and adult porcine cerebrum [124] and adult human cerebrum [106] at similar frequencies.

As a comparison to this data, Fallenstein and Hulce [37] found the storage modulus of *in vitro* brain tissue to range from 600 to 1100 Pa and the loss modulus to range from 350 to 600 Pa using frequencies from 9 to 10 Hz. Galford and McElhaney [43] found that for *in vitro* human brain tissue, at a frequency of 34 Hz, the storage modulus is 22 200 Pa and the loss modulus is 8700 Pa. The values found by Shuck and Advani [111] range from 7600 to 33 900 Pa for the storage modulus and from 2800 to 81 400 Pa for the loss modulus using frequencies from 5 to 350 Hz. These significant differences indicate the difficult nature of measuring the mechanical properties of brain tissue and may

Table 6.1: Brain tissue complex moduli for infant and adult porcine cerebrum [124] and adult human cerebrum [106].

Frequency [Hz]	20	25	30	37.5	40	50	60	62.5
Infant[124] G' [Pa]	758		674		747	800	842	
Adult[124] G' [Pa]	1200		1053		1095	1200	1263	
Adult[106] G' [Pa]		1100		1310		1520		2010
Infant[124] G'' [Pa]	210		300		330	430	460	
Adult[124] G'' [Pa]	350		460		600	740	860	
Adult[106] G'' [Pa]		480		570		600		800

be a consequence of the different methods used and the different tissue sample treatments used in the experiments.

6.2 The Fractional Zener Model

The constitutive equation for the fractional Zener model is obtained by replacing the first order differential operator in the Zener model with a fractional differential operator of order α, denoted D^α. The schematic of the Zener model is given in Figure 6.1. Here, σ is the stress, ϵ is the strain, E_1 and E_2 are the spring constants (elastic moduli) and μ is the viscosity of the dashpot. Recall from Chapter 5, that by defining an initial elastic modulus $E_0 = E_1 + E_2$, a steady-state elastic modulus $E_\infty = E_2$, and a relaxation time $\tau = \frac{\mu}{E_1}$, the constitutive equation for the fractional Zener model can be written as [23, 132]

$$\sigma + \tau^\alpha D^\alpha \sigma = E_\infty \epsilon + E_0 \tau^\alpha D^\alpha \epsilon. \tag{6.1}$$

Therefore, the storage and loss moduli for the fractional Zener model are

$$G'(\omega) = \frac{E_\infty + (E_0 + E_\infty)\tau^\alpha \omega^\alpha \cos\left(\frac{\alpha\pi}{2}\right) + E_0 \tau^{2\alpha}\omega^{2\alpha}}{1 + 2\tau^\alpha \omega^\alpha \cos\left(\frac{\alpha\pi}{2}\right) + \tau^{2\alpha}\omega^{2\alpha}}, \tag{6.2}$$

and

$$G''(\omega) = \frac{(E_0 - E_\infty)\tau^\alpha \omega^\alpha \sin\left(\frac{\alpha\pi}{2}\right)}{1 + 2\tau^\alpha \omega^\alpha \cos\left(\frac{\alpha\pi}{2}\right) + \tau^{2\alpha}\omega^{2\alpha}}. \tag{6.3}$$

For comparison purposes, we use the Zener model and the standard viscoelastic model (see Figure 6.1). The complex modulus for model n ($n = z$ for the Zener model and $n = s$ for the standard model) is

$$G_n^*(i\omega) = \frac{E_\infty^n + E_0^n \tau_n^2 \omega^2}{1 + \tau_n^2 \omega^2} + i\frac{(E_0^n - E_\infty^n)\tau_n \omega}{1 + \tau_n^2 \omega^2}, \tag{6.4}$$

where $E_0^z = E_1^z + E_2^z$, $E_\infty^z = E_2^z$, and $\tau_z = \frac{\mu_z}{E_1^z}$ for the Zener model, and $E_0^s = k_1$, $E_\infty^s = \frac{k_1 k_2}{k_1 + k_2}$, and $\tau_s = \frac{\eta}{k_1 + k_2}$ for the standard viscoelastic model.

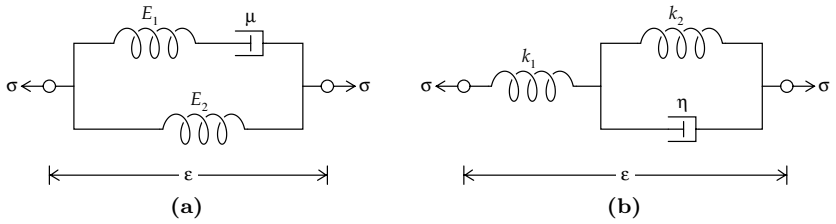

Figure 6.1: The Zener (a) and standard (b) viscoelastic model schematics.

6.3 Determining Model Parameters

For the three models discussed above, the parameter values were determined by numerically fitting to the data presented by Thibault and Margulies [124] and to the data presented by Sack *et al.* [106], using a nonlinear least squares algorithm (`lsqcurvefit` in `MATLAB`). The results of fitting the fractional Zener model to the infant and adult porcine brain tissue complex modulus data (19 data points each) are given in Figure 6.2.

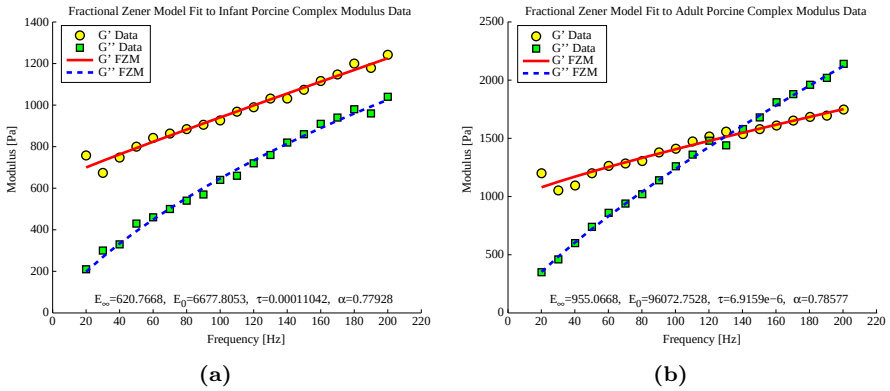

Figure 6.2: Complex moduli for the infant (a) and adult (b) porcine data [124] and the fractional Zener model (parameters determined by curve fitting).

The model parameters determined by curve fitting the complex moduli to the experimental data are listed in Table 6.2. The fractional Zener model was previously fitted to the creep and relaxation data of Galford and McElhaney [43] by Davis *et al.* [23] with the following results: curve fitting to the relaxation data gave $E_\infty = 1612$ Pa, $E_0 = 7715$ Pa, $\tau = 6.709$ s, and $\alpha = 0.641$, while curve fitting to the creep data gave $11\,943 \leq E_\infty \leq 20\,770$ Pa, $9238 \leq E_0 \leq 24\,173$ Pa, $8.056 \leq \tau \leq 22.211$ s, and $0.382 \leq \alpha \leq 0.435$.

Comparing the adult parameter values for the fractional Zener model and the two data sets (column three and four of Table 6.2), we see that the values for

Table 6.2: Model parameters fit to porcine data [124] and human data [106].

Model Parameter	Infant Porcine	Adult Porcine	Adult Human
(FZM) E_∞	621 Pa	955 Pa	829 Pa
(FZM) E_0	6678 Pa	96 073 Pa	2842 Pa
(FZM) τ	110 μs	6.92 μs	2068 μs
(FZM) α	0.779	0.786	0.8
(ZM/SM) E_∞^n	737 Pa	1156 Pa	1000 Pa
(ZM/SM) E_0^n	3244 Pa	8667 Pa	2456 Pa
(ZM/SM) τ_n	425 μs	257 μs	2620 μs

E_∞ and α are of similar orders while the values for E_0 and τ are not. Caution should be taken when considering the adult human parameters since the 3- or 4-parameter models were fitted to only 4 data points; however, since the elastic moduli found by fitting to the adult human MRE data are smaller, and the relaxation times are larger, than the adult porcine fitted parameters, the same relations may exist for the infant brain parameters. That is, the MRE method of measuring the complex modulus of living brain tissue inside the closed cranium may result in elastic moduli which are smaller, and relaxation times which are larger, than those found using *in vitro* experiments.

6.3.1 Viscosity

The dashpot viscosity in the fractional Zener model is $\mu = \tau(E_0 - E_\infty)$. Using the parameter values found above, $\mu \approx 0.66$ Pa·s for both infant and adult porcine cerebrum (see Table 6.3). This value is comparable to the viscosity of glycerin. Using the parameter values for material relaxation reported by Davis *et al.* [23], the viscosity of the dashpot is 40 945 Pa·s (comparable to tar) which seems too large for the viscosity of soft brain tissue.

Fallenstein and Hulce [37] estimated the dynamic viscosity of *in vitro* brain tissue to range from 5.6 to 9.6 Pa·s. This agrees with the viscosities found using the MRE data but is larger than the viscosities found using the porcine data. The extreme differences between the viscosities found here (Table 6.3) and the viscosities corresponding to the parameter values from Davis *et al.* (40 945 to 214 514 Pa·s) [23] are due to the relaxation time (τ): the relaxation times reported here are 4 to 6 orders of magnitude smaller than the smallest value reported in [23]. The small relaxation times found here do not match the observed relaxation behaviour of brain tissue [43]. Instead, material relaxation predicted by the model parameters found here is almost instantaneous which is not a realistic representation of the relaxation behaviour of brain tissue.

Table 6.3: Fractional Zener, Zener, and standard viscoelastic model schematic parameter values based on the data fitting from Table 6.2.

Model Parameter	Infant Porcine	Adult Porcine	Adult Human
(FZM) E_1	6057 Pa	95118 Pa	2013 Pa
(FZM) E_2	621 Pa	955 Pa	829 Pa
(FZM) μ	0.67 Pa·s	0.66 Pa·s	4.16 Pa·s
(FZM) α	0.779	0.786	0.8
(ZM) E_1^z	2507 Pa	7511 Pa	1456 Pa
(ZM) E_2^z	737 Pa	1156 Pa	1000 Pa
(ZM) μ_z	1.07 Pa·s	1.93 Pa·s	3.81 Pa·s
(SM) k_1	3244 Pa	8667 Pa	2456 Pa
(SM) k_2	954 Pa	1334 Pa	1688 Pa
(SM) η	1.78 Pa·s	2.57 Pa·s	10.9 Pa·s

6.3.2 Shear Modulus

The shear modulus, G, of a fractional Zener viscoelastic material can be found by assuming the material is incompressible so that the Poisson ratio $\nu = 0.5$. Then, in steady state, when the elastic modulus $E \approx E_\infty$, the shear modulus is

$$G = \frac{E}{2(1+\nu)} \approx \frac{E_\infty}{3}.$$

Using the fractional Zener model parameters of Table 6.2, the shear modulus for infant porcine brain is 207 Pa; for adult porcine brain it is 318 Pa, and for adult human brain from MRE it is 276 Pa. The shear modulus found using the values from Davis *et al.* [23] range from 537 to 6923 Pa, which are larger than the values determined here. Dobbing [25] showed that the water content in brain tissue decreases as a function of age to about 85% of the value at birth. Assuming adult brain tissue is about 80% water, infant brain tissue should be about 94% water. Thus we should expect the value of the shear modulus to increase slightly with age from infancy, which agrees with the results above.

6.4 Tissue Displacement under Hydrocephalic Conditions and Pulsatile CSF

Assuming the deviatoric behaviour of brain tissue can be modelled by the fractional Zener model and the dilatational behaviour can be modelled by the linear elastic model, the displacement of the parenchyma can be found analytically using the elastic-viscoelastic correspondence principle. Recall that the two bound-

ary value problems describing the infant and adult cases of hydrocephalus are

$$\text{Infant} \begin{cases} \frac{\partial}{\partial r}\sigma_{rr} + \frac{1}{r}(\sigma_{rr} - \sigma_{\theta\theta}) = 0 \\ \sigma_{rr} = -p_i(t) \quad \text{at } r = a \\ \sigma_{rr} = 0 \quad \text{at } r = b \end{cases} \tag{6.5}$$

and

$$\text{Adult} \begin{cases} \frac{\partial}{\partial r}\sigma_{rr} + \frac{1}{r}(\sigma_{rr} - \sigma_{\theta\theta}) = 0 \\ \sigma_{rr} = -p_i(t) \quad \text{at } r = a \\ u = 0 \quad \text{at } r = b. \end{cases} \tag{6.6}$$

Again, we simplify the brain geometry to a thick walled cylinder (see Figure 5.2) and assume a pulsatile internal pressure of the form $p_i(t) = p^* \cos(\omega t)$. Details on the model derivation were given in Chapter 5.

The infant and adult displacement solutions to boundary value problems (6.5) and (6.6), u_I and u_A respectively, are reprinted here for completeness from Chapter 5, Equation 5.12 and Equation 5.19:

$$\begin{aligned} u_I(r,t) =& \frac{a^2}{b^2 - a^2}\left[\left(\frac{3r}{6K + E_0} + \frac{b^2}{E_0 r}\right) p_i(t)\right. \\ &+ \frac{b^2(E_0 - E_\infty)}{E_0^2 \tau^\alpha r} p_i(t) * \left(t^{\alpha-1} E_{\alpha,\alpha}\Big(-\frac{E_\infty}{E_0}\Big(\frac{t}{\tau}\Big)^\alpha\Big)\right) \\ &\left.+ \frac{3r(E_0 - E_\infty)}{(6K + E_0)^2 \tau^\alpha} p_i(t) * \left(t^{\alpha-1} E_{\alpha,\alpha}\Big(-\frac{6K + E_\infty}{6K + E_0}\Big(\frac{t}{\tau}\Big)^\alpha\Big)\right)\right] \end{aligned} \tag{6.7}$$

and

$$\begin{aligned} u_A(r,t) =& \left(\frac{b}{r} - \frac{r}{b}\right)\left[\frac{3a^2 b}{(6K + E_0)a^2 + 3E_0 b^2} p_i(t)\right. \\ &\left.+ \frac{3a^2 b(a^2 + 3b^2)(E_0 - E_\infty)}{\big((6K + E_0)a^2 + 3E_0 b^2\big)^2 \tau^\alpha} p_i(t) * \left(t^{\alpha-1} E_{\alpha,\alpha}\Big(-\hat{h}\Big(\frac{t}{\tau}\Big)^\alpha\Big)\right)\right], \end{aligned} \tag{6.8}$$

where $E_{\alpha,\alpha}(z)$ is the generalized Mittag-Leffler function,

$$\hat{h} = \frac{(6K + E_\infty)a^2 + 3E_\infty b^2}{(6K + E_0)a^2 + 3E_0 b^2},$$

and $*$ denotes the convolution operation over time. The displacements predicted in Chapter 5 used the fractional Zener model parameter values found by Davis *et al.* [23] ($E_\infty = 1,612$ Pa, $E_0 = 7,715$ Pa, $\tau = 6.709$ s, and $\alpha = 0.641$) as well as the inner radius $a = 30$ mm, the outer radius $b = 100$ mm, the inner pressure amplitude $p^* = 667$ Pa, the bulk modulus $K = 2.1$ GPa, and the angular frequency $\omega = 7$ rad/s. The maximum displacement amplitude of the ventricle wall predicted by the model with these parameter values was 3 mm in the infant case and 48 nm in the adult case.

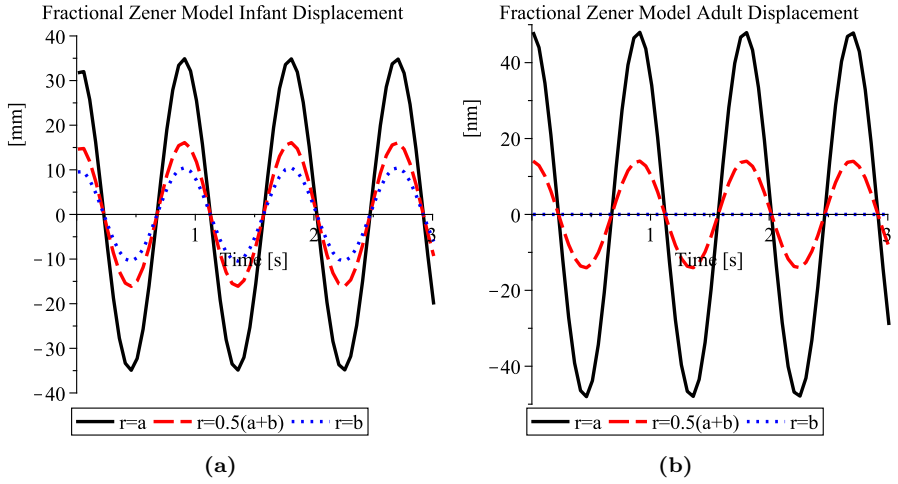

Figure 6.3: Infant (a) and adult (b) parenchyma displacements predicted by the fractional Zener model using the parameter values from Table 6.2.

Using the infant and adult porcine parameter values for the fractional Zener model (Table 6.2), the displacements of the parenchyma predicted by (6.7) and (6.8) are shown in Figure 6.3. The infant porcine parameter values predict unphysical displacements in our infant hydrocephalus model: the maximum displacement of the ventricle wall is 35 mm which is greater than the 30 mm inner radius of the model geometry. The adult case predicts a maximum displacement of 48 nm, the same as was predicted in Chapter 5.

The unphysical result obtained in the infant case is due to either an unphysical mathematical model or poor experimental data. The model gives physical and reasonable predictions in the adult case but not in the infant case where smaller elastic moduli are used. It is possible that the zero-stress boundary condition assigned in the infant case (6.5) is too weak. This condition was previously used [64, 114, 121, 132] to avoid the free boundary value problem. Assuming that the infant brain is enclosed in a thin elastic membrane representing the unfused skull, and that the large deformations observed in hydrocephalus occur over time scales much larger than those considered here, this boundary condition appears to be a reasonable approximation.

6.4.1 A Mixed Boundary Condition

An alternate boundary conditon for the infant hydrocephalus case can be constructed from the adult case [8]. The solution to the adult boundary value problem (6.6) gives an expression for the radial stress at the outer boundary ($r = b$): denote this stress by $\sigma_{rr}^{A}(b,t)$ where A indicates the (A)dult solution. Assuming the infant skull provides a fraction, δ, of the restrictive force provided by the adult skull, we can assign a new mixed boundary condition for the infant

hydrocephalus case,

$$\sigma_{rr} = \delta\sigma_{rr}^{A}(b,t) \quad \text{at } r = b. \tag{6.9}$$

From Chapter 5, Equation 5.20, the radial stress at $r = b$ in the adult hydrocephalus case is

$$\begin{aligned}\sigma_{rr}^{A}(b,t) = &\frac{-(6K+4E_0)a^2}{(E_0+6K)a^2+3E_0b^2}\, p_i(t) \\ &- \frac{6K(E_\infty - E_0)\tau^{-\alpha}a^4}{\big((6K+E_0)a^2+3E_0b^2\big)^2}\, p_i(t) * \left(t^{\alpha-1}E_{\alpha,\alpha}\Big(-\hat{h}\Big(\frac{t}{\tau}\Big)^{\alpha}\Big)\right).\end{aligned} \tag{6.10}$$

Since the partial differential equation in (6.5) is linear, boundary condition (6.9) corresponds to the linear combination of the two original boundary value problems, (6.5) and (6.6). That is, the brain tissue displacement solution of the mixed boundary value problem, u_m, is

$$u_m(r,t) = (1-\delta)u_I(r,t) + \delta u_A(r,t), \tag{6.11}$$

where $0 \le \delta \le 1$, u_I is the infant displacement solution (6.7), and u_A is the adult displacement solution (6.8). Algorithms for the numerical computation of the generalized Mittag-Leffler function are described in [44, 45] and some sample `Maple` code is provided in Appendix B.

Margulies and Thibault [70] measured the mechanical properties of infant skull and suture and conducted a finite element simulation to compare the protective properties of infant and adult skulls. They found that when a 1000 N load was applied to the skull, the infant skull deformed a maximum of 4 mm while the adult skull deformed a maximum of 2 mm. Under a 5000 N load, the infant skull deformed a maximum of 10 mm while the adult skull deformed a maximum of 4 mm. We thus infer that the infant skull provides approximately 40 to 50% of the resistive force that the adult skull provides and so we assume δ satisfies $0.4 \le \delta \le 0.5$. Note, however, that these forces are significantly larger than those we are considering in this analysis.

Since the adult displacement, u_A, is several orders of magnitude smaller than the infant displacement, u_I, the brain tissue displacement with this mixed boundary condition is approximately $(1-\delta)u_I$. Figure 6.4a shows the displacements predicted throughout the brain tissue using the parameter values listed in Table 6.2 and $\delta = 0.5$. Figure 6.4b shows the displacement of the ventricle wall at $t = 0.9$ s (the approximate location of a maximum) as a function of the mixing parameter δ.

The maximum displacement of the ventricle wall using the mixed boundary condition is 17.5 mm for $\delta = 0.5$ and 21 mm for $\delta = 0.4$. Assuming the other parameters are constant, a more clinically common ventricular wall displacement, about 5 mm [62], requires a value of $\delta \approx 0.86$. This implies that the infant skull provides about 86% of the resistive force provided by the adult skull, which may not be inconsistent with our previous assumed range since the magnitude of the force considered here is much less than the magnitudes considered by Margulies and Thibault [70].

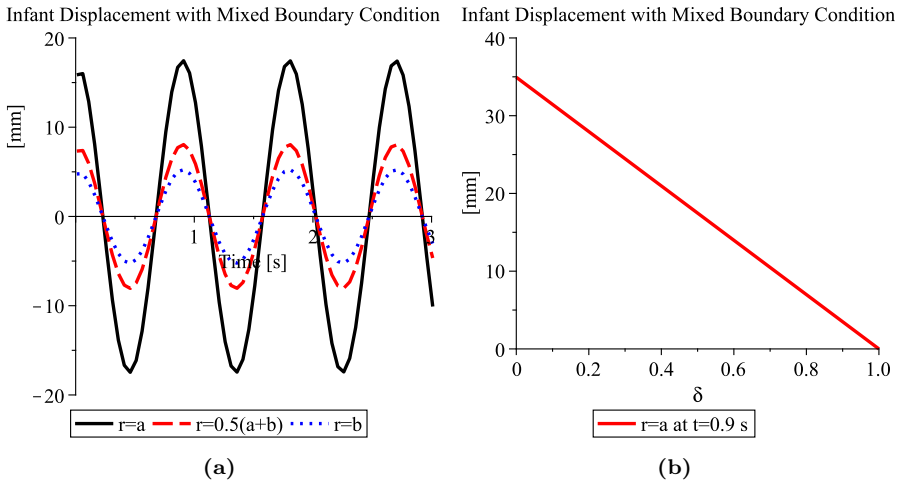

Figure 6.4: Displacements predicted by the mixed boundary value problem with the fractional Zener model using the parameter values from Table 6.2.

6.4.2 Parameter Sensitivity Analyses

The fractional Zener model parameter values found in this Chapter (see Table 6.2) were fitted to the experimental data in the least squares sense via the storage and loss moduli, (6.2) and (6.3) respectively, which are nonlinear functions of the four model parameters. To investigate the effect the parameter values have on the predictions of the infant hydrocephalus model, boundary value problem (6.5) with solution (6.7), sensitivity analyses were performed for the elastic moduli and relaxation time (E_∞, E_0, and τ). The maximum displacement of the ventricle wall was determined while one parameter was varied over a suitable range and the other parameters were held constant at the values listed in Table 6.2. The resulting plots are shown in Figure 6.5. Assuming again that a physical and reasonable amount of displacement at the ventricle wall is about 5 mm, Figure 6.5 shows that this would require either $\tau > 0.1$ s, $E_\infty > 5000$ Pa, or $E_0 > 10^6$ Pa, if the non-varied parameters have the values listed in Table 6.2.

The fractional order α in the fractional Zener model was hypothesized in Chapter 5 to capture microstructural changes in the viscoelastic material. Even though infant and adult brain tissues are known to differ in composition, microstructure [25], and mechanical properties [124], the results of fitting our model to the age-dependent data of Thibault and Margulies [124] indicate a value of $\alpha \approx 0.8$ for both ages of brain tissue.

The role of α in the fractional Zener model is to interpolate between the linear elastic model ($\alpha = 0$) and the Zener model ($\alpha = 1$) in a manner which incorporates the material history. When the relaxation time (or viscosity) is

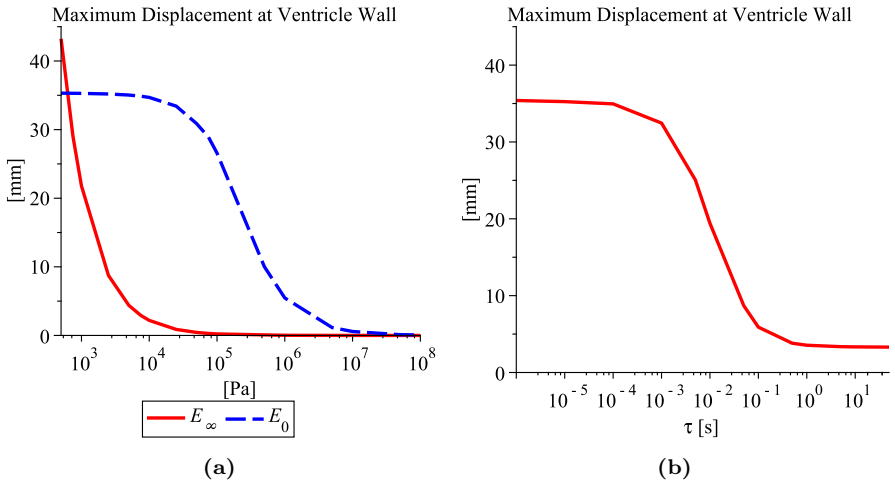

Figure 6.5: Sensitivity of maximum infant ventricle wall displacement to variations in the elastic moduli (E_∞ and E_0) (a) and the relaxation time (τ) (b) for the fractional Zener model.

large enough such that $\tau > 1$, the linear elastic model predicts larger ventricular wall displacements than the Zener model, and as α ranges from 0 to 1, this maximum displacement decreases exponentially, as discussed in Chapter 5. When the relaxation time (or viscosity) is small enough such that $\tau < 1$, as is the case here, the linear elastic model predicts smaller ventricular wall displacements than the Zener model, and as α ranges from 0 to 1, this maximum displacement increases logarithmically. This behaviour is due to the factors of τ^α in the constitutive equation (6.1). Using the infant brain tissue parameter values from Table 6.2, the maximum displacement of the ventricle wall is 6 mm when $\alpha = 0$ and 35.4 mm when $\alpha = 1$ (an unphysical displacement).

The same pressure pulse amplitude p^* and angular frequency ω have been used in all the above computations. As can be seen from the analytic forms, (6.7) and (6.8), the amplitude of the CSF pulsations is directly proportional to the resulting tissue displacements. Thus, a decrease in the pressure amplitude by half results in a decrease in the predicted displacement amplitude by half. Recall, that p^* was chosen based on clinical observations of 10 mm Hg peak-to-peak pressure pulsations in hydrocephalus patients [35]. Angular frequency variations within a physically reasonable range (5 to 14 rad/s) do not significantly affect the predicted displacements.

6.5 Discussion

The parameter values for the fractional Zener, the Zener, and the standard viscoelastic models were determined for both infant and adult cerebra. The fractional Zener model was then used to predict the response of infant and adult brains under conditions simulating the onset of hydrocephalus. The adult model predicted displacements in agreement with previously reported results [132], but the infant model predicted unphysical ventricular wall displacements.

A new boundary condition was proposed to create a new displacement boundary value problem better suited to the infant hydrocephalic brain. The new condition assumes the infant skull provides a fraction of the resistive force that the adult skull provides. The fraction, δ, was determined from infant skull and suture experiments [70] and the resulting ventricular wall displacements were physical but large. Assuming our infant parameter values were correct, a fraction of $\delta = 0.86$ was required to obtain physically and clinically reasonable [62] displacements at the ventricle wall. Although the skull rigidity, δ, was shown to control linearly the amount of tissue displacement in the infant brain, Figure 6.4b, this parameter was not considered as a possible influence in hydrocephalus development because it was assumed that the infant skull only becomes more rigid with age and that the adult skull is completely rigid ($\delta = 1$).

The fractional Zener model is based on a linear constitutive equation and is valid when a linear geometrical response is assumed (infinitesimal strains). Because of this assumption, the model is not accurate for large deformations and this may be partially responsible for the large unphysical displacements predicted by the infant model with the new parameter values of Table 6.2. The linear assumption still provides reasonable approximations for small finite deformations (less than 10 mm) and therefore the model is able to provide insights into the response of brain tissue to periodic ventricular wall loading due to CSF pulsations. This issue of geometric nonlinearity in large deformations is resolved in Chapter 7 via an incremental small strain numerical method.

Parameter sensitivity analyses demonstrated the effect of the fractional Zener model parameter values on the maximum ventricular wall displacement in the infant hydrocephalic brain. The steady-state elastic modulus, E_∞, affected the maximum displacement most when its value ranged from 500 to 10 000 Pa. The range of interest for the initial elastic modulus, E_0, was found to be 10^5 to 10^6 Pa, and the range of interest for the relaxation time, τ, was found to be 10^{-2} to 1 s. The order of the fractional derivative, α, which incorporates microstructural changes into the macroscopic description of the tissue by introducing a history dependence in the stress-strain relation, was determined to be approximately 0.8 for both infant and adult cerebra. For the viscosities found above, 0.67 Pa·s for infant cerebrum, a smaller value of α would predict smaller displacements of the parenchyma.

Our numerical simulations represented the conditions present during the onset of hydrocephalus where increased pulse amplitudes are observed [35, 94]. The fractional Zener material and infant brain tissue parameter values in our model

of infant hydrocephalus produced unphysical displacements of the ventricle wall. These unphysical displacements demonstrate the importance of parameter values in mathematical models of biological systems. Accurate and complete experimental data are required to determine parameter values for such models. Since the parameter values found here predicted unphysical displacements in the infant hydrocephalic brain, we can identify possible parameters and their corresponding mechanical behaviours that, when altered, may lead to the development of hydrocephalus. The infant parameter values found in this Chapter describe a brain that is susceptible to large deformations.

From Equation 5.15, the stresses of the infant brain are not affected by the new parameter values. The adult stresses are also relatively unaffected. The stresses in the mixed boundary condition brain are the linear combination of the infant and adult stresses: for example, $\sigma^m_{rr} = (1-\delta)\sigma^I_{rr} + \delta\sigma^A_{rr}$, where σ^I is the infant stress and σ^A is the adult stress. At the ventricle wall, the radial stress is thus equal to -670 Pa when $\delta = 0$, 0 Pa when $\delta = 0.5$, and 670 Pa when $\delta = 1$. The tangential stress is 800 Pa when $\delta = 0$, 735 Pa when $\delta = 0.5$, and 670 Pa when $\delta = 1$. These stresses are similar in magnitude to those discussed in Chapter 5 and thus we must conclude that, again, they are not sufficient to cause the tissue damage observed in hydrocephalus. The maximum shear stress measure $\tau^m(r) = \frac{1}{2}\left(\sigma^m_{\theta\theta}(r) - \sigma^m_{rr}(r)\right)$ [63, 64] decreases with r. Thus, the tissue most susceptible to damage is the periventricular region; however, the magnitudes of the stresses are still at most 30% of the transition to hardening threshold [40]. The resulting strains and stresses in the periventricular tissue, due to increased CSF pressure pulse amplitudes, may contribute to the tissue damage and ventricular expansion observed in hydrocephalus, but they cannot be the primary cause.

The infant cerebrum steady-state elastic modulus, E_∞, was determined to be about 600 Pa, which is approximately equal to the Young's modulus found by Taylor and Miller for studies of hydrocephalus (584 Pa) [120], and close to the value found by Cheng and Bilston (350 Pa) [17] for infants or young children. The steady-state elastic modulus for adult cerebrum was determined to be about 1000 Pa, almost double that found by Taylor and Miller. Both of these values lie within the range of interest identified above for the steady-state elastic modulus, meaning that slight variations in these values will have a significant effect on the predicted parenchymal displacements. Therefore, we identify the steady-state elastic modulus as a parameter of interest in the development of hydrocephalus.

Sack *et al.* [106] found both the storage and loss moduli decrease with age in adults over the age of 18 years. Thus, it is possible that the steady-state elastic modulus increases from the infant value of about 600 Pa to a maximum value of about 1000 Pa at early adulthood and then decreases with age. If this hypothesis is correct, then the increased occurrence of hydrocephalus in infants and the elderly can be partially explained by a reduced steady-state elastic modulus, which renders the tissue more susceptible to large deformations and to the development of hydrocephalus. This effect would be enhanced when

coupled with a reduced bulk modulus which, as suggested in Chapter 5, might occur in the elderly.

The microstructural mechanism for hydrocephalus proposed by M. Johnston and colleagues [86] was hypothesized to affect the macroscopic description of brain tissue by reducing the Young's modulus and increasing fluid absorption by the tissue [9]. These two factors have previously been shown to cause hydrocephalus in mathematical models [93]. The age-dependent analysis presented here suggests that infant and elderly populations may be more susceptible to hydrocephalus since the first of these two factors, a reduced steady-state elastic modulus, is realized by the immaturity, and may be realized by the degeneration [98], of the brain tissue. Therefore, the biological changes that occur during the growth and development of the infant brain, and the brain degeneration seen in older people, alter the mechanical behaviour of the parenchyma and thus, age-dependent mechanical properties need to be considered in future mathematical models of brain biomechanics for problems where age-related sensitivities may exist.

Chapter 7

A Quasilinear Fractional Hyper-Viscoelastic Model of Infant Hydrocephalus

In this Chapter, we focus on the case of infant communicating hydrocephalus and show that long-term pressure gradients on the order of 1 mm Hg are sufficient to cause ventricular expansion, especially when the mechanical properties of the brain are degraded. Recall that up to the age of two years, the infant brain undergoes rapid growth and development during the brain growth spurt, and significant changes in the mechanical properties of the brain tissue occur as a result [124]. In Chapter 6 we showed that the shear modulus, derived from the steady-state elastic modulus of infant cerebrum, is reduced when compared to the corresponding modulus of the adult cerebrum.

In previous Chapters, the hypothesis that CSF pulsations were a crucial mechanism in the pathogenesis of hydrocephalus was analyzed and it was concluded that the pulsations cannot be a primary cause of hydrocephalus. Recall that in mathematical models of non-communicating hydrocephalus, a large mean pressure gradient (non-pulsatile component) is assumed to exist between the cerebral ventricles and the subarachnoid space. This transmantle pressure gradient provides the mechanical force required to compress the brain tissue, as manifested in hydrocephalic brains. In infants, where the cranial sutures are unfused, such outward deformation of the brain parenchyma can cause the skull to expand if the condition is left untreated. In adults, where the cranial sutures are fused and the skull is rigid, the signs and symptoms of brain compression are not so outwardly evident.

The presence of such a large mean pressure gradient, however, has been questioned by Linninger *et al.* [68, 95]. They inserted pressure sensors into the ventricle, the parenchyma, and the subarachnoid space, and continuously recorded measurements in dogs with kaolin-induced hydrocephalus. Their mea-

surements show no significant pressure differences between the ventricles and the parenchyma or the ventricles and the subarachnoid space; however, the sensitivity of their sensors was approximately 1 mm Hg, hence pressure differences below this threshold would not have been observed. Levine [65] suggested that these *mini gradients* may be responsible for changes in the Starling forces, triggering fluid absorption by the tissue, and initiating and sustaining ventricular enlargement. Furthermore, Penn and Linninger [95] showed that in their model of adult hydrocephalus, mean pressure gradients on the order of 1 mm Hg were sufficient to enlarge the ventricles. Dutta-Roy, Wittek, and Miller [31], however, showed that a 1 mm Hg pressure gradient was not sufficient to enlarge the ventricles to their hydrocephalus threshold of 58 cm^3 (from 14 cm^3). Instead, they claimed a minimum pressure difference of 1.76 mm Hg was required.

The model developed in this Chapter should be able to predict large deformations of the brain, deformations involving strains greater than 5%; therefore, a neo-Hookean hyper-viscoelastic model is required [17]. Hyperelasticity describes models for which the constitutive equation is specified in terms of a strain energy density function that is dependent on the deformation gradient. The specific form of the strain energy density is phenomenologically determined. For brain tissue, a viscous component needs to be coupled with the hyperelastic component in the constitutive equation due to the tissue's highly dissipative characteristics [90].

Miller and Chinzei [79] proposed a nonlinear viscoelastic constitutive equation for brain tissue using a generalization of the Mooney-Rivlin strain energy function where the coefficients were expressed as a sum of exponentials. Libertiaux and Pascon [66] then developed a fractional derivative hyper-viscoelastic model based on this strain energy function. They compared their model to simple compression tests and found that the model fit the experimental data almost perfectly. Unfortunately, their model was not amenable to analytic methods and the physical interpretation of the model components was lost. The assumption that the energy of a compressive deformation and the energy of a tensile deformation are equal was shown to be incorrect by Miller and Chinzei [80]. To account for this, they proposed a fractional powered hyper-viscoelastic constitutive equation. Dutta-Roy, Wittek, and Miller [31] then applied a simplified version of this hyper-viscoelastic constitutive equation (strain rate dependence was dropped) to the problem of normal pressure hydrocephalus. Using a relaxed shear modulus, 156 Pa, and both a single phase and a biphasic hyperelastic material, they computed the tissue displacements using `ABAQUS` on a computational brain mesh. They showed that a pressure gradient of at least 1.764 mm Hg (235 Pa) was required to cause hydrocephalus assuming a minimal ventricular volume increase from 14 to 58 cm^3.

In this Chapter, a fractional hyper-viscoelastic model is developed due to the recent success of fractional derivatives in capturing the complex behaviour of brain tissue with a reasonably modest number of model parameters [23, 66]. The brain tissue is represented by a Kelvin-Voigt viscoelastic solid, where a hyperelastic spring is coupled in parallel to a fractional viscoelastic dashpot. A

strain energy density function of the Mooney-Rivlin form, originally developed for rubber, is assumed. The nonlinear elastic component allows for more accurate predictions of finite deformations compared to linear elastic models and the fractional derivative viscous component incorporates the material deformation history into the stress-strain relation. The model proposed in this Chapter is a quasilinear model because even though the model allows for nonlinear elasticity, the fractional viscous component is independent of the elastic component and is based on a linear viscous model. Some authors refer to this type of model as nonlinear [30], but we follow the lead of Fung [42] and refer to it as quasilinear.

The Chapter proceeds as follows: first, we develop the quasilinear viscoelastic fractional derivative model and analytic solutions under the assumption of small strains. Then, we present numerical simulations of these analytic solutions and use an iterative numerical technique exploiting the incremental law of soft tissues [42, pg. 238–9] to approximate the finite deformations observed in hydrocephalus. Finally, we solve the quasilinear model with first order derivatives numerically. This mathematical analysis allows the estimation of the ventricular expansion caused by a pressure gradient of 1 mm Hg in the infant hydrocephalic brain, and demonstrates that such pressure gradients are sufficient to cause infant hydrocephalus.

7.1 Mathematical Analysis

In this section we derive the mathematical model for the hyper-viscoelastic fractional derivative Kelvin-Voigt material and present analytic solutions to the resulting equation of motion for the case of small strains. The full quasilinear equation of motion is presented at the end of the section.

7.1.1 Model Derivation

Again, we use a simplified geometry of the hydrocephalic brain that is amenable to analytic solutions. In fully developed hydrocephalus, when the cerebral ventricles are expanded, the brain is more akin to a cylindrical shape than a spherical shape and so we set up our model as follows: consider a thick walled cylinder with inner radius R_1 and outer radius R_2 made of an incompressible fractional Kelvin-Voigt material, see Figure 7.1a.

At $t = 0$, the cylinder is in an undeformed state with a Lagrangian cylindrical co-ordinate system, (R, Θ, Z), and the unit direction vectors, $(\hat{\mathrm{e}}_R, \hat{\mathrm{e}}_\Theta, \hat{\mathrm{e}}_Z)$. The internal surface is subjected to a pressure, $p_0(t)$, and the external surface is traction free, representing the unfused infant skull. There are no body forces. For $t > 0$, the cylinder is in a deformed state due to the applied boundary conditions and the Eulerian cylindrical co-ordinate system (r, θ, z) deforms with the material. The unit direction vectors of this space are $(\hat{\mathrm{e}}_r, \hat{\mathrm{e}}_\theta, \hat{\mathrm{e}}_z)$. We assume that the ends of the cylinder are tethered so that under the action of the internal

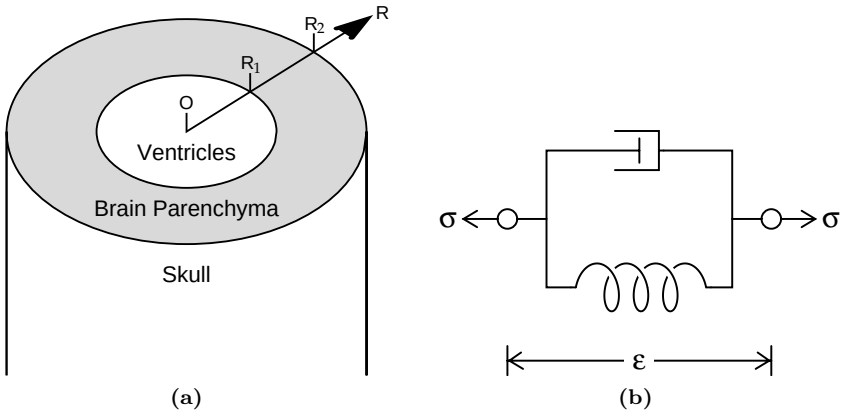

Figure 7.1: The thick walled cylinder model geometry (a) and the Kelvin-Voigt viscoelastic material schematic (b).

pressure, $p_0(t)$, radially symmetric planar deformations occur:

$$r = f(t, R), \qquad \theta = \Theta, \text{ and } \qquad z = Z, \tag{7.1}$$

where $f(t, R)$ is the deformation function to be determined. The radial vector of the deformed cylinder is thus $\vec{r}(t, R) = f(t, R)\hat{e}_r + z\hat{e}_z$.

Deformation Gradients and Tensors

Deformation gradients characterize the deformation in a small neighbourhood of any point. More details on the derivation of the following deformation gradients and deformation tensor can be found in Appendix C. The bi-tensor $\mathbf{F}(t, R)$ is the gradient of the deformation map $\vec{r}(t, R)$ with respect to the Lagrangian (undeformed) coordinates. Using the radius vector above, the deformation gradient is

$$\mathbf{F}(t, R) = h(t, R)\hat{e}_r\hat{e}_R + \frac{f(t, R)}{R}\hat{e}_\theta\hat{e}_\Theta + \hat{e}_z\hat{e}_Z, \tag{7.2}$$

where $h(t, R) = \frac{\partial f}{\partial R}(t, R)$. The relative deformation gradient tensor, which characterizes the entire history of the deformation on the interval $[0, t]$, is

$$\begin{aligned} \mathbf{F}_{\boldsymbol{\tau}}(t, R) &= \mathbf{F}(t, R) \cdot \big(\mathbf{F}(\tau, R)\big)^{-1} \\ &= \frac{h(t, R)}{h(\tau, R)}\hat{e}_r\hat{e}_r + \frac{f(t, R)}{f(\tau, R)}\hat{e}_\theta\hat{e}_\theta + \hat{e}_z\hat{e}_z. \end{aligned} \tag{7.3}$$

The left Cauchy-Green deformation tensor describes transformations that do not lead to a change in the position vector $\vec{r}$ relative to the coordinate system embedded in the material; that is, the tensor describes deformations which are

not translations or rotations. The left Cauchy-Green tensor, $\mathbf{B}$, is defined in terms of the deformation gradient, (7.2), as

$$\begin{aligned}\mathbf{B}(t,R) &= \mathbf{F}(t,R)\cdot\big(\mathbf{F}(t,R)\big)^{\mathrm{T}}\\ &= h^2(t,R)\hat{\mathrm{e}}_r\hat{\mathrm{e}}_r + \frac{f^2(t,R)}{R^2}\hat{\mathrm{e}}_\theta\hat{\mathrm{e}}_\theta + \hat{\mathrm{e}}_z\hat{\mathrm{e}}_z,\end{aligned} \tag{7.4}$$

where $(\cdot)^{\mathrm{T}}$ denotes the transpose operation. The principal invariants of $\mathbf{B}$ are

$$\begin{cases} I_1 = h^2(t,R) + \frac{f^2(t,R)}{R^2} + 1\\ I_2 = h^2(t,R)\frac{f^2(t,R)}{R^2} + h^2(t,R) + \frac{f^2(t,R)}{R^2}\\ I_3 = h^2(t,R)\frac{f^2(t,R)}{R^2}. \end{cases} \tag{7.5}$$

Assuming brain tissue to be incompressible requires that the third principal invariant be unitary. This implies that

$$I_3 = \frac{h^2(t,R)f^2(t,R)}{R^2} = 1.$$

Integrating, we find that the deformation function f must be of the form

$$f(t,R) = \sqrt{R^2 + A(t)}, \tag{7.6}$$

where $A(t)$ is a function to be determined such that $A(0) = 0$. Furthermore,

$$h(t,R) = \frac{\partial f}{\partial R}(t,R) = \frac{R}{\sqrt{R^2 + A(t)}}. \tag{7.7}$$

Substituting (7.6) and (7.7) into the left Cauchy-Green tensor (7.4) gives

$$\mathbf{B}(t,R) = \frac{R^2}{R^2 + A(t)}\hat{\mathrm{e}}_r\hat{\mathrm{e}}_r + \frac{R^2 + A(t)}{R^2}\hat{\mathrm{e}}_\theta\hat{\mathrm{e}}_\theta + \hat{\mathrm{e}}_z\hat{\mathrm{e}}_z. \tag{7.8}$$

The symmetric part of the velocity gradient tensor, $\boldsymbol{\nabla}\mathbf{v}$, where $\vec{v} = \frac{\partial\vec{r}}{\partial t}$ is the velocity, defines the rate-of-strain tensor, $\mathbf{D} = \frac{1}{2}\left(\boldsymbol{\nabla}\mathbf{v} + \boldsymbol{\nabla}\mathbf{v}^{\mathrm{T}}\right)$. Using the Caputo definition of the fractional derivative of a function $g(t)$ [66, Eq. 6],

$$D^\alpha g(t) = \frac{1}{\Gamma(1-\alpha)}\int_0^t \frac{1}{(t-s)^\alpha}\,\dot{g}(s)\mathrm{d}s, \tag{7.9}$$

where $\dot{g}(t) = \frac{\mathrm{d}g}{\mathrm{d}t}$, and generalizing to three dimensions, gives the fractional rate-of-strain tensor, $\mathbf{D}^{\{\alpha\}}$ [30, equation 4.2.10], as

$$\mathbf{D}^{\{\alpha\}}(t,R) = \frac{1}{\Gamma(1-\alpha)}\int_0^t \frac{1}{(t-\tau)^\alpha}\big(\mathbf{F}_{\boldsymbol{\tau}}(t,R)\big)^{\mathrm{T}}\cdot\mathbf{D}(\tau,R)\cdot\mathbf{F}_{\boldsymbol{\tau}}(t,R)\,\mathrm{d}\tau.$$

Substituting (7.3), (7.6), and (7.7) into the above expression gives

$$\begin{aligned}\mathbf{D}^{\{\alpha\}}(t,R) = \frac{1}{2\Gamma(1-\alpha)}\int_0^t \frac{1}{(t-\tau)^\alpha}\Bigg(&\frac{-\dot{A}(\tau)}{R^2 + A(t)}\hat{\mathrm{e}}_r\hat{\mathrm{e}}_r\\ &+ \frac{\dot{A}(\tau)\big(R^2 + A(t)\big)}{\big(R^2 + A(\tau)\big)^2}\hat{\mathrm{e}}_\theta\hat{\mathrm{e}}_\theta\Bigg)\mathrm{d}\tau.\end{aligned} \tag{7.10}$$

The Constitutive Equation

We assume that infant brain tissue can be modelled as a Kelvin-Voigt solid, schematically represented by an elastic spring connected in parallel to a viscous dashpot, see Figure 7.1b. The Cauchy stress tensor thus has the form $\boldsymbol{\sigma} = \boldsymbol{\sigma}_\mathbf{e} + \boldsymbol{\sigma}_\mathbf{v}$, where $\boldsymbol{\sigma}_\mathbf{e}$ is the stress in the spring and $\boldsymbol{\sigma}_\mathbf{v}$ is the stress in the dashpot.

At small strains and uniaxial loading, the constitutive equation of a linear elastic spring satisfies Hooke's law, $\sigma_\mathrm{e} = E\varepsilon$. For finite strains, the spring is assumed to be a homogeneous, isotropic, hyperelastic material. Thus, the constitutive equation for the hyperelastic spring is defined in terms of the strain energy density function, $W = W(\mathbf{B})$, via

$$\boldsymbol{\sigma}_\mathbf{e} = \frac{2}{\sqrt{I_3}}\left[\left(\frac{\partial W}{\partial I_1} + I_1\frac{\partial W}{\partial I_2}\right)\mathbf{B} - \frac{\partial W}{\partial I_2}\mathbf{B}^2\right] + 2\sqrt{I_3}\frac{\partial W}{\partial I_3}\mathbf{I}, \tag{7.11}$$

where $\mathbf{I}$ is the identity tensor, $\mathbf{B}$ is the left Cauchy-Green deformation tensor (7.8), and I_1, I_2, and I_3 are the principal invariants of $\mathbf{B}$ (7.5).

At small strains and uniaxial loading, a linear viscous dashpot has constitutive equation $\sigma_v = \eta\dot{\varepsilon}$ and a fractional viscous dashpot has constitutive equation $\sigma_v = \eta D^\alpha\varepsilon$. For finite strains, the fractional derivative of the strain is replaced by the fractional rate-of-strain tensor, $\mathbf{D}^{\{\alpha\}}$, which gives the constitutive equation

$$\boldsymbol{\sigma}_\mathbf{v} = 2\eta\mathbf{D}^{\{\alpha\}}. \tag{7.12}$$

Our assumption of incompressibility requires that there is no net change in volume, $I_3 = 1$, and since the material is isotropic, the strain energy density function does not depend on I_3. Thus, the constitutive equation for the Kelvin-Voigt material simplifies to

$$\boldsymbol{\sigma}_\mathbf{e} + \boldsymbol{\sigma}_\mathbf{v} = 2\left[\left(\frac{\partial W}{\partial I_1} + I_1\frac{\partial W}{\partial I_2}\right)\mathbf{B} - \frac{\partial W}{\partial I_2}\mathbf{B}^2\right] + 2\eta\mathbf{D}^{\{\alpha\}}.$$

This expression describes the deviatoric part of the stress. To include dilatational stress we add a hydrostatic pressure term. This term imparts no net work on the incompressible material since any work done would have to be through a change in volume, and an incompressible material undergoes no volume change under hydrostatic pressure. Therefore, the complete constitutive equation for the fractional Kelvin-Voigt material is

$$\boldsymbol{\sigma} = -q\mathbf{I} + 2\left[\left(\frac{\partial W}{\partial I_1} + I_1\frac{\partial W}{\partial I_2}\right)\mathbf{B} - \frac{\partial W}{\partial I_2}\mathbf{B}^2\right] + 2\eta\mathbf{D}^{\{\alpha\}}. \tag{7.13}$$

Constitutive equation (7.13) determines the stress state only up to an arbitrary function $-q\mathbf{I}$. It is better to think of q as a Lagrange multiplier used to enforce incompressibility rather than as a hydrostatic pressure or internal tissue pressure that can be measured by a transducer.

We assume that the strain energy density function of the soft brain tissue can be described by the Mooney-Rivlin model,

$$W = c_{10}(I_1 - 3) + c_{01}(I_2 - 3), \tag{7.14}$$

where c_{10} and c_{01} are material parameters. Substituting this strain energy density into the constitutive equation (7.13) gives

$$\boldsymbol{\sigma} = -q\mathbf{I} + 2\left(c_{10} + c_{01}\left(h^2 + \frac{f^2}{R^2} + 1\right)\right)\mathbf{B} - 2c_{01}\mathbf{B}^2 + 2\eta\mathbf{D}^{\{\alpha\}}.$$

Since $\mathbf{I}$, $\mathbf{B}$, $\mathbf{B}^2$, and $\mathbf{D}^{\{\alpha\}}$ are all diagonal tensors, $\boldsymbol{\sigma}$ must also be a diagonal tensor of the form $\boldsymbol{\sigma} = \sigma_r\hat{\mathbf{e}}_r\hat{\mathbf{e}}_r + \sigma_\theta\hat{\mathbf{e}}_\theta\hat{\mathbf{e}}_\theta + \sigma_z\hat{\mathbf{e}}_z\hat{\mathbf{e}}_z$. Substituting the expressions for $\mathbf{B}$ (7.8) and $\mathbf{D}^{\{\alpha\}}$ (7.10) gives the components of the stress tensor as

$$\begin{aligned}\sigma_r(t,R) = -q + 2\left(c_{10} + c_{01}\left(h^2(t,R) + \frac{f^2(t,R)}{R^2} + 1\right)\right)h^2(t,R) \\ - 2c_{01}h^4(t,R) + \frac{2\eta}{\Gamma(1-\alpha)}\int_0^t \frac{1}{(t-\tau)^\alpha}\frac{h^2(t,R)h_t(\tau,R)}{h^3(\tau,R)}\,\mathrm{d}\tau,\end{aligned} \tag{7.15}$$

$$\begin{aligned}\sigma_\theta(t,R) = -q + 2\left(c_{10} + c_{01}\left(h^2(t,R) + \frac{f^2(t,R)}{R^2} + 1\right)\right)\frac{f^2(t,R)}{R^2} \\ - 2c_{01}\frac{f^4(t,R)}{R^4} + \frac{2\eta}{\Gamma(1-\alpha)}\int_0^t \frac{1}{(t-\tau)^\alpha}\frac{f^2(t,R)f_t(\tau,R)}{f^3(\tau,R)}\,\mathrm{d}\tau,\end{aligned} \tag{7.16}$$

and

$$\sigma_z(t,R) = -q + 2\left(c_{10} + c_{01}\left(h^2(t,R) + \frac{f^2(t,R)}{R^2} + 1\right)\right) - 2c_{01}. \tag{7.17}$$

The Equation of Motion

In the absence of body forces, conservation of momentum gives the equilibrium equation $\vec{\nabla}\cdot\boldsymbol{\sigma} = 0$, and since σ_r, σ_θ, and σ_z only depend on r and t, the equation of motion is

$$\frac{\partial\sigma_r}{\partial r} + \frac{1}{r}(\sigma_r - \sigma_\theta) = 0. \tag{7.18}$$

Introducing the notation for the boundaries of the cylindrical brain at time t as $r_1 = f(t, R_1)$ and $r_2 = f(t, R_2)$, the boundary conditions enforced for the infant hydrocephalic brain are

$$\sigma_r(t, r_1) = -p_0(t) \qquad \text{and} \qquad \sigma_r(t, r_2) = 0. \tag{7.19}$$

Note that, again, we use the simple stress-free outer boundary condition. Integrating the equation of motion (7.18) over the brain parenchyma and applying

the boundary conditions (7.19) gives

$$p_0(t) = \int_{r_1}^{r_2} \frac{1}{r}(\sigma_\theta - \sigma_r)\,\mathrm{d}r. \tag{7.20}$$

Changing the variable of integration from r to R via $r = f(t, R)$ and then to the dimensionless variable of integration x via $R^2 = R_1^2 x$ gives, after simplification, the equation of motion that we wish to solve,

$$\begin{aligned} p_0(t) = \frac{\mu}{2}\int_1^b \left(\frac{1}{x} - \frac{x}{\big(x + B(t)\big)^2}\right)\mathrm{d}x \\ + \frac{\eta}{2\Gamma(1-\alpha)}\int_0^t \frac{\dot{B}(\tau)}{(t-\tau)^\alpha}\int_1^b \left(\frac{1}{\big(x + B(\tau)\big)^2} + \frac{1}{\big(x + B(t)\big)^2}\right)\mathrm{d}x\,\mathrm{d}\tau, \end{aligned} \tag{7.21}$$

where $B(t) = R_1^{-2}A(t)$, $b = \left(\frac{R_2}{R_1}\right)^2$, and $\mu = 2(c_{10} + c_{01})$ is the shear modulus.

7.1.2 The Small Strain Solution

As a first approximation, we solve the equation of motion (7.21) using the assumption of small strains ($B(t) \ll 1$). After introducing this approximation and simplifying, the equation of motion becomes the linear integro-differential equation with Abel kernel,

$$\mu B(t) + \frac{\eta}{\Gamma(1-\alpha)}\int_0^t \frac{1}{(t-\tau)^\alpha}\dot{B}(\tau)\,\mathrm{d}\tau = \frac{b}{b-1}p_0(t). \tag{7.22}$$

Recognizing this integral from the Caputo definition of the fractional derivative (7.9) simplifies the notation, and the small strain equation of motion becomes

$$\mu B(t) + \eta D^\alpha B(t) = \frac{b}{b-1}p_0(t), \tag{7.23}$$

which is a fractional differential equation with initial condition $B(0) = 0$.

The Small Oscillations Response

We now analyze small steady oscillations of the brain parenchyma at the boundary in response to an internal pressure oscillation of the form $p_0(t) = P\cos\omega t = \mathrm{Re}\big(P\mathrm{e}^{i\omega t}\big)$. Here P is the amplitude and ω is the angular frequency of the oscillations.

Since we are interested in steady oscillations, and not in the effect of initial conditions, we replace the lower limit of integration in (7.22), 0, with $-\infty$, and seek a solution of the form $B(t) = \mathrm{Re}\left(B^*\mathrm{e}^{i\omega t}\right)$. Substituting $p_0(t)$ and $B(t)$ into the small strain equation of motion (7.22) gives

$$\mu B^*\mathrm{e}^{i\omega t} + \frac{\eta}{\Gamma(1-\alpha)}\int_{-\infty}^t \frac{1}{(t-\tau)^\alpha}B^* i\omega\mathrm{e}^{i\omega\tau}\,\mathrm{d}\tau = \frac{b}{b-1}P\mathrm{e}^{i\omega t}.$$

Changing the variable of integration to ξ via $\xi = t - \tau$ and then introducing $s = i\omega$ and using the Laplace Transform $\mathcal{L}\{\xi^{k-1}\} = \Gamma(k)s^{-k}$ for $k > 0$ [1, Eq. 29.3.7] allows the integral to be evaluated. After simplifying, the complex amplitude of the oscillations is $B^* = \dfrac{bP}{(b-1)(\mu + \eta(i\omega)^\alpha)}$, and thus

$$B(t) = \frac{bP}{b-1} \frac{\left(\mu + \eta\omega^\alpha \cos\frac{\pi\alpha}{2}\right)\cos\omega t + \eta\omega^\alpha \sin\frac{\pi\alpha}{2}\sin\omega t}{\left(\mu + \eta\omega^\alpha \cos\frac{\pi\alpha}{2}\right)^2 + \left(\eta\omega^\alpha \sin\frac{\pi\alpha}{2}\right)^2}.$$

A more biologically relevant form of the internal pressure is the combination of a constant pressure and an oscillatory pressure, $p_0(t) = P_c + P_o \cos\omega t$, corresponding to oscillations from $P_c - P_o$ to $P_c + P_o$. Since the small strain equation of motion (7.22) is linear, the long-time solution due to an internal pressure of this form is the sum of a constant solution and a periodic solution. The steady-state solution to (7.22) with a constant internal pressure $p_0(t) = P_c$ is simply $B_c = \frac{b}{b-1}\frac{P_c}{\mu}$. Introducing $\tilde{A}$ and ϕ via

$$\tilde{A} = \left(\mu^2 + \eta^2\omega^{2\alpha} + 2\mu\eta\omega^\alpha \cos\frac{\pi\alpha}{2}\right)^{-\frac{1}{2}} \quad \text{and} \quad \phi = \arctan\left(\frac{\eta\omega^\alpha \sin\frac{\pi\alpha}{2}}{\mu + \eta\omega^\alpha \cos\frac{\pi\alpha}{2}}\right),$$

allows us to write the long-time solution to the small strain equation of motion (7.22) subject to an internal pressure of the form $p_0(t) = P_c + P_o\cos\omega t$ as

$$B(t) = \frac{b}{b-1}\left(\frac{P_c}{\mu} + P_o\tilde{A}\cos(\omega t - \phi)\right). \tag{7.24}$$

The Step Response

The previous section solved the small strain equation of motion (7.23) for the long-time oscillatory response of the material to periodic pressure gradients. In this section, we investigate the step response of the material for a special form of the fractional order. If $\alpha = \frac{n}{m}$, where n and m are positive integers satisfying $n < m$, then Laplace Transforms can be used to solve the small strain equation of motion (7.23).

The Laplace Transform of the fractional derivative of a causal function $f(t)$ is $\mathcal{L}\{D^\alpha f(t)\} = s^\alpha \bar{F}(s)$, where $\bar{F}(s)$ is the Laplace Transform of $f(t)$. Assuming $p_0(t) = \Delta p H(t)$, where $H(t)$ is the Heaviside function, then the Laplace Transform of $p_0(t)$ is $\mathcal{L}\{p_0(t)\} = \Delta p\frac{1}{s}$. Using the Laplace Transform to solve the small strain equation of motion (7.23) with the initial condition $B(0) = 0$, gives, after simplification,

$$\bar{B}(s) = \frac{b}{b-1}\frac{\Delta p}{\mu}\left(\frac{1}{s} - \frac{s^{\alpha-1}}{s^\alpha + \frac{\mu}{\eta}}\right). \tag{7.25}$$

This expression can be simplified further once the value of $\alpha = \frac{n}{m}$ is known [81]. We find the response of the fractional viscoelastic material to a 20 Pa instantaneous jump in internal pressure for five values of α ($\alpha = \frac{1}{3}$, $\frac{1}{2}$, $\frac{2}{3}$, $\frac{3}{4}$, and $\frac{4}{5}$).

The solution method is now demonstrated for the simplest case, $\alpha = \frac{1}{2}$, and a demonstration of the solution method for $\alpha = \frac{4}{5}$ is provided in Appendix C.

In order to apply the inverse Laplace Transform to (7.25), long division of polynomials and partial fraction expansions are required to rewrite the second term in the parentheses in a form appropriate for the inverse Laplace integral. For $\alpha = \frac{1}{2}$, let $\beta = \frac{\mu}{\eta}$, and rewrite the fractional order term to get the following expression for $\bar{B}(s)$,

$$\bar{B}(s) = \frac{b}{b-1}\frac{\Delta p}{\mu}\left(\frac{1}{s} - \frac{1}{s-\beta^2} + \frac{\beta s^{-\frac{1}{2}}}{s-\beta^2}\right).$$

Then, taking the inverse Laplace Transform and simplifying gives

$$B(t) = \frac{b}{b-1}\frac{\Delta p}{\mu}\left(1 - \mathrm{e}^{\beta^2 t} + \mathrm{e}^{\beta^2 t}\,\mathrm{erf}\left(\beta\sqrt{t}\right)\right)H(t),$$

where $\mathrm{erf}(z) = \frac{2}{\sqrt{\pi}}\int_0^z \mathrm{e}^{-t^2}\,\mathrm{d}t$ is the error function. Using the complimentary error function, $\mathrm{erfc}(z) = 1 - \mathrm{erf}(z)$, the expression for $B(t)$ becomes

$$B(t) = \frac{b}{b-1}\frac{\Delta p}{\mu}\left(1 - \mathrm{e}^{\beta^2 t}\,\mathrm{erfc}\left(\beta\sqrt{t}\right)\right)H(t). \tag{7.26}$$

7.1.3 The Quasilinear Equation

Without the assumption of small strains, the quasilinear equation of motion (7.21) can be simplified by directly evaluating the integrals over x. This gives the following nonlinear integro-differential equation for $B(t)$:

$$\begin{aligned} p_0(t) = \frac{\mu}{2}&\left(\ln\left(\frac{b\big(1+B(t)\big)}{b+B(t)}\right) + \frac{(b-1)B(t)}{\big(1+B(t)\big)\big(b+B(t)\big)}\right) \\ &+ \frac{\eta}{2\Gamma(1-\alpha)}\int_0^t \frac{\dot{B}(\tau)}{(t-\tau)^\alpha}\left(\frac{1}{1+B(\tau)} - \frac{1}{b+B(\tau)}\right)\mathrm{d}\tau \\ &+ \frac{\eta}{2\Gamma(1-\alpha)}\frac{b-1}{\big(1+B(t)\big)\big(b+B(t)\big)}\int_0^t \frac{\dot{B}(\tau)}{(t-\tau)^\alpha}\,\mathrm{d}\tau. \end{aligned} \tag{7.27}$$

Again, using the notation for the Caputo fractional derivative (7.9), this equation can be written more simply as

$$\begin{aligned} p_0(t) = \frac{\mu}{2}&\left(\ln\left(\frac{b\big(1+B(t)\big)}{b+B(t)}\right) + \frac{(b-1)B(t)}{\big(1+B(t)\big)\big(b+B(t)\big)}\right) \\ &+ \frac{\eta}{2}\left(D^\alpha \ln\left(\frac{1+B(t)}{b+B(t)}\right) + \frac{b-1}{\big(1+B(t)\big)\big(b+B(t)\big)}D^\alpha B(t)\right). \end{aligned} \tag{7.28}$$

To compute the components of the stress tensor (7.15)–(7.17), the value of the Lagrange multiplier, q, must be determined. This is done by integrating the

equilibrium equation (7.18) from r_1 to r and solving for q. The expression for the radial stress becomes

$$\begin{aligned}\sigma_r(t,R) = &- p_0(t) + \frac{\mu}{2}\left(\ln\left(\frac{g\big(1+B(t)\big)}{g+B(t)}\right) + \frac{(g-1)B(t)}{\big(1+B(t)\big)\big(g+B(t)\big)}\right)\\ &+ \frac{\eta}{2}\left(D^\alpha \ln\left(\frac{1+B(t)}{g+B(t)}\right) + \frac{(g-1)D^\alpha B(t)}{\big(1+B(t)\big)\big(g+B(t)\big)}\right),\end{aligned} \tag{7.29}$$

and the expression for the tangential stress becomes

$$\begin{aligned}\sigma_\theta(t,R) = &- p_0(t) + \frac{\mu}{2}\left(\ln\left(\frac{g\big(1+B(t)\big)}{g+B(t)}\right) + \frac{(g-1)B(t)}{\big(1+B(t)\big)\big(g+B(t)\big)}\right)\\ &+ \frac{\eta}{2}\left(D^\alpha \ln\left(\frac{1+B(t)}{g+B(t)}\right) + \frac{(g-1)D^\alpha B(t)}{\big(1+B(t)\big)\big(g+B(t)\big)}\right)\\ &+ \eta\left(\frac{g}{g+B(t)}D^\alpha\left(\frac{g+B(t)}{g}\right) - \frac{g+B(t)}{g}D^\alpha\left(\frac{g}{g+B(t)}\right)\right)\\ &+ \mu\frac{\big(2g+B(t)\big)B(t)}{g\big(g+B(t)\big)}\end{aligned} \tag{7.30}$$

where g is a function of R defined by $g = \dfrac{R^2}{R_1^2}$ and so $1 \le g \le b$.

7.2 Numerical Simulations

Numerical simulations of the radial displacement at the inner and outer boundaries demonstrate the behaviour of the brain parenchyma under the assumed pressure gradient, $p_0(t)$. The ventricle wall (inner boundary at $r = r_1$) and the cortical surface (outer boundary at $r = r_2$) are given by

$$\begin{aligned} r_1(t) &= f(t,R_1) = R_1\sqrt{1+B(t)},\\ r_2(t) &= f(t,R_2) = R_2\sqrt{1+\frac{1}{b}B(t)}.\end{aligned}$$

Furthermore, the displacement of each boundary from its initial position is given by $u_1(t) = r_1(t) - R_1$ (inner boundary) and $u_2(t) = r_2(t) - R_2$ (outer boundary), and the parenchyma width is given by $w(t) = r_2(t) - r_1(t)$.

The model parameters used to compute the displacements numerically are listed in Table 7.1. The initial positions of the ventricle wall and cortical surface are based on a 35 cm newborn head circumference. The values of the shear modulus μ, the viscosity η, and the fractional order α, are taken from Chapter 6 (also [131]) where the fractional Zener viscoelastic model was fitted to experimental data for infant porcine cerebrum. Note that the viscosity from Chapter 6 (0.66 Pa·s) is used here as an approximation to the viscosity required in this fractional viscoelastic model, which has viscosity units of Pa·s$^\alpha$.

Table 7.1: Hyper-viscoelastic model parameter values for the infant brain.

$R_1 = 2$ cm	$R_2 = 6$ cm	$b = \left(\frac{R_2}{R_1}\right)^2 = 9$
$\mu = 207$ Pa [131]	$\eta = 0.66$ Pa·s$^\alpha$ [131]	$\alpha = 0.779$ [131]
$P_c = 20$ Pa	$P_o = 20$ Pa	$\omega = 7$ rad s^{-1} [131]

7.2.1 Small Strain Oscillations

For small oscillations in the pressure gradient, the amplitudes P or P_c and P_o, must be chosen so that the small strain assumption is valid. For simplicity we assume $P_c = P_o = P$, then under a constant and dynamic pressure gradient, assuming $B(t) \ll 1$ requires that for all t,

$$P \ll \frac{b-1}{b} \cdot \frac{\mu}{1 + \mu \tilde{A} \cos(\omega t - \phi)}.$$

Using the parameter values from Table 7.1 the above constraint requires that $P \ll 90$ Pa for the small strain assumption to be valid. Therefore, the amplitudes of the constant and dynamic pressure gradients are chosen to be 20 Pa or less.

The predicted displacements of the inner and outer boundaries due to a constant and dynamic pressure gradient of the form $p_0(t) = P(1 + \cos \omega t)$ Pa are given in Figure 7.2a. The displacement due to a constant pressure gradient of 20 Pa is 1.06 mm at the ventricle wall and 0.36 mm at the cortical surface. Note that these predictions use a shear modulus that is based on the steady-state elastic modulus from Table 6.2 from Chapter 6. Thus, this shear modulus is actually the steady-state shear modulus and it describes the material's long-time response to shear strains. For oscillations on the order of the heart beat, as simulated here, a more appropriate value of the shear modulus would be one based on the initial elastic modulus from Table 6.2, that is, a value of $\mu = \frac{E_0}{3} \approx 2226$ Pa. Such a value would predict displacements of about 100 μm at the ventricle wall and 34 μm at the cortical surface. For very slow oscillations in the pressure, however, the long-time shear modulus is appropriate, and significant displacements can occur from seemingly small pressure gradients. The long-time shear modulus is used in these oscillatory predictions to maintain consistency with predictions made in the remainder of this Chapter.

Model Sensitivity Analysis

To investigate the model's sensitivity to the values of the parameters, the shear modulus, μ, viscosity, η, and fractional order, α, are varied. The predicted maximum displacements are normalized with the maximum displacement of the ventricle wall obtained using the parameter values from Table 7.1 and the results are plotted in Figure 7.2. Oscillatory pressure gradients of the form $p_0(t) = 20 \cos \omega t$ Pa were used.

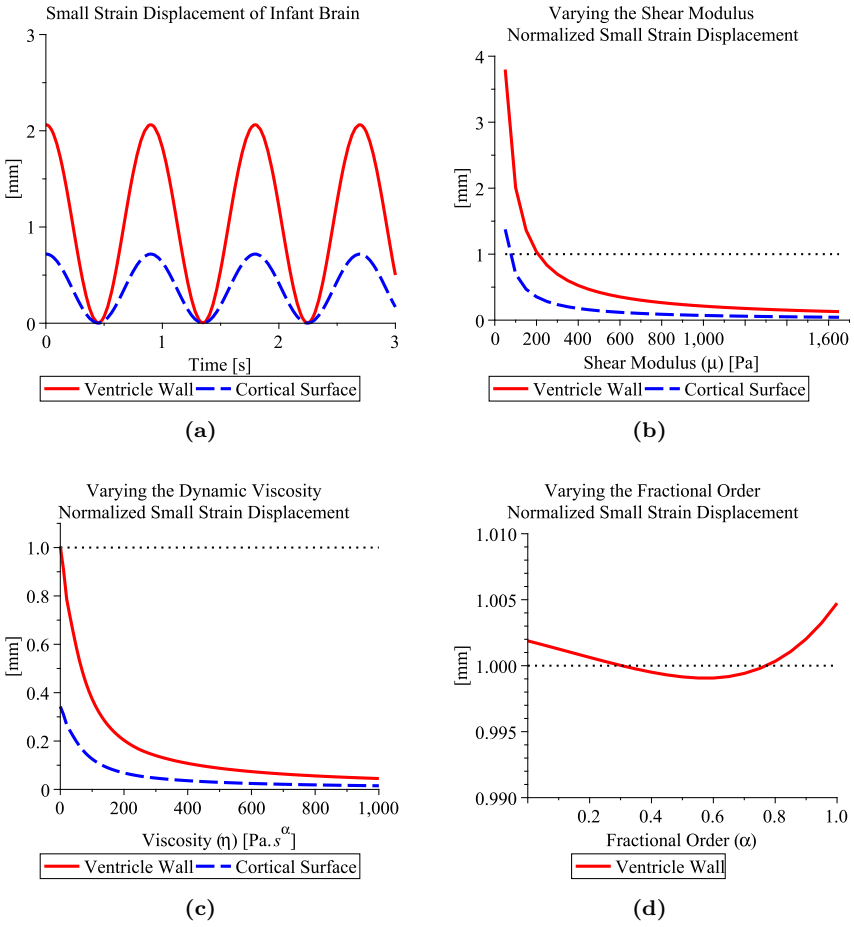

Figure 7.2: Simulated small strain displacements of the ventricle wall ($r = r_1$) and cortical surface ($r = r_2$) of the infant brain under a pressure gradient of the form $p_0(t) = 20(1 + \cos \omega t)$ Pa, (a), and the sensitivity of the displacements to variations in the shear modulus, (b), viscosity, (c), and fractional order, (d), under an oscillatory pressure gradient $p_0(t) = 20 \cos \omega t$ Pa, normalized by the maximum displacement of the ventricle wall due to a 20 Pa pressure gradient (1.06 mm).

From the form of the small strain solution for constant pressure gradients, $B_c = \frac{b}{b-1}\frac{P}{\mu}$, we see that only the shear modulus affects the boundary displacements, and the displacements decrease proportionally to $\frac{1}{\mu}$. Under an oscillatory pressure gradient, increasing either the shear modulus or the dynamic viscosity causes the maximum displacements of the parenchyma boundaries to decrease with increasing μ or η. Varying the fractional order under an oscillatory pressure gradient has a small effect on the maximum boundary displacements with

the maximum displacement occurring when $\alpha = 1$ and the minimum occurring when $\alpha \approx 0.6$.

The sensitivities of the predicted displacements to the model parameter values demonstrate the importance of using tissue-dependent parameter values in the numerical simulations. The displacements predicted here, using the infant brain tissue parameter values listed in Table 7.1, would be quite different if the initial elastic modulus was used to determine the shear modulus or if standard adult brain tissue parameter values were used. A larger shear modulus or viscosity would predict significantly less deformation of the brain tissue.

7.2.2 Small Strain Step Response

From the expression for $B(t)$ when $\alpha = \frac{1}{2}$ (7.26), we can estimate the effect of the fractional derivative in the viscoelastic material. Assuming a tolerance of 10^{-3}, a simple calculation shows that the effect of the fractional derivative is present in $B(t)$ for approximately 3.7 s before the steady-state value ($B_c = \frac{b}{b-1}\frac{\Delta p}{\mu}$) is reached. Displacements at the ventricle wall and cortical surface boundaries of the brain are shown in Figure 7.3 for $\alpha = \frac{1}{3}$, $\frac{1}{2}$, $\frac{2}{3}$, $\frac{3}{4}$, and $\frac{4}{5}$.

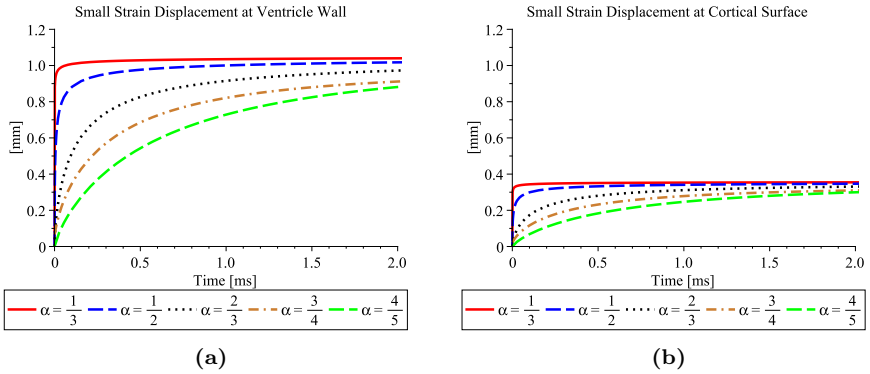

Figure 7.3: Response of the fractional hyper-viscoelastic material to a 20 Pa instantaneous change in pressure for five values of the fractional order α.

As α approaches zero, the displacements approach the instantaneous elastic response. As α approaches unity, the effect of the fractional derivative (viscous element) becomes more pronounced and more prolonged in the step response before the steady-state value is reached. For infant cerebrum $\alpha \approx \frac{4}{5}$ and the viscous component delays the hyper-viscoelastic materials response to the instantaneous change. Given sufficient time, however, the material will reach the steady-state value which is determined by the hyperelastic component of the constitutive equation. This justifies ignoring the strain rate dependence when considering the long-time behaviour of brain tissue as was done by Dutta-Roy, Wittek, and Miller [31], and as is done in the following section.

7.2.3 Incremental Approximation to Finite Strains

Ideally, we would like a solution to the quasilinear equation of motion (7.21) that does not assume small strains, so that large deformations can be predicted accurately. Unfortunately, the quasilinear equation is difficult to solve analytically; however, we can approximate a finite strain deformation by incrementally solving for small strain solutions and summing the resulting deformations [20]. This iterative numerical technique is based on the incremental law discussed by Fung [42, pg. 238–9]; using uniaxial tension tests he demonstrated that sequential small strain loading-unloading loops are a good approximation to the finite-strain loading-unloading loop.

To approximate the finite deformation resulting from a large pressure gradient, Δp, we divide this gradient into n small uniform pieces, δp, so that $n\delta p = \Delta p$. The sum of the deformations caused by each incremental gradient, δp, approximates the finite deformation that would have resulted from the pressure gradient Δp. If δp is sufficiently small, then the resulting long-time displacement can be approximated by the steady-state small strain solution to a constant pressure gradient. Thus, the incremental displacement is

$$u(t,R) = \sqrt{R^2 + R_1^2 B_c} - R \qquad \text{where} \qquad B_c = \frac{b}{b-1}\frac{\delta p}{\mu}.$$

After the application of each incremental pressure gradient, δp, the steady-state solution gives the new position of the parenchyma boundaries, and so R_1, R_2, and b must be updated to reflect the new deformed state. Iterating in this manner produces a series of displacements whose sum approximates the displacement that would have resulted from the application of the large pressure gradient, Δp.

In Figure 7.4a, the small strain solution is summed for pressure gradient increments of size $\delta p = 1$, 5, 10, and 20 Pa. The shear modulus value and the initial values of R_1 and R_2 are listed in Table 7.1. As expected, the width of the parenchyma decreases as the incremental pressure gradients accumulate. A reduction in width of about 50% occurs when the total applied pressure gradient, Δp, is about 350 to 400 Pa. This range is approximately 2.5 to 3.0 mm Hg which is biologically reasonable and is comparable to the amplitude of cerebrospinal fluid pressure pulsations in normal ventricles (5 mm Hg peak-to-peak). The difference, however, is that the pressure gradients here are assumed to be held constant for long times instead of oscillating with the cardiac and respiratory cycles. Figure 7.4b displays the width of the brain tissue for various shear moduli and an incremental pressure gradient of $\delta p = 5$ Pa. When reducing the width by 50%, doubling the shear modulus requires approximately double the total pressure gradient, Δp, when applied in increments small enough to satisfy the small strain assumption.

The Evans ratio is a diagnostic tool for identifying hydrocephalus. It is defined as the ratio of the maximum width of the frontal horns to the maximum width of the brain parenchyma. A ratio greater than 0.4 indicates a

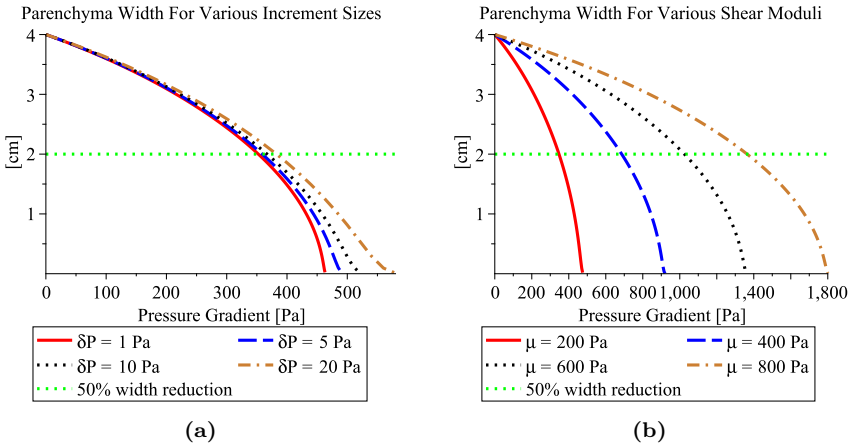

Figure 7.4: Parenchyma width due to a pressure gradient divided into increments of 1, 5, 10, and 20 Pa ($\mu = 207$ Pa), (a), and parenchyma width for various shear moduli values due to a pressure gradient divided into increments of 5 Pa, (b).

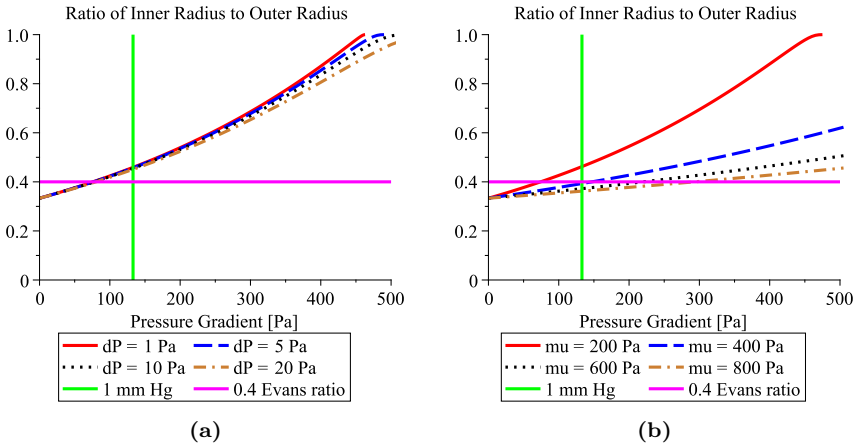

Figure 7.5: Evans Ratio $\left(\frac{r_1(t)}{r_2(t)}\right)$ due to a pressure gradient divided into increments of 1, 5, 10, and 20 Pa ($\mu = 207$ Pa), (a), and for various shear moduli due to a pressure gradient divided into increments of 5 Pa, (b).

hydrocephalic brain [125]. Figure 7.5 shows the ratio of the inner radius to the outer radius, the Evans ratio for our cylindrical model geometry, as both the pressure gradient increment and shear modulus are varied. It is clear that with a shear modulus of 200 Pa, a 1 mm Hg pressure gradient is sufficient to cause the development of hydrocephalus in this simplified model. As the shear

modulus increases, however, this gradient is not sufficient, and other possible factors, such as fluid absorption by the parenchyma, would be required to expand the ventricles. It should be noted that these results are dependent on the initial configuration and geometry of the model; however, they do suggest that the infant brain may develop hydrocephalus in the presence of a small pressure gradient. Furthermore, aging brain tissues, with reduced values of various mechanical parameters, appear to be susceptible to large deformations and to the development of hydrocephalus. The necessity of accurate mechanical parameter values for accurate tissue deformation predictions is also demonstrated.

The advantage of this iterative method in predicting ventricular expansion is that large strains are never required to occur in the material. This is consistent with the belief that hydrocephalus develops slowly over time due to the accumulation of small strains [65, 69]. The pressure gradient accumulates over such a long period of time that the living tissue is able to deform with small strains in response to the gradient increments. The tissue may then, in response to the mechanical stimuli of these small structural stresses, reorganize its cell-ECM structure to reduce these stresses. With the build-up of another increment in pressure, the process may start over again, eventually resulting in a large deformation without large strains, and an new configuration of the cell-ECM structure.

7.2.4 Quasilinear Solution Simulations

To solve the quasilinear equation of motion (7.28), we assume that $\alpha = 1$ so that the fractional derivatives become first order derivatives. Assigning a pressure gradient that starts at zero and increases to a maximum of 100 Pa,

$$p_0(t) = 100(1 - \mathrm{e}^{-10t}), \tag{7.31}$$

we can solve the first order quasilinear differential equation numerically using the `dsolve` command in `MAPLE` and the initial condition $B(0) = 0$. The displacement at the ventricle wall and the parenchyma width reduction resulting from the application of pressure gradient (7.31) to the quasilinear equation of motion (7.28) with $\alpha = 1$ are shown in Figure 7.6. Model parameter values for b and η are taken from Table 7.1.

With first order derivatives, the quasilinear equation predicts that a 100 Pa pressure gradient displaces the ventricle wall by about 0.8 cm and decreases the parenchyma width by about 0.5 cm, assuming a shear modulus of 200 Pa. This displacement doubles the planar area of the ventricle. Comparing the reduction in parenchyma width due to a 100 Pa pressure gradient predicted by the quasilinear equation with $\alpha = 1$ to the incremental method simulations, Figure 7.4, shows that they are in approximate agreement with each other. The parenchyma width reduction predicted by this model is significant for a pressure gradient on the order of 1 mm Hg, especially when the shear modulus is reduced, as is the case for infant brain tissue.

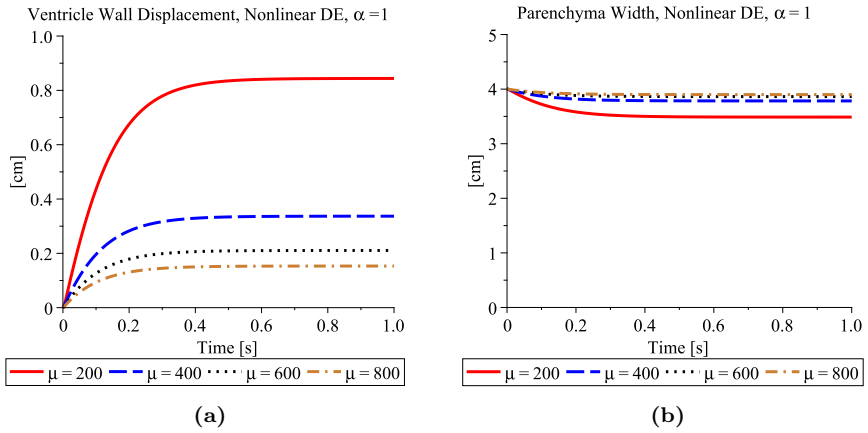

Figure 7.6: Displacement of the ventricle wall (a) and the width of the parenchyma (b) according to the quasilinear DE with $\alpha = 1$ due to a pressure gradient of the form (7.31) for various shear moduli.

Analysis of the radial and tangential stresses indicates that as the pressure gradient increases, both stresses become infinite. This behaviour is not physical; at some threshold value for the tangential stress (tensile component), the brain tissue will become damaged and this hyper-viscoelastic mathematical model will no longer provide a valid description of the material behaviour. This model does, however, indicate that stresses large enough to cause tissue damage can occur under sufficiently large pressure gradients, and that the damaging gradient threshold will depend on the shear modulus, and thus the age, of the tissue.

7.3 Discussion

In this Chapter, a fractional derivative hyper-viscoelastic model was developed to describe the behaviour of infant brain tissue under loading conditions consistent with the development of pediatric communicating hydrocephalus. Using model parameter values appropriate for infant parenchyma, it has been demonstrated that pressure gradients of 1 mm Hg are sufficient to cause ventricular expansion.

Using the assumption of small strains, the response of the fractional hyper-viscoelastic material was determined for pressure gradients with small oscillations and instantaneous jumps. The small oscillations response predicts the motion of the brain parenchyma due to the small amplitude pulsatile loading of the ventricle wall. The resulting waves travel through the incompressible material without accruing any phase shift, a simplified approximation of the physical behaviour of wave propagation through the cell, extracellular matrix, and extracellular fluid system, of which all biological tissues are comprised.

Laplace Transforms were used to find the step response of the small strain equation of motion for various values of the fractional order. The step response demonstrates the effect of the fractional derivative and viscous component on material behaviour after an instantaneous increase in pressure. In Chapter 6, infant brain tissue was found to have a fractional order of about 0.8. In this case, the viscous component modifies the step response significantly when compared to the instantaneous jump to the steady-state value that occurs in the elastic limit ($\alpha = 0$). For long times, however, this viscous effect can be neglected since for all values of α, the step response eventually reaches the same elastic limit.

By summing the steady-state responses of the hyper-viscoelastic material to small increments in the pressure gradient, an approximation to the finite strain deformation was obtained. Figure 7.4 shows the relationship between the infant parenchyma width and the steady-state pressure gradient, and the Evans ratio plots in Figure 7.5 suggest that 1 mm Hg pressure gradients are sufficient to cause hydrocephalus in infants. Since the small strain solution is accumulated, these predicted finite deformations occur without large stresses, which is consistent with the belief that hydrocephalus develops slowly over time via the accumulation of small strains [65, 69]. Assuming that the pressure gradient increments accrue over very long times, the viscous component of the material can be neglected. Thus, the finite deformation is approximated by the sum of the steady-state hyperelastic responses to pressure gradient increments in this iterative numerical technique. This technique predicts the resulting parenchymal width reduction, or ventricular expansion, occurring as a result of pressure gradients applied for long times. This predictive tool could be used as an *in silico* experimental technique and will hopefully prove useful to both clinicians and experimentalists whose focus is on the development of a more fundamental understanding of, as well as the development of effective treatments for, hydrocephalus.

The quasilinear equation of motion was solved numerically after changing the fractional derivatives to first order derivatives. A pressure gradient that increases to a maximum of 100 Pa (7.31) was applied to simulate the slow evolution of a trans-parenchymal gradient. The resulting displacements were large enough to double the planar area of the ventricle assuming a shear modulus of 200 Pa. This deformation is significant and demonstrates that in infants, where the mechanical properties of brain tissue are lower than the corresponding properties for adult tissue, hydrocephalus can develop under sustained pressure gradients on the order of 1 mm Hg.

Both the radial and tangential stresses become large with increasing pressure. At the damage threshold, 2.71 kPa for white matter [40], these large stresses will initiate damage in the tissue, causing edemas to form near the ventricle wall where the stresses are largest. The long-time pressure gradient necessary to cause these damaging stresses depends on the shear modulus of the tissue. After the damage threshold is reached in terms of model stress, the mathematical model no longer provides a valid description of the dynamical phenomenon under consideration.

Recall that the recent work by Johnston and coworkers [86] showed that the dissociation of β_1-integrins from the surrounding extracellular matrix caused hydrocephalus to develop in rats. If this dissociation of the cells from the ECM degrades the macroscopic mechanical properties of the tissue, then, as was demonstrated here, the tissue will be more susceptible to deformations and to the development of hydrocephalus. It is therefore plausible that some cases of hydrocephalus are caused by microstructural changes in the tissue which degrade the macroscopic mechanical properties, enabling the tissue to deform grossly under a pressure gradient that in normal circumstances may not have much effect.

A transparenchymal pressure gradient of 1 mm Hg was shown here to be sufficient to cause hydrocephalus in the infant brain, where the long-time shear modulus is about 200 Pa. In adult brains, however, where the shear modulus is larger, this pressure gradient may be insufficient to cause hydrocephalus. It is most likely that hydrocephalus develops as a result of a combination of events. For example, microscopic changes may degrade the macroscopic mechanical properties, and disrupt tissue homeostasis by altering the delicate osmotic pressure balance. The gradual accumulation of a small pressure gradient due to this CSF production-absorption imbalance may then further increase the fluid absorption by the parenchyma by perturbing the Starling forces that govern transcapillary flow [65]. This may generate an intramantle pressure gradient in addition to a small transmantle pressure gradient. The reduced tissue mechanical properties and increased fluid absorption are sufficient to cause ventricular enlargement according to Peña *et al.* [93]. With the process of ventricular expansion initiated and the mechanical properties of the tissue degraded, ventricular CSF pressure waves may then increase in amplitude causing a dynamic pressure gradient and increasing the fluid filtration and tissue displacements in the periventricular region. Tissue damage and edemas may result from the combined effect of these events, and may not necessarily be attributable to any single event. This cascade of events, that on their own may be insufficient to cause ventriculomegaly, may combine to produce the conditions necessary for the development of hydrocephalus.

Finally, it should be noted that the finite deformations predicted by this fractional hyper-viscoelastic model are rough estimates of the true deformations due in part to the weak zero-stress boundary condition enforced at the infant skull boundary, and due in part to the simplified model of the mechanical behaviour and geometry of living brain tissue. In addition, the estimates of the mechanical parameters of infant brain tissue are subject to variation. All of these factors will have an impact on the predicted deformation; however, this is the first time, to our knowledge, that results of this nature have been presented. The results presented are clearly of significance for shunt planning and of relevance for experimental researchers as well as for clinicians involved in the treatment and management of hydrocephalus.

Chapter 8

Conclusions, Implications, Recommendations, and Future Work

In this final Chapter, the results of this Thesis are reviewed and the implications of the work for hydrocephalus research is discussed. We make recommendations describing the experimental data that would be useful in verifying the conjectures made in this Thesis, and outline some future directions that would continue and extend the ideas presented in this Thesis.

8.1 Chapter Summaries and Conclusions

We begin with brief summaries of the results and conclusions of each research Chapter of this Thesis, and the implications of these results.

Pressure Volume Model Conclusions

In Chapter 3, a pressure volume model was used to analyze the CSF dynamics of the cranium. Using experimentally determined values of compliance, pressure volume index, resistance to CSF absorption, and absorption site pressure, the model was unable to reproduce observed CSF flow dynamics. The predicted pulsations were much smaller than the observed normal CSF pulsations of 5 mm Hg peak-to-peak. Prescribed criteria guaranteed pulsations of 5 mm Hg, an average CSF pressure of 13.5 mm Hg, and synchrony between the CSF and arterial forcing pulsations, in order to determine the compliance, resistance to CSF absorption, and absorption site pressure model parameters. A compliance or pressure volume index five orders of magnitude smaller than experimentally determined values was required to predict CSF flow satisfying the criteria and to

match observed CSF dynamics. Assuming a constant compliance, it was demonstrated that the CSF and arterial pulsations are approximately synchronous when $2\omega C_0 R_a \ll 1$, and that large disruptions in the balance of the compliance, the resistance, and the heart rate are required to disturb this synchrony. The main conclusion of the pressure volume analysis was that these simple temporal models, pressure volume models and the analogous circuit models, are incapable of accurately predicting the complex CSF dynamics of the cranium. Furthermore, in hydrocephalus, where increased CSF pressure pulse amplitudes occur with any combination of an increased or decreased mean ICP and an increased or decreased PVI or cranial compliance, the dynamics are complex and cannot be described by these ordinary differential equation models.

In light of the analysis presented in Chapter 3, it is hoped that future investigations of CSF dynamics and hydrocephalus will focus on spatio-temporal models, which are better suited to capture the dynamics of CSF and brain tissue within the cranium.

Poroelastic Model Conclusions

In Chapter 4, the pulsation-damage hypothesis was analyzed using a poroelastic model to predict the interactions between the fluid and solid phases of brain tissue in response to CSF pulsations. The model was solved analytically for the parenchyma displacement, fluid filtration, and pore pressure, and using parameter sensitivity analyses, significant parameters of the model were identified. The Young's modulus and the pressure difference between the ventricle and SAS pulsations were found to be significant factors that influenced parenchyma displacement and thus ventricular expansion. In order to determine the capability of trans-parenchymal fluid flow to damage the tissue at the cellular level, a single pore flow model was developed. The shear stress induced on the wall of a pore by fluid flow moving at the filtration velocity was found to be negligible when compared to the shear stress required to detach a cell from a substrate or to break a single adhesion bond. This analysis indicates that the fluid flow through brain tissue is not a significant contributor to tissue damage observed in hydrocephalus. Only the internal tissue stresses remain as a possible mechanism for tissue damage, and thus a possible mechanism contributing to ventricular expansion, in the pulsation-damage hypothesis.

The poroelastic model presented in this Thesis does not allow for parenchymal fluid absorption. Incorporating absorption by the capillaries of the tissue would increase the peak fluid filtration velocity, and thus increase the shear stress induced by the flow on the pore walls. Furthermore, the effects of oscillatory shear flows on cells attached to substrates, especially substrates coated with ligands found in abundance in the brain ECM (not collagen or fibronectin) have yet to be experimentally determined. If the ability of cells to adhere to brain ECM is significantly weaker than their ability to adhere to collagen, then the shear required to detach them, or to break an adhesion bond, will be less than the shear forces estimated in Chapter 4. In this case, the fluid filtration

near the ventricles may be a more significant contributor to the tissue damage; however, it is more likely that fluid filtration plays a secondary role in the initiation of tissue damage, especially if the structural integrity of the tissue has already been compromised. If the tissue is in a diseased state, or if preliminary structural damage is already present, then fluid filtration may facilitate further damage to the tissue.

The Young's modulus and the difference in CSF pulse amplitude between the ventricles and the SAS were shown to affect the amount of parenchymal displacement significantly. A reduced Young's modulus and larger amplitude differences were hypothesized to cause larger compressive and expansive forces in the tissue. The cells of living biological tissues are able to sense mechanical and chemical stimuli and to react in response to these stimuli. Living tissues, therefore, have the ability to reorganize the microstructure of the tissue which may have profound effects on the tissue's macroscopic mechanical properties. With regards to hydrocephalus, the expanded ventricles compress the brain tissue which may, over time, cause the cells to reorganize the microstructure in order to reduce the internal state of stress of the tissue. The prospect that this reorganization may alter the macroscopic mechanical properties of the tissue is a new and exciting aspect that should be incorporated into mathematical models of hydrocephalus, and represents a novel direction for future exploration.

Fractional Zener Model Conclusions

In Chapter 5, the fractional Zener viscoelastic model was used to analyze both the infant and adult cases of hydrocephalus with regards to the effect of pulsatile CSF on ventriculomegaly, more specifically, with regards to the pulsation-damage hypothesis. In infant hydrocephalus, zero stress was enforced at the cortical surface to represent the unfused sutures of the skull, whereas in adult hydrocephalus, zero displacement was enforced at the cortical surface to represent the rigid skull. Peak-to-peak ventricle wall displacements of 6 mm were predicted in the infant brain, and of 100 nm in the adult brain, for typical pulse amplitudes found in hydrocephalic brains [35] (pressure pulsations of 667 Pa, or 10 mm Hg peak-to-peak). The material stresses for both cases ranged from 670 Pa to 800 Pa which are smaller than the damage threshold of 2710 Pa determined for white matter by Franceschini *et al.* [40]. Thus, CSF pulsations, even at the magnitude observed in hydrocephalic patients, appear to give rise to internal tissue stresses that are too small to be responsible for the tissue damage observed in hydrocephalus.

In Chapter 5, two conjectures were advanced: first, that the order of the fractional derivative is a parameter capable of capturing the effects of microstructural changes and growth processes in brain tissue, and second, that the bulk modulus may decrease with advancing age, making the aged brain more easily compressed by hydrostatic pressures, and thus more susceptible to developing hydrocephalus. These two aspects lead to promising new directions worthy of future investigations.

Brain Tissue Aging and the Fractional Zener Model Conclusions

In Chapter 6, using age-dependent shear complex modulus data, the parameter values for several linear viscoelastic models for infant and adult cerebra were determined. Then, the tissue displacements predicted by the fractional Zener model were recomputed both for the infant and adult brains, under conditions simulating hydrocephalus. The infant displacements where found to be unphysical when the new parameter values were used. A new boundary condition was proposed to replace the weak condition of zero-stress at the outer boundary, as used in the infant boundary value problem. The new condition linearly interpolates between the original infant and adult boundary conditions. Initially, it was estimated that the infant skull should provide about 40% to 50% of the resistive force that the adult skull provides, but the model required 86% in order to obtain physically reasonable displacements. After performing parameter sensitivity analyses, the steady-state elastic modulus was identified as a parameter of interest in models of hydrocephalus. The stresses predicted by the fractional Zener model were relatively unaffected by the new parameter values, and the magnitude of the new boundary value problem stresses were still in the range of 670 Pa to 800 Pa. Thus, the material stresses induced by the CSF pulsations remained around 30% of the tissue damage threshold discussed in Chapter 5. Therefore, even with the age-appropriate model parameters, the CSF pulsations are still incapable of being the primary cause of the tissue damage observed in hydrocephalus.

From the age-dependent data presented by Thibault and Margulies [124] and by Sack *et al.* [106], and from the analysis presented in Chapter 6, it was possible to show that the steady-state elastic modulus increases from a minimum value at infancy to a maximum value at early adulthood, which led to our conjecture that it then declines slowly with advancing age. This age-dependence of the elastic modulus may partially explain why the pediatric and geriatric populations seem to be those most susceptible to hydrocephalus.

Since both the fluid and the solid phases of brain tissue have been shown in this Thesis to cause tissue stresses incapable of damaging healthy tissue, no mechanism remains to explain the tissue damage and ventricular expansion of hydrocephalus, according to the pulsation-damage hypothesis. Simplifications have been made in the analyses of this Thesis; however, we believe that they do not significantly affect the results. Therefore, we conclude that CSF pulsations are not a primary contributor to the forces that damage seemingly healthy tissue in hydrocephalus, and thus the pulsation-damage hypothesis, as described in this Thesis, should be revised.

Fractional Hyper-Viscoelastic Model Conclusions

In Chapter 7, with age-appropriate mechanical parameter values for infant brain tissue, small magnitude long-term pressure gradients were shown to be sufficient to cause the ventricular expansion observed in hydrocephalus. A fractional hyper-viscoelastic model for infant brain tissue based on a Kelvin-Voigt solid

was presented. Using the assumption of small strains, both the oscillatory response and the step response of the material were analyzed. Next, a numerical technique based on the incremental law of soft tissues [42] was presented. This iteratively solved the small strain solution to approximate a finite deformation. The technique is capable of predicting large deformations without the necessity for large material stresses; this is consistent with the belief that hydrocephalus may develop due to the accumulation of small strains. The technique also provides a tool by which long-term tissue deformations can be estimated from the magnitude of steady-state pressure gradients. The predicted deformations were shown to be consistent with the predictions of the finite-strain solution found by solving the model with first order derivatives numerically. Assuming that an Evans Ratio of 0.4 is an indicator of hydrocephalus, it was possible to show that transmantle pressure gradients of 1 mm Hg are sufficient to cause hydrocephalus in an infant brain, where the steady-state shear modulus is reduced compared with that of a healthy young adult. Thus, pressure gradients too small to be detected by experimental pressure sensors may exist in hydrocephalic brains, and may contribute to the expansion of the ventricles.

In Chapter 7, it was shown that pediatric communicating hydrocephalus may result from small pressure gradients, that in other circumstances, such as in a mature adult brain, may not have much effect. This result is significant as it indicates that ventricular expansion can occur under small magnitudes of the pressure gradient that are undetectable experimentally, since the magnitudes lie below the sensitivity threshold of the transducers [67]. Furthermore, the iterative numerical technique provides a way of predicting ventricular expansion without the necessity for large stresses to occur in the tissue. It also provides a tool that may prove useful to both clinicians and experimentalists in their quest for both a more fundamental understanding of, and more effective treatments for, hydrocephalus; to the best of our knowledge, this is the first time that results of this nature have been established.

8.2 Overall Conclusions

In this Thesis, we have shown, by analyzing both the fluid and solid phases of brain tissue and their interactions, that CSF pulsations cannot be the primary cause of the tissue damage and ventricular expansion observed in hydrocephalus. Thus, the pulsation-damage hypothesis needs to be revised. We have also shown that in the infant brain, where the steady-state elastic modulus, and thus the steady-state shear modulus, are smaller than the corresponding adult brain tissue values, a pressure gradient on the order of 1 mm Hg is sufficient to cause ventricular expansion, and thus lead to hydrocephalus.

By hypothesizing that the steady-state elastic modulus of infant and elderly brain tissues may be reduced, we are lead to a potential explanation for the prevalence of hydrocephalus among these populations. Furthermore, the action of various proteins in brain tissue, as for example by the injection of antibodies

to β_1-integrins or by hemorrhages that result in a blood leakage into the extracellular environment, may initiate microstructural changes that alter the macroscopic mechanical properties of the tissue. During the brain growth spurt, the blood brain barrier is relaxed to allow nutrients, proteins, and other molecules vital to healthy brain growth and development, to enter the brain. It is plausible that, in some infants, this relaxed barrier allows various proteins/antibodies to enter the brain that trigger the damaging microstructural changes which lead to hydrocephalus. Furthermore, it may be possible that the blood brain barrier of elderly adults is compromised, although, to our knowledge, no experimental evidence to support this claim exists. These potential microstructural changes lead to several questions that will be addressed in the next Section.

The iterative numerical technique, used in Chapter 7, predicted ventricular expansion without the accumulation of large stresses or strains in the material. This is consistent with the belief that hydrocephalus develops slowly over time due to the accumulation of small strains. When small pressure gradients accumulate over long times, the living tissue also deforms over long times, with small strains and small internal stresses. The tissue may then, in response to the mechanical stimuli of these small structural stresses, reorganize its cell-extracellular matrix structure to reduce these stresses. With the build-up of another increment in pressure, the process may start over again, eventually producing a large-strain-free finite deformation, a new configuration of the cell-ECM structure, and altered mechanical properties of the tissue.

A 1 mm Hg transmantle pressure gradient was shown to be sufficient to cause hydrocephalus in infant brains where the long-time shear modulus is estimated to be about 200 Pa. In contrast, both the long-time shear modulus and brain geometry are larger in adult brains, suggesting that this pressure gradient may be insufficient to cause hydrocephalus on its own. It is more likely, therefore, that hydrocephalus develops due to the combined effects of a cascade of events. Each event on its own may be insufficient to cause ventricular dilation to the extent that it is seen in hydrocephalic brains, but together, their cumulative effects may be quite severe.

One possible scenario could be as follows. A disease, microscopic, or chemical change may initially degrade the macroscopic mechanical properties of the brain tissue, as well as disrupt the tissue's homeostatic state by altering osmotic pressures. This may create a small intramantle pressure gradient which may further perturb the Starling forces increasing fluid absorption by the capillaries of the tissue. Increased parenchymal absorption would increase the magnitude of the intramantle pressure gradient causing tissue compression, and potentially decreasing the compliance of the cranium. This decreased compliance may cause the CSF pulsations to increase in amplitude and to develop a slight imbalance between the ventricles and SAS. Additionally, a transmantle pressure gradient may develop, further compressing the tissue.

In response to the compression caused by the oscillatory, intramantle, and transmantle pressure gradients, the hyaluronic acid complexes of the extracellular matrix may release the water molecules they bind to allow tissue com-

pression to occur without significantly affecting the health of the neural cells. Since the periventricular regions compress the most, this released water from the ECM may contribute to edema formation. The continual stretching and compression of the tissue, combined with the presence of edema and the initial microstructural/chemical/disease-induced changes may all contribute to damage the ependyma and periventricular tissues. With tissue damage, the permeability of the tissue would increase, speeding up the fluid filtration through the periventricular regions and potentially contributing further to the edema and tissue damage. The resulting ventricular expansion, combined with the tissue damage and presence of edema, complete the description of hydrocephalic brains, thus suggesting that hydrocephalus may be the cumulative result of an unfortunate cascade of events.

To summarize, we attempt to categorize the results of this Thesis by trying to answer a few of the questions posed by Bergsneider, Egnor, and Johnston, *et al.* in their paper, *What we don't (but should) know about Hydrocephalus* [10].

1. "Why do the ventricles dilate in communicating hydrocephalus?"

   We propose that the absorption-degradation hypothesis adequately answers this question. The sequence of events eventually leading to hydrocephalus is initiated by microstructural changes that increase fluid absorption by the parenchyma and degrade the tissue's elastic properties. Intramantle and transmantle pressure gradients, small enough to be considered noise in experimental measurements, form, and over long times, provide the mechanism for ventricular expansion.

2. "What causes normal pressure hydrocephalus?"

   The above explanation does not specifically require increased intracranial pressure and thus also explains normal pressure hydrocephalus.

3. "How is the brain of a child with hydrocephalus different from that of a young or elderly adult?"

   In Chapter 6, we discussed how the mechanical properties of infant cerebrum are different from those of young adult cerebrum, which may also be different from those of elderly adult cerebrum. It was demonstrated that the steady-state elastic modulus of infant cerebrum is reduced compared to that of adult cerebrum, and we conjectured that the steady-state elastic modulus of elderly adult cerebrum is reduced. This reduction in the mechanical properties of brain cerebrum provides a possible explanation for the increased susceptibility of these populations to developing hydrocephalus. Furthermore, the compromised state of the blood brain barrier in infants would increase the likelihood of undesirable proteins/molecules entering the brain tissue and initiating damaging microstructural changes leading to hydrocephalus.

8.3 Future Directions

A central theme of this Thesis is the suggestion that ventricular expansion may be the result of microstructural changes in the tissue. The introduction of fractional derivatives into the constitutive equations for brain tissue mechanics, is a first attempt to link microstructural changes to the macroscopic description of the material. Thus, we foresee a fruitful and challenging future for mathematical modelling in hydrocephalus in several areas: incorporating changes in the cell and extracellular matrix, in the biochemical reactions that occur in the cell and ECM, to the fibrous nature of the ECM, in the behaviour or structure of the cell, in the osmotic balance of the tissue, in the permeability of the blood brain barrier, and a major challenge will be to link multi-scale, multi-level effects to a macroscopic description of brain tissue. Linking these multiple scales may well lead to the discovery of possible biological changes that may be capable of inducing hydrocephalus.

8.3.1 Recommendations to Experimentalists

While completing the research presented in this Thesis, it quickly became apparent that there is a dearth of experimental data/information relevant for the purposes of mathematical modelling. Below are listed various recommendations and suggestions to experimentalists that will hopefully help to settle various questions and, in general, further our collective understanding of hydrocephalus (as well as brain tissue growth, development, and aging).

1. *Pressure Distribution*
   Many theories for hydrocephalus hinge on the existence of transmantle or intramantle pressure gradients. Recording the pressure at several positions throughout the parenchyma from the ventricles to the SAS would help to determine if such gradients exist, and if they do, their magnitudes.

2. *Oscillatory Shear Flows*
   In the poroelastic model, CSF was found to oscillate in and out of the periventricular tissue causing oscillatory shear stresses to act on the tissue. The effect of oscillatory shear flows on cells attached to substrates has yet to be investigated. Oscillatory shear flows may damage tissue more easily than steady flows due to the flow reversals. Therefore, it is important to determine the effect of oscillatory shear flows on cell adhesion in order to better estimate their potential to cause damage.

3. *Cell Adhesion Strength*
   Cell adhesion tests typically use collagen or fibronectin coated substrates; unfortunately, these molecules are not predominant in brain ECM. Thus, cell adhesion strength to brain ECM may differ significantly from the estimates based on these studies. Therefore, in order to determine the adhesion strength of cells to brain ECM, shear flow experiments should

be performed with substrates coated with ligands found in abundance in brain ECM.

4. *Age-Dependent Bulk Modulus*
   In this Thesis, the bulk modulus of an aged brain is conjectured to be reduced compared to that of a healthy mature brain. Experiments should be conducted to determine if the bulk modulus of brain tissue is age-dependent. It may also prove interesting to determine how the macroscopic bulk modulus of the tissue relates to the bulk modulus of the individual cells, thus linking the microscopic and macroscopic levels of the tissue.

5. *Age-Dependent Mechanical Properties In Vivo*
   The complex modulus data for infant porcine cerebrum presented by Thibault and Margulies [124] may not accurately describe the tissue's behaviour inside a closed cranium, since the tissues were excised and tested in a mechanical apparatus surrounded by air. Infant brain tissue is still developing its cellular structure and thus its behaviour may be more sensitive to the environment in which it is tested than adult brain tissue, and the mechanical behaviour may be altered by removal from the cerebrospinal fluid bath in the cranial vault. The MRE experimental method used by Sack *et al.* [106] resolves these problems. Therefore, animal MRE experiments should be conducted with a wide range in subject age (from infancy to old age) to test the hypothesized age-dependence of the steady-state elastic modulus.

6. *Accurate MRE Data Fitting*
   The magnetic resonance elastography complex modulus data [106] approximately agreed with the adult porcine data [124], but the slopes of the storage and loss moduli curves differed. Similar differences may exist between the infant porcine data and potential MRE measurements of infant subjects. This may imply a reduction in the initial elastic modulus and an increase in the relaxation time; however, the number of data points used in the MRE experiments (4) is too small to permit a reliable fit to our models. Thus, more frequency values should be used in future MRE experiments.

7. *Age-Dependent Creep and Relaxation*
   The complex modulus does not fully characterize all behaviours of a viscoelastic material. As discussed in Chapter 6, model parameters that accurately predict the oscillatory response of brain tissue do not accurately predict the relaxation behaviour of brain tissue. Thus, it is important to perform creep and relaxation tests, as well as vibration tests, to fully characterize the behaviour, and to allow for the determination of age-dependent model parameters that describe all aspects of the viscoelastic behaviour of soft biological tissues.

8.3.2 Future Work

Lastly, we consider some possible future projects that extend the concepts of, or investigate the conjectures made in, this Thesis.

1. *Parenchymal Fluid Absorption*
   One possible extension of the poroelastic model described in Chapter 4, is to incorporate parenchymal fluid absorption into the governing equations. Fluid absorption by the capillaries of brain tissue should increase the peak fluid filtration velocity, as well as slightly alter the interactions between the fluid and solid phases of the brain, due to the CSF pulsations. If fluid flow near the ventricles is markedly increased due to the additional withdrawal of fluid that absorption would necessitate, then the shear stress induced on the cells of the tissue will also be increased. Once the new filtration velocities are determined, the shear flow induced stress can be calculated. This stress can be compared to the damage thresholds, such as the shear required to detach a cell from a substrate or the shear required to break a single adhesion bond, in order to determine if tissue fluid filtration is a potential factor in tissue damage when parenchymal fluid absorption is taken into consideration.

2. *Effects of Integrin Antibodies*
   Another possible extension of the poroelastic model described in Chapter 4 is to macroscopically incorporate the presumed effect of an injection of β_1-integrin antibodies [86]. Using the assumption that the antibodies reduce the Young's modulus of the tissue and locally increase the permeability, preliminary investigations of the antibodies' role in the development of hydrocephalus can be made. This work would be based on the investigations made during the OCCAM-Fields-MITACS problem solving workshop [9].

3. *ECM Cushioning Mechanism*
   I propose to investigate the cushioning mechanism of brain ECM provided by the unique composition of the matrix, or more specifically, by the presence of hyaluronic acid. This acid molecule is known to be capable of binding water molecules to provide a cushioning effect and to protect the tissue from compression-induced damage. I would like to develop a poroelastic model that allows for the partial transition of the solid phase to the fluid phase, where the transition is triggered by compression. Such a model could provide insight into the development of edema in hydrocephalus.

4. *Fractional Order Derivatives*
   In Chapter 5, we hypothesized that the value of α, the fractional order of the derivative, captures microstructural changes in the tissue; but, in Chapter 6, curve fitting to age-dependent shear complex modulus data showed that the value of α is approximately 0.8 for both infant and adult cerebra. It is possible, however, that curve fitting with creep and relaxation data for infant and adult brain tissue would result in different values

of α. Thus, in the future, when this experimental data becomes available, it appears feasible to perform a curve fitting analysis to see if the order of the fractional derivative is capable of capturing the compositional and microstructural changes that occur during the growth and development or degeneration phases of the human brain tissue lifespan.

5. *Fractional Hyperelastic Constitutive Equation*
   To improve upon the simple fractional hyper-viscoelastic model based on the Kelvin-Voigt solid used in Chapter 7, I would like to develop a more realistic constitutive equation for brain tissue. In collaboration with C. Drapaca PhD (The Pennsylvania State University), I would like to explore the use of fractional derivatives to develop a new strain energy density function. The addition of fractional derivatives to this function will introduce a history dependence that may improve the model's ability to link the microscopic and macroscopic scales of tissues.

6. *Microstructural Changes*
   To investigate the effects of a living tissue's ability to reduce its internal state of stress, I would like to develop a constitutive equation that allows for microstructural changes due to the reorganization of the cell-ECM binding cites. A framework for incorporating microstructural changes into constitutive equations of materials has already been developed by Rajagopal and Wineman [99], and this work would provide a starting point for my tissue model. Building a model to account for microstructural changes of the tissue will allow for further analytical investigation of the work of Johnston and colleagues [86] in the development of hydrocephalus.

7. *Microstructure Derived Constitutive Equation*
   Following the work of Bagley [5] and others in the field of polymer mechanics, another direction of interest would be to derive a constitutive equation for brain tissue directly from the microstructure. Fractional constitutive equations have been derived from the microstructure of polymers, and the similarities between the microstructure of polymers and brain tissue suggest that an analogous derivation could be carried out for brain tissue.

The goal of mathematical modelling in hydrocephalus is to help further our understanding of the causes and formation of this severe clinical condition. Modelling may propose hypotheses or questions that can help to direct future experimental investigations and it can help to explore existing or new etiological theories. In these regards, the models presented in this Thesis have been quite successful.

Appendix A

Details of the Poroelastic Model

A.1 Analytic Solution

This section describes the process of solving the coupled system of PDEs given by (4.11) and (4.12), and also given below for convenience,

$$\frac{\partial^2 u}{\partial t^2} + f_r \frac{\partial u}{\partial t} = f_r \frac{1}{r} c_0(t) + {c_d}^2 \left(\frac{\partial^2 u}{\partial r^2} + \frac{1}{r}\frac{\partial u}{\partial r} - \frac{1}{r^2} u \right) \tag{A.1}$$

$$\frac{\partial p_d}{\partial r} = \frac{\mu}{k} \left(\frac{\partial u}{\partial t} - \frac{1}{r} c_0(t) \right). \tag{A.2}$$

Recall that $f_r = \frac{\mu}{\rho k}$ is the relaxation frequency and $c_d = \sqrt{\frac{\lambda+2G}{\rho}}$ is the propagation speed of the dilatational waves. The first step to solving this system is to nondimensionalize the equations.

A.1.1 Nondimensionalization

We begin by defining the characteristic scales and nondimensional variables listed in Table A.1. Using these definitions, the displacement PDE (A.1) becomes

$$\hat{u}_{\hat{t}\hat{t}} + \hat{u}_{\hat{t}} = \frac{1}{\hat{r}} \hat{c}_0(\hat{t}) + \left(\hat{u}_{\hat{r}\hat{r}} + \frac{1}{\hat{r}} \hat{u}_{\hat{r}} - \frac{1}{\hat{r}^2} \hat{u} \right), \tag{A.3}$$

and the pressure PDE (A.2) becomes

$$\hat{p}_{\hat{r}} = \frac{1}{\hat{k}} \left(\hat{u}_{\hat{t}} - \frac{1}{\hat{r}} \hat{c}_0(\hat{t}) \right). \tag{A.4}$$

Table A.1: Characteristic scales and nondimensional variables and parameters for the poroelastic model equations (4.11) and (4.12).

$T_c = \frac{1}{f_r}$	characteristic time
$L_c = \frac{c_d}{f_r}$	characteristic length
$M_c = \frac{\mu c_d}{f_r^2}$	characteristic mass
$\hat{t} = f_r t$	nondimensional time
$\hat{r} = \frac{f_r r}{c_d}$	nondimensional length
$\hat{u}(\hat{r}, \hat{t}) = \frac{f_r}{c_d} u(r,t)$	nondimensional displacement
$\hat{p}(\hat{r}, \hat{t}) = \frac{1}{\mu f_r} p_d(r,t)$	nondimensional dynamic pressure
$\hat{c}_0(\hat{t}) = \frac{f_r}{c_d^2} c_0(t)$	nondimensional arbitrary integration function
$\hat{r}_V = \frac{f_r}{c_d} r_V$	nondimensional ventricle boundary
$\hat{r}_{SAS} = \frac{f_r}{c_d} r_{SAS}$	nondimensional SAS boundary
$\hat{k} = \frac{k f_r^2}{c_d^2}$	nondimensional permeability
$\hat{\omega} = \frac{\omega}{f_r}$	nondimensional angular frequency

A.1.2 Solving for Displacement

Assuming $\hat{u}(\hat{r}, \hat{t}) = \mathrm{Re}\left(\hat{U}(\hat{r})\mathrm{e}^{i\hat{\omega}\hat{t}}\right)$ and $\hat{c}_0(\hat{t}) = \mathrm{Re}\left(\hat{C}_0\mathrm{e}^{i\hat{\omega}\hat{t}}\right)$ and substituting these forms into (A.3) gives

$$\left((i\hat{\omega})^2\hat{U} + i\hat{\omega}\hat{U}\right)\mathrm{e}^{i\hat{\omega}\hat{t}} = \frac{1}{\hat{r}}\hat{C}_0\mathrm{e}^{i\hat{\omega}\hat{t}} + \left(\hat{U}'' + \frac{1}{\hat{r}}\hat{U}' - \frac{1}{\hat{r}^2}\hat{U}\right)\mathrm{e}^{i\hat{\omega}\hat{t}},$$

or, after simplifying

$$\hat{r}^2\hat{U}'' + \hat{r}\hat{U}' + \left((\hat{\omega}^2 - i\hat{\omega})\hat{r}^2 - 1\right)\hat{U} = -\hat{C}_0\hat{r}.$$

Letting $\alpha = \sqrt{\hat{\omega}^2 - i\hat{\omega}}$, $\xi(\hat{r}) = \alpha\hat{r}$, $V(\xi) = \hat{U}(\hat{r})$ and $A = \frac{\hat{C}_0}{\alpha}$ rescales the above differential equation into

$$\xi^2 V'' + \xi V' + (\xi^2 - 1)V = -A\xi, \tag{A.5}$$

which is a nonhomogeneous Bessel DE of order one. The homogeneous solution is thus given by

$$V_h(\xi) = C_1 J_1(\xi) + C_2 Y_1(\xi), \tag{A.6}$$

where J_1 and Y_1 are the Bessel functions of order 1.

Finding the particular solution requires the method of reduction of order. Since $J_1(\xi)$ is a solution to the homogeneous DE, a guess of the particular solution is $V_p(\xi) = J_1(\xi)w(\xi)$. Substituting this form into (A.5) gives

$$\xi^2(J_1''w + 2J_1'w' + J_1w'') + \xi(J_1'w + J_1w') + (\xi^2 - 1)J_1w = -A\xi.$$

Rewriting the equation as

$$w(\xi^2 J_1'' + \xi J_1' + (\xi^2 - 1)J_1) + w'(2\xi^2 J_1' + \xi J_1) + w''(\xi^2 J_1) = -A\xi$$

shows that the first term vanishes since J_1 satisfies the homogeneous Bessel DE of order one. This leaves the following second order DE for w,

$$w'' + \frac{2\xi^2 J_1' + \xi J_1}{\xi^2 J_1} w' = -\frac{A}{\xi J_1}. \tag{A.7}$$

Rewriting this as a first order linear DE for w', we can identify the integrating factor as

$$I(\xi) = \exp\left(\int 2\frac{J_1'}{J_1} + \frac{1}{\xi}\mathrm{d}\xi\right) = \exp\left(\ln J_1^2 + \ln|\xi|\right) = \xi J_1^2. \tag{A.8}$$

Multiplying (A.7) by the integrating factor and collapsing the left hand side gives

$$\frac{\mathrm{d}}{\mathrm{d}\xi}\left(w'\xi J_1^2\right) = -AJ_1, \tag{A.9}$$

and integrating with respect to ξ gives

$$w'\xi J_1^2 = -A\int J_1 \mathrm{d}\xi = AJ_0 + C_3,$$

or

$$w' = \frac{AJ_0}{\xi J_1^2} + \frac{C_3}{\xi J_1^2}.$$

Integrating once again gives

$$w = A\int \frac{J_0}{\xi J_1^2}\mathrm{d}\xi + C_3\int \frac{1}{\xi J_1^2}\mathrm{d}\xi = -\frac{A}{\xi J_1} + \frac{\pi}{2}C_3\frac{Y_1}{J_1} + C_4.$$

The above integrations and simplifications have used the following properties of Bessel functions:

$$\frac{\mathrm{d}}{\mathrm{d}\xi}\left(\frac{-1}{\xi J_1}\right) = \frac{1}{(\xi J_1)^2}\left(J_1 + \xi J_1'\right) = \frac{J_1 + \xi(J_0 - \frac{1}{\xi}J_1)}{(\xi J_1)^2} = \frac{J_0}{\xi J_1^2}$$

and

$$\frac{\mathrm{d}}{\mathrm{d}\xi}\left(\frac{\pi}{2}\frac{Y_1}{J_1}\right) = \frac{\pi}{2}\frac{Y_1' J_1 - Y_1 J_1'}{J_1^2} = \frac{\pi}{2}\frac{\mathcal{W}(J_1, Y_1)}{J_1^2} = \frac{\pi}{2}\frac{2}{\pi\xi}\frac{1}{J_1^2} = \frac{1}{\xi J_1^2},$$

where $\mathcal{W}(f, g)$ is the Wronskian and $\mathcal{W}(J_n(z), Y_n(z)) = \frac{2}{\pi z}$ [130, pg. 76].

The particular solution is therefore,

$$\begin{aligned} V_p = J_1 w &= J_1 \left(\frac{-A}{\xi J_1} + C_3 \frac{\pi}{2} \frac{Y_1}{J_1} + C_4 \right) \\ &= -\frac{A}{\xi} + C_3 \frac{\pi}{2} Y_1 + C_4 J_1. \end{aligned} \tag{A.10}$$

Since $J_1(\xi)$ and $Y_1(\xi)$ are the independent functions that make up the homogeneous solution, they don't contribute to the particular solution and the constants C_3 and C_4 can be set to zero. The solution to (A.5) is therefore given by

$$V(\xi) = V_h(\xi) + V_p(\xi) = C_1 J_1(\xi) + C_2 Y_1(\xi) - \frac{A}{\xi}, \tag{A.11}$$

and the nondimensional displacement is thus

$$\hat{u}(\hat{r}, \hat{t}) = \mathrm{Re}\left(\left(C_1 J_1(\alpha \hat{r}) + C_2 Y_1(\alpha \hat{r}) - \frac{\hat{C}_0}{\alpha^2 \hat{r}} \right) \mathrm{e}^{i\hat{\omega}\hat{t}} \right). \tag{A.12}$$

A.1.3 Solving for Pressure

Assuming $\hat{p}(\hat{r}, \hat{t}) = \mathrm{Re}\left(\hat{P}(\hat{r})\mathrm{e}^{i\hat{\omega}\hat{t}}\right)$ and substituting into the PDE for pressure (A.4) gives

$$\hat{P}'(\hat{r})\mathrm{e}^{i\hat{\omega}\hat{t}} = \frac{1}{\hat{k}} \left(i\hat{\omega}\hat{U}(\hat{r}) - \frac{1}{\hat{r}}\hat{C}_0 \right) \mathrm{e}^{i\hat{\omega}\hat{t}}.$$

Using $\hat{U}(\hat{r}) = V(\xi)$, substituting (A.11), and simplifying gives

$$\hat{P}'(\hat{r}) = \frac{i\hat{\omega}}{\hat{k}} \left(C_1 J_1(\alpha \hat{r}) + C_2 Y_1(\alpha \hat{r}) \right) - \frac{\omega^2 \hat{C}_0}{\hat{k}\alpha^2 \hat{r}},$$

since $\alpha^2 = \omega^2 - i\omega$. Integrating with respect to $\hat{r}$ gives the nondimensional pressure amplitude as

$$\hat{P}(\hat{r}) = \frac{-i\hat{\omega}}{\hat{k}\alpha} \left(C_1 J_0(\alpha \hat{r}) + C_2 Y_0(\alpha \hat{r}) \right) - \frac{\omega^2 \hat{C}_0}{\hat{k}\alpha^2} \ln(\hat{r}) + C_3. \tag{A.13}$$

The nondimensional pressure function is thus given by

$$\hat{p}(\hat{r}, \hat{t}) = \mathrm{Re}\left(\left(\frac{-i\hat{\omega}}{\hat{k}\alpha} \left(C_1 J_0(\alpha \hat{r}) + C_2 Y_0(\alpha \hat{r}) \right) - \frac{\omega^2 \hat{C}_0}{\hat{k}\alpha^2} \ln(\hat{r}) + C_3 \right) \mathrm{e}^{i\hat{\omega}\hat{t}} \right). \tag{A.14}$$

A.1.4 Applying the Boundary Conditions

Nondimensionalizing the boundary conditions for the dynamic pressure (4.13) requires that the nondimensional pressure amplitude function, $\hat{P}(\hat{r})$, satisfies

$$\begin{cases} \hat{P}(\hat{r}_V) = \hat{p}_V \\ \hat{P}(\hat{r}_{SAS}) = \hat{p}_{SAS}, \end{cases}$$

where $\hat{p}_V = \frac{1}{\mu f_r} p_V$ and $\hat{p}_{SAS} = \frac{1}{\mu f_r} p_{SAS}$. Using the above expression for the nondimensional pressure amplitude (A.13) gives

$$\begin{cases} \frac{-i\hat{\omega}}{\hat{k}\alpha}\left(C_1 J_0(\alpha\hat{r}_V) + C_2 Y_0(\alpha\hat{r}_V)\right) - \frac{\hat{\omega}^2 \ln(\hat{r}_V)}{\hat{k}\alpha^2}\hat{C}_0 + C_3 = \hat{p}_V \\ \frac{-i\hat{\omega}}{\hat{k}\alpha}\left(C_1 J_0(\alpha\hat{r}_{SAS}) + C_2 Y_0(\alpha\hat{r}_{SAS})\right) - \frac{\hat{\omega}^2 \ln(\hat{r}_{SAS})}{\hat{k}\alpha^2}\hat{C}_0 + C_3 = \hat{p}_{SAS}. \end{cases} \tag{A.15}$$

Nondimensionalizing the displacement boundary conditions (4.14) requires that the nondimensional displacement amplitude function, $\hat{U}(\hat{r})$, satisfies

$$\begin{cases} \frac{\lambda+2G}{\lambda}\hat{U}'(\hat{r}_V) + \frac{1}{\hat{r}_V}\hat{U}(\hat{r}_V) = 0 \\ \frac{\lambda+2G}{\lambda}\hat{U}'(\hat{r}_{SAS}) + \frac{1}{\hat{r}_{SAS}}\hat{U}(\hat{r}_{SAS}) = 0. \end{cases}$$

Using $\hat{U}(\hat{r}) = V(\xi)$, and substituting the expression for the nondimensional displacement amplitude, (A.11), gives the boundary conditions as

$$\begin{cases} \frac{\lambda+2G}{\lambda}\left(\alpha C_1 J_1'(\alpha\hat{r}_V) + \alpha C_2 Y_1'(\alpha\hat{r}_V) + \frac{\hat{C}_0}{\alpha^2\hat{r}_V^2}\right) \\ \qquad + \frac{1}{\hat{r}_V}\left(C_1 J_1(\alpha\hat{r}_V) + C_2 Y_1(\alpha\hat{r}_V) - \frac{\hat{C}_0}{\alpha^2\hat{r}_V}\right) = 0 \\ \frac{\lambda+2G}{\lambda}\left(\alpha C_1 J_1'(\alpha\hat{r}_{SAS}) + \alpha C_2 Y_1'(\alpha\hat{r}_{SAS}) + \frac{\hat{C}_0}{\alpha^2\hat{r}_{SAS}^2}\right) \\ \qquad + \frac{1}{\hat{r}_{SAS}}\left(C_1 J_1(\alpha\hat{r}_{SAS}) + C_2 Y_1(\alpha\hat{r}_{SAS}) - \frac{\hat{C}_0}{\alpha^2\hat{r}_{SAS}}\right) = 0. \end{cases} \tag{A.16}$$

Since $J_1'(z) = J_0(z) - \frac{1}{z}J_1(z)$ and $Y_1'(z) = Y_0(z) - \frac{1}{z}Y_1(z)$, the above conditions simplify to

$$\begin{cases} \frac{1}{\alpha^2\hat{r}_V}\hat{C}_0 + \left(\frac{M\alpha\hat{r}_V}{2G}J_0^V - J_1^V\right)C_1 + \left(\frac{M\alpha\hat{r}_V}{2G}Y_0^V - Y_1^V\right)C_2 = 0 \\ \frac{1}{\alpha^2\hat{r}_{SAS}}\hat{C}_0 + \left(\frac{M\alpha\hat{r}_{SAS}}{2G}J_0^{SAS} - J_1^{SAS}\right)C_1 + \left(\frac{M\alpha\hat{r}_{SAS}}{2G}Y_0^{SAS} - Y_1^{SAS}\right)C_2 = 0, \end{cases} \tag{A.17}$$

where $M = \lambda + 2G$ and the notation $\mathcal{F}_n^B = \mathcal{F}_n(\alpha\hat{r}_B)$ with $n = 0$ or 1, $B = V$ or SAS, and $\mathcal{F} = J$ or Y, is used for convenience.

Boundary conditions (A.15) and (A.17) can be solved simultaneously by constructing the matrix equation $\mathbf{A}\vec{x} = \vec{b}$ where

$$\vec{x} = [\ \hat{C}_0 \quad C_1 \quad C_2 \quad C_3\ ]^T,$$
$$\vec{b} = [\ \hat{p}_V \quad \hat{p}_{SAS} \quad 0 \quad 0\ ]^T,$$

and the matrix $\mathbf{A}$ is defined as

$$\mathbf{A} = \begin{bmatrix} -\frac{\hat{\omega}^2\ln(\hat{r}_V)}{\hat{k}\alpha^2} & -\frac{i\hat{\omega}}{\hat{k}\alpha}J_0^V & -\frac{i\hat{\omega}}{\hat{k}\alpha}Y_0^V & 1 \\ -\frac{\hat{\omega}^2\ln(\hat{r}_{SAS})}{\hat{k}\alpha^2} & -\frac{i\hat{\omega}}{\hat{k}\alpha}J_0^{SAS} & -\frac{i\hat{\omega}}{\hat{k}\alpha}Y_0^{SAS} & 1 \\ \frac{1}{\alpha^2\hat{r}_V} & \frac{M\alpha\hat{r}_V}{2G}J_0^V - J_1^V & \frac{M\alpha\hat{r}_V}{2G}Y_0^V - Y_1^V & 0 \\ \frac{1}{\alpha^2\hat{r}_{SAS}} & \frac{M\alpha\hat{r}_{SAS}}{2G}J_0^{SAS} - J_1^{SAS} & \frac{M\alpha\hat{r}_{SAS}}{2G}Y_0^{SAS} - Y_1^{SAS} & 0 \end{bmatrix}. \tag{A.18}$$

A.2 Numerical Method

In order to numerically simulate the solutions to the poroelastic model, the asymptotic expasions of the Bessel functions for large arguments are used. They are [1]

$$J_0(z) = \sqrt{\frac{2}{\pi z}}\left(\cos\left(z-\frac{\pi}{4}\right)+\frac{1}{8z}\sin\left(z-\frac{\pi}{4}\right)-\frac{9}{128z^2}\cos\left(z-\frac{\pi}{4}\right)+\dots\right),$$
$$Y_0(z) = \sqrt{\frac{2}{\pi z}}\left(\sin\left(z-\frac{\pi}{4}\right)-\frac{1}{8z}\cos\left(z-\frac{\pi}{4}\right)-\frac{9}{128z^2}\sin\left(z-\frac{\pi}{4}\right)+\dots\right),$$
$$J_1(z) = \sqrt{\frac{2}{\pi z}}\left(\cos\left(z-\frac{3\pi}{4}\right)-\frac{3}{8z}\sin\left(z-\frac{3\pi}{4}\right)+\frac{15}{128z^2}\cos\left(z-\frac{3\pi}{4}\right)+\dots\right),$$
$$Y_1(z) = \sqrt{\frac{2}{\pi z}}\left(\sin\left(z-\frac{3\pi}{4}\right)+\frac{3}{8z}\cos\left(z-\frac{3\pi}{4}\right)+\frac{15}{128z^2}\sin\left(z-\frac{3\pi}{4}\right)+\dots\right).$$

The analytic solutions for displacement, pressure, filtration velocity, and the arbitrary constant, $c_0(t)$ are defined in terms of cross products of Bessel functions such as $J_0(x)Y_0(y) - Y_0(x)J_0(y)$ where x and y are complex. Expressions for these cross products can be found using the asymptotic expansions above and basic trigonometric identities. For example,

$$J_0(x)Y_0(y) - J_0(y)Y_0(x) = \frac{2}{\pi}\frac{1}{\sqrt{xy}}\left(\left(\frac{1}{8x}-\frac{1}{8y}+\dots\right)\cos(y-x) + \left(1-\frac{9}{28^2y^2}-\frac{9}{28^2x^2}+\frac{1}{8^2xy}+\dots\right)\sin(y-x)\right)$$

In the `MAPLE` code included below, the following variable names are defined as follows,

$$crossprodJ0Y0(x,y) = J_0(x)Y_0(y) - Y_0(x)J_0(y),$$
$$crossprodJ1Y0(x,y) = J_1(x)Y_0(y) - Y_1(x)J_0(y),$$
$$crossprodJ0Y1(x,y) = J_0(x)Y_1(y) - Y_0(x)J_1(y),$$
$$crossprodJ1Y1(x,y) = J_1(x)Y_1(y) - Y_1(x)J_1(y).$$

A.2.1 `Maple` Code

```
# Compute displacement, pressure, and filtration velocity
# from poroelastic model with pulsatile pressure BCs
restart:
digits := 20:

# Define constants
G := E / ( 2 * (1 + nu ) ):
lambda := E * nu / ( ( 1 + nu ) * ( 1 - 2 * nu ) ):
```

```
ri  := 3e−2: # 3 cm Ventricle wall boundary
ro := ri + 7e−2: # 10 cm SAS/cortical surface boundary
rm := ri + 0.5 * ( ro − ri ):  # 6.5 cm mid−point of parenchyma
convertmmHgPa := 133.32239: # to convert mmHg to Pa

# Define scalings, nondimensional variables and parameters
fr  := mu / ( rho * k ): # frequency time scale
cd := sqrt( ( lambda + 2 * G ) / rho ): # speed of dilatational waves
wH := omega / fr: # nondimensional frequency of oscillations
kH := k * fr^2 / cd^2: # nondimensional permeability
pHi := pii / ( mu * fr ):  # nondimensional pressure at ventricle wall
pHo := po / ( mu * fr ): # nondimensional pressure at cortical surface
rH := r −> fr * r / cd: # nondimensional spatial variable
rHi := rH( ri ):  # nondimensional ventricle wall boundary
rHo := rH( ro ): # nondimensional cortical surface boundary
alpha := evalf( sqrt( wH^2 − I * wH ) ): # a scaling
xi  := r −> alpha * rH( r ): # scaled nondimensional spatial variable
xii  := xi( ri  ):  # scaled nondimensional ventricle wall boundary
xio := xi( ro ):  # scaled nondimensional cortical surface  boundary

# Define cross products
crossprodJ0Y0 := ( x, y ) −> 2 * ( ( 1 / 8 / x − 1 / 8 / y ) * cos( y − x )
     + ( 1 − 9 / 128 / y^2 − 9 / 128 / x^2 + 1 / 64 / x / y )
     * sin( y − x ) ) / ( Pi * sqrt( x * y ) ):
crossprodJ1Y0:=( x, y )−> 2 * ( ( 3 / 8 / x + 1 / 8 / y ) * sin( y − x )
     + ( 1 − 9 / 128 / y^2 + 15 / 128 / x^2 − 3 / 64 / x / y )
     * cos( y − x ) ) / ( Pi * sqrt( x * y ) ):
crossprodJ0Y1 := ( x, y ) −> − crossprodJ1Y0( y, x ):
crossprodJ1Y1 := ( x, y ) −> 2 * ( ( 3 / 8 / y − 3 / 8 / x ) * cos( y − x )
     + ( 1 + 15 / 128 /y^2 + 15 / 128 / x^2 + 9 / 64 / x / y )
     * sin( y − x ) ) / ( Pi * sqrt( x * y ) ):

# Define the numerator of the constant c_0(t)
C0num := evalf( ( pHi − pHo ) * ( 4 * xii * G^2 * crossprodJ1Y0( xio, xii )
     + 4 * xio * G^2 * crossprodJ0Y1( xio, xii )
     + 2 * xio * lambda * G * crossprodJ0Y1( xio, xii )
     + 2 * xii * lambda * G * crossprodJ1Y0( xio, xii )
     + 4 * G^2 * crossprodJ1Y1( xii, xio )
     + xii * xio * lambda^2 * crossprodJ0Y0( xii, xio )
     + 4 * xii * xio * lambda * G * crossprodJ0Y0( xii, xio )
     + 4 * xii * xio * G^2 * crossprodJ0Y0( xii, xio ) )
     / ( xii * xio ) ):

C3num := evalf( wH * ( pHo * wH * ln( rHi ) * xii * xio * (
        4 * xii  * G^2 * crossprodJ0Y1( xii, xio )
     + 4 * xio * G^2 * crossprodJ1Y0( xii, xio )
```

```
    + 2 * xio * lambda * G * crossprodJ1Y0( xii, xio )
    + 2 * xii * lambda * G * crossprodJ0Y1( xii, xio )
    + 4 * G^2 * crossprodJ1Y1( xio, xii )
    + xii * xio * lambda^2 * crossprodJ0Y0( xio, xii )
    + 4 * xii * xio * lambda * G * crossprodJ0Y0( xio, xii )
    + 4 * xii * xio * G^2 * crossprodJ0Y0( xio, xii ) )
    + pHi * wH * ln( rHo ) * xii * xio * (
      4 * xii  * G^2 * crossprodJ1Y0( xio, xii )
    + 4 * xio * G^2 * crossprodJ0Y1( xio, xii )
    + 2 * xio * lambda * G * crossprodJ0Y1( xio, xii )
    + 2 * xii * lambda * G * crossprodJ1Y0( xio, xii )
    + 4 * G^2 * crossprodJ1Y1( xii, xio )
    + xii * xio * lambda^2 * crossprodJ0Y0( xii, xio )
    + 4 * xii * xio * lambda * G * crossprodJ0Y0( xii, xio )
    + 4 * xii * xio * G^2 * crossprodJ0Y0( xii, xio ) )
    + 2 * I * pHo * (
      2 * xio * G^2 * crossprodJ1Y0( xio, xii )
    + 2 * xio^2 * G^2 * crossprodJ0Y0( xii, xio )
    + 2 * xii * G^2 * crossprodJ0Y1( xii, xii )
    + xio^2 * lambda * G * crossprodJ0Y0( xii, xio ) )
    + 2 * I * pHi * (
      2 * xii  * G^2 * crossprodJ1Y0( xii, xio )
    + 2 * xii^2 * G^2 * crossprodJ0Y0( xio, xii )
    + 2 * xio * G^2 * crossprodJ0Y1( xio, xio )
    + xii^2 * lambda * G * crossprodJ0Y0( xio, xii ) ) )
    / ( kH * alpha^2 * xii^2 * xio^2 ) ):

# Define the determinant of the matrix A
detA := evalf( wH * ( wH * ln( rHi ) * xii * xio * (
      4 * xii  * G^2 * crossprodJ0Y1( xii, xio )
    + 4 * xio * G^2 * crossprodJ1Y0( xii, xio )
    + 2 * xio * lambda * G * crossprodJ1Y0( xii, xio )
    + 2 * xii * lambda * G * crossprodJ0Y1( xii, xio )
    + 4 * G^2 * crossprodJ1Y1( xio, xii )
    + xii * xio * lambda^2 * crossprodJ0Y0( xio, xii )
    + 4 * xii * xio * lambda * G * crossprodJ0Y0( xio, xii )
    + 4 * xii * xio * G^2 * crossprodJ0Y0( xio, xii ) )
    + wH * ln( rHo ) * xii * xio * (
      4 * xii  * G^2 * crossprodJ1Y0( xio, xii )
    + 4 * xio * G^2 * crossprodJ0Y1( xio, xii )
    + 2 * xio * lambda * G * crossprodJ0Y1( xio, xii )
    + 2 * xii * lambda * G * crossprodJ1Y0( xio, xii )
    + 4 * G^2 * crossprodJ1Y1( xii, xio )
    + xii * xio * lambda^2 * crossprodJ0Y0( xii, xio )
    + 4 * xii * xio * lambda * G * crossprodJ0Y0( xii, xio )
    + 4 * xii * xio * G^2 * crossprodJ0Y0( xii, xio ) )
```

```
      + 2 * I * G * (
         2 * G * xi^2 * crossprodJ0Y0( xio, xii  )
      + 2 * G * xio^2 * crossprodJ0Y0( xii, xio )
      + 2 * G * xii * crossprodJ1Y0( xii, xio  )
      + 2 * G * xio * crossprodJ1Y0( xio, xii )
      + 2 * G * xii * crossprodJ0Y1( xii, xii  )
      + 2 * G * xio * crossprodJ0Y1( xio, xio )
      + lambda * xi^2 * crossprodJ0Y0( xio, xii )
      + lambda * xio^2 * crossprodJ0Y0( xii, xio ) ) )
      / ( kH * alpha^2 * xi^2 * xio^2 ):

# Define the arbitrary constant of integration  c_0(t)
C0 := C0num / detA:
# Define C_3
C3 := C3num / detA:

# To compute C1J1(xi) + C2Y1(xi) define the numerator as
C1J1C2Y1num := r -> 2 * G * ( pHi - pHo ) * ( ( lambda + 2 * G )
      * ( xi ^2 * crossprodJ1Y0( xi( r ),  xii  )
      - xio^2 * crossprodJ1Y0( xi( r ),  xio  ) )
      - 2 * G * (xii * crossprodJ1Y1( xi( r ),  xii  )
      - xio * crossprodJ1Y1( xi( r ),  xio  ) ) )
      / ( alpha * xi ^2 * xio^2 ):

# To compute C1J0(xi) + C2Y0(xi) define the numerator as
C1J0C2Y0num := r -> 2 * G * ( pHi - pHo ) * ( ( lambda + 2 * G )
      * ( xi ^2 * crossprodJ0Y0( xi( r ),  xii  )
      - xio^2 * crossprodJ0Y0( xi( r ),  xio  ) )
      - 2 * G * ( xi  * crossprodJ0Y1( xi( r ),  xii  )
      - xio * crossprodJ0Y1( xi( r ),  xio  ) ) )
      / ( alpha * xi ^2 * xio^2 ):

# The displacement amplitude is defined by
U := r -> C1J1C2Y1num( r ) / detA - C0 / ( alpha * xi( r ) ):
# and the dimension-full displacement is thus
u := ( r,  t  ) -> cd / fr * U( r ) * exp( I * omega * t ):

# The pressure amplitude is defined by
P := r -> - I * wH * C1J0C2Y0num( r ) / ( kH * alpha * detA )
      - wH^2 * C0 * ln( rH( r ) ) / ( kH * alpha^2 ) + C3:
# and the dimension-full pressure in mmHg is thus
p := ( r,  t  ) -> ( pave + mu * fr * P( r ) * exp( I * omega * t ) )
      / convertmmHgPa:

# The dimension-full filtration velocity  is  defined  by
W := ( r, t  ) -> ( - I * omega * cd / fr * C1J1C2Y1num( r ) / detA
```

```
    + cd^2 * omega^2 * C0 / ( alpha^2 * fr^3 * r ) )
    * exp( I * omega * t ):

# Assuming parameter values that describe NPH
# the displacement in micrometers is given by
NPHu := ( r, t ) -> 1e6 * Re ( evalf ( subs ( omega = 6, mu = 1e-3,
    k = 1e-14, rho = 1e3, E = 21000, nu = 0.4,
    pave = 13 * convertmmHgPa, pii = 0.5 * 9.4 * convertmmHgPa,
    po = 0.5 * 9.0 * convertmmHgPa, u( r, t ) ) ) ):

# the pressure in mmHg is given by
NPHp := ( r, t ) -> Re ( evalf ( subs ( omega = 6, mu = 1e-3,
    k = 1e-14, rho = 1e3, E = 21000, nu = 0.4,
    pave = 13 * convertmmHgPa, pii = 0.5 * 9.4 * convertmmHgPa,
    po = 0.5 * 9.0 * convertmmHgPa, p( r, t ) ) ) ):

# and the filtration  velocity  in micrometers/second is given by
NPHW := ( r, t ) -> 1e6 * Re ( evalf ( subs ( omega = 6, mu = 1e-3,
    k = 1e-14, rho = 1e3, E = 21000, nu = 0.4,
    pave = 13 * convertmmHgPa, pii = 0.5 * 9.4 * convertmmHgPa,
    po = 0.5 * 9.0 * convertmmHgPa, W( r, t ) ) ) ):
```

Appendix B

Details of the Fractional Zener Viscoelastic Model

B.1 Computing the Mittag-Leffler Function

Algorithms for the numerical computation of the generalized Mittag-Leffler function,

$$E_{\alpha,\beta}(z) = \sum_{k=0}^{\infty} \frac{z^k}{\Gamma(\beta + \alpha k)} \tag{B.1}$$

for $\alpha \in \mathbb{R}^+$, $\beta \in \mathbb{R}$, and $z \in \mathbb{C}$ have been presented by Gorenflo *et al.* in [45, 44] and by Diethelm *et al.* [24]. For small $|z|$, we use the definition to compute the function since all the instances in this thesis satisfy $z < 0$ and so the series is alternating and arbitrary accuracy can be achieved. Unfortunately, when $|z|$ is large, this series is extremely slow to converge. Thus, the asymptotic representation is required:

$$E_{\alpha,\beta} = -\sum_{k=1}^{k_1} \frac{z^{-k}}{\Gamma(\beta - \alpha k)} + \mathcal{O}(|z|^{-(1+k_1)}) \text{ as } |z| \to \infty \tag{B.2}$$

for $|\arg(z)| \geq \frac{3\alpha\pi}{4}$ where $k_1 = \lfloor -\ln(\epsilon)/\ln(|z|) \rfloor$ and ϵ is the machine precision. The magnitude at which the transition between these two expressions occurs is $|z| = \lfloor 10 + 5\alpha \rfloor$.

In the fractional Zener viscoelastic models, the generalized Mittag-Leffler function is multiplied by $t^{\alpha-1}$ and then convolved with the pressure function.

Recall that the infant and adult displacements are given by

$$\begin{aligned} u_I(r,t) =& \frac{a^2}{b^2-a^2}\left[\left(\frac{3r}{6K+E_0}+\frac{b^2}{E_0 r}\right)p_i(t)\right. \\ &+\frac{b^2(E_0-E_\infty)}{E_0^2\tau^\alpha r}p_i(t)*t^{\alpha-1}E_{\alpha,\alpha}\left(-\frac{E_\infty}{E_0}\left(\frac{t}{\tau}\right)^\alpha\right) \\ &\left.+\frac{3r(E_0-E_\infty)}{(6K+E_0)^2\tau^\alpha}p_i(t)*t^{\alpha-1}E_{\alpha,\alpha}\left(-\frac{6K+E_\infty}{6K+E_0}\left(\frac{t}{\tau}\right)^\alpha\right)\right] \end{aligned} \tag{B.3}$$

and

$$\begin{aligned} u_A(r,t) =& \left(\frac{b}{r}-\frac{r}{b}\right)\left[\frac{3a^2b}{(6K+E_0)a^2+3E_0b^2}p_i(t)\right. \\ &\left.+\frac{3a^2b(a^2+3b^2)(E_0-E_\infty)}{\left((6K+E_0)a^2+3E_0b^2\right)^2\tau^\alpha}p_i(t)*t^{\alpha-1}E_{\alpha,\alpha}\left(-\hat{h}\left(\frac{t}{\tau}\right)^\alpha\right)\right], \end{aligned} \tag{B.4}$$

and that the solution to the mixed boundary value problem is

$$u_m = (1-\delta)u_I + \delta u_A. \tag{B.5}$$

We denote k_0 as the upper limit in the sum for the Mittag-Leffler definition determined by the alternating series and k_1 as the upper limit in the sum for the asymptotic series expression of the Mittag-Leffler function, as $|z|\to\infty$ for $|\arg(z)| \geq \frac{3\alpha\pi}{4}$, determined by $\max\{\lfloor -\ln(\epsilon)/\ln(|z(\zeta)|)\rfloor, \lfloor -\ln(\epsilon)/\ln(|z(t)|)\rfloor\}$, where $\zeta(z)$ is the transition point between the two expressions determined by solving $z(s) = \lfloor 10+5\alpha\rfloor$ for s and letting $\zeta(z)=s$. Each convolution can then be expressed as

$$\begin{aligned} C(t) &= \int_0^t p_i(t-s)s^{\alpha-1}E_{\alpha,\alpha}(-z(s))\,\mathrm{d}s \\ &= \begin{cases} \int_0^t p_i(t-s)s^{\alpha-1}\sum_{k=0}^{k_0}\frac{z(s)^k}{\Gamma(\alpha(1+k))}\,\mathrm{d}s & \text{if } t\leq\zeta(z) \\ \int_0^{\zeta(z)} p_i(t-s)s^{\alpha-1}\sum_{k=0}^{k_0}\frac{z(s)^k}{\Gamma(\alpha(1+k))}\,\mathrm{d}s & \text{otherwise} \\ \quad +\int_{\zeta(z)}^t p_i(t-s)s^{\alpha-1}(-1)\sum_{k=1}^{k_1}\frac{z(s)^{-k}}{\Gamma(\alpha(1-k))}\,\mathrm{d}s & \end{cases} \\ &= \begin{cases} \sum_{k=0}^{k_0}\frac{1}{\Gamma(\alpha(1+k))}\int_0^t p_i(t-s)s^{\alpha-1}z(s)^k\,\mathrm{d}s & \text{if } t\leq\zeta(z) \\ \sum_{k=0}^{k_0}\frac{1}{\Gamma(\alpha(1+k))}\int_0^{\zeta(z)} p_i(t-s)s^{\alpha-1}z(s)^k\,\mathrm{d}s & \text{otherwise} \\ \quad -\sum_{k=1}^{k_1}\frac{1}{\Gamma(\alpha(1-k))}\int_{\zeta(z)}^t p_i(t-s)s^{\alpha-1}z(s)^{-k}\,\mathrm{d}s & \end{cases} \end{aligned}$$

B.1.1 `Maple` Code

The following is the `Maple` script used to compute the infant tissue displacement for the mixed boundary value problem.

```
# Mixed_Disp_Final2.mw
# Compute mixed BC infant brain displacement using definition and
# asymptotic expansion of the Mittag−Leffler function
# no integral representation
#
# outer boundary condition sigma_rr = delta*(stress in adult at r=b)
# causing a mix of the two solutions

Digits := 40;
K := 2.1*10^9;          # bulk modulus
alpha := 0.779;         # fractional order
E0 := 6678;             # initial elatic modulus
Einf := 621;            # steady−state elastic modulus
tau := 0.000110;        # relaxtion time
P := 667;               # pressure wave amplitude
omega := 7;             # angular frequency
a := 0.03;              # inner radius
b := 0.1;               # outer radius
tol := 10.0^(−12);      # tolerance (precision )

fh := (6*K+Einf)*a^2+3*Einf*b^2;
gh := (6*K+E0)*a^2+3*E0*b^2;
hh := fh/gh;
z1 := s −> −(Einf+6*K)/(E0+6*K)*(s/tau)^alpha;
z2 := s −> −Einf/E0*(s/tau)^alpha;
z3 := s −> −hh*(s/tau)^alpha;

# proceedure to calculute number of terms for ML definition
maxk := proc (aa, z, tol)
  local k;
  k := 1;
  while tol < evalf(abs(z^k/GAMMA(aa*(k+1)))) do
    k := k+2
  end do;
  return k
end proc:

# values of s where transition occurs between ML definiton and
# asymptotic expansion
break2 := floor(10+5*alpha);
s1b2 := evalf((break2/abs(z1(1)))^(1/alpha));
s2b2 := evalf((break2/abs(z2(1)))^(1/alpha));
s3b2 := evalf((break2/abs(z3(1)))^(1/alpha));

# tissue displacement
u := (delta,r,t) −> u1(delta,r,t) + u2(delta,r,t) + u3(delta,r,t);
```

```
u1 := (delta,r,t) -> evalf(a^2/(b^2-a^2)
        *((1-delta*(b^2*(4*E0+6*K))/gh)*3*r/(E0+6*K)
          +(1-delta*(a^2*(4*E0+6*K))/gh)*b^2/(E0*r))*P*cos(omega*t));
u3 := (delta,r,t) -> evalf(delta*(3*a^2*(a^2+3*b^2)
        *(E0-Einf)*tau^(-alpha))/gh^2*(b^2/r-r)*P*ConvC(t));
u2 := (delta,r,t) -> evalf(a^2/(b^2-a^2)*(E0-Einf)*(1-delta)*tau^(-alpha)
        *P*(3*r/(E0+6*K)^2*ConvA(t)+b^2/(r*E0^2)*ConvB(t)));

# using z1(t) we can calculate the convolution ConvA
ConvA := proc (t)
  local kk, temp, k1A, kmaxA;
  kmaxA := maxk(alpha, z1(s1b2), tol);
  temp := 0;
  if t < s1b2 then
    for kk from 0 to kmaxA do
      temp := temp + eval(z1(1)^k
              *(int(cos(omega*(t-s))*s^(alpha*(k+1)-1),s=0. .. t))
              /GAMMA(alpha*(k+1)), k = kk);
    end do;
  else
    for kk from 0 to kmaxA do
      temp := temp + eval(z1(1)^k
              *(int(cos(omega*(t-s))*s^(alpha*(k+1)-1), s=0. .. s1b2))
              /GAMMA(alpha*(k+1)), k = kk);
    end do;
    k1A := max(floor(-ln(tol)/ln(abs(z1(s1b2)))),
               floor(-ln(tol)/ln(abs(z1(5)))));
    temp := temp + Re(-1*add(z1(1)^(-k)
                    *(int(cos(omega*(t-s))*s^(alpha*(1-k)-1), s = s1b2 .. t))
                    /GAMMA(alpha*(1-k)), k = 1 .. k1A));
  end if:
  return temp;
end proc:

# using z2(t) we can calculate the convolution ConvB
ConvB := proc (t)
  local kk, temp, kmaxB, k1B;
  kmaxB := maxk(alpha, z2(s2b2), tol);
  temp := 0;
  if t < s2b2 then
    for kk from 0 to kmaxB do
      temp := temp + eval(z2(1)^k
              *(int(cos(omega*(t-s))*s^(alpha*(k+1)-1), s=0. .. t))
              /GAMMA(alpha*(k+1)), k = kk);
  end do;
  else
```

```
    for kk from 0 to kmaxB do
      temp := temp + eval(z2(1)^k
              *(int(cos(omega*(t-s))*s^(alpha*(k+1)-1), s= 0. .. s2b2))
              /GAMMA(alpha*(k+1)), k = kk);
  end do;
  k1B := max(floor(-ln(tol)/ln(abs(z2(s2b2)))),
             floor(-ln(tol)/ln(abs(z2(5)))));
  temp := temp + Re(-1*add(z2(1)^(-k)
                  *(int(cos(omega*(t-s))*s^(alpha*(1-k)-1), s = s2b2 .. t))
                  /GAMMA(alpha*(1-k)), k = 1 .. k1B));
  end if:
  return temp;
end proc:

# using z3(t) we can calculate the convolution ConvC
ConvC := proc (t)
  local kk, temp, kmaxC, k1C;
  kmaxC := maxk(alpha, z3(s3b2), tol);
  temp := 0;
  if t < s3b2 then
    for kk from 0 to kmaxC do
      temp := temp + eval(z3(1)^k
              *(int(cos(omega*(t-s))*s^(alpha*(k+1)-1), s = 0. .. t))
              /GAMMA(alpha*(k+1)), k = kk);
    end do;
  else
    for kk from 0 to kmaxC do
      temp := temp + eval(z3(1)^k
              *(int(cos(omega*(t-s))*s^(alpha*(k+1)-1), s=0. .. s3b2))
              /GAMMA(alpha*(k+1)), k = kk);
    end do;
    k1C := max(floor(-ln(tol)/ln(abs(z3(s3b2)))),
               floor(-ln(tol)/ln(abs(z3(5)))));
    temp := temp + Re(-1*add(z3(1)^(-k)
                    *(int(cos(omega*(t-s))*s^(alpha*(1-k)-1), s = s3b2 .. t))
                    /GAMMA(alpha*(1-k)), k = 1 .. k1C));
  end if:
  return temp;
end proc:

# To avoid recalculating the convolutions, precalculate them
# and then find the displacements at three points in parenchyma
t_Data := [seq(evalf(i/20+0.01), i= 0 .. 60)]:   # t from 0.01 .. 3
CA_Data := []:
CB_Data := []:
CC_Data := []:
```

```
for tt in t_Data do
   CA_Data := [op(CA_Data), ConvA(tt)];
   CB_Data := [op(CB_Data), ConvB(tt)];
   CC_Data := [op(CC_Data), ConvC(tt)];
end do:

# calculuate displacement at r=a
u1_Data_ra := eval(a^2/(b^2-a^2)*(
                (1-delta*(b^2*(4*E0+6*K))/gh)*3*r/(E0+6*K)
                +(1-delta*(a^2*(4*E0+6*K))/gh)*b^2/(E0*r))
                *P*[seq(cos(omega*t),t in t_Data)], {r = a, delta = 0.5}):
u2_Data_ra := eval(a^2/(b^2-a^2)*(E0-Einf)*(1-delta)*tau^(-alpha)*P
                *(3*r/(E0+6*K)^2*CA_Data+b^2/(r*E0^2)*CB_Data),
                {r = a, delta = 0.5}):
u3_Data_ra := eval(delta*(3*a^2*(a^2+3*b^2)*(E0-Einf)*tau^(-alpha))/gh^2
                *(b^2/r-r)*P*CC_Data, {r = a, delta = 0.5}):

# calculuate displacement at r=0.5(a+b)
u1_Data_rm := eval(a^2/(b^2-a^2)*(
                (1-delta*(b^2*(4*E0+6*K))/gh)*3*r/(E0+6*K)
                +(1-delta*(a^2*(4*E0+6*K))/gh)*b^2/(E0*r))*P
                *[seq(cos(omega*t),t in t_Data)], {r = 0.5*(a+b), delta = 0.5}):
u2_Data_rm := eval(a^2/(b^2-a^2)*(E0-Einf)*(1-delta)*tau^(-alpha)*P
                *(3*r/(E0+6*K)^2*CA_Data+b^2/(r*E0^2)*CB_Data),
                {r = 0.5*(a+b), delta = 0.5}):
u3_Data_rm := eval(delta*(3*a^2*(a^2+3*b^2)*(E0-Einf)*tau^(-alpha))/gh^2
                *(b^2/r-r)*P*CC_Data, {r = 0.5*(a+b), delta = 0.5}):

# calculuate displacement at r=b
u1_Data_rb := eval(a^2/(b^2-a^2)*(
                (1-delta*(b^2*(4*E0+6*K))/gh)*3*r/(E0+6*K)
                +(1-delta*(a^2*(4*E0+6*K))/gh)*b^2/(E0*r))
                *P*[seq(cos(omega*t),t in t_Data)], {r = b, delta = 0.5}):
u2_Data_rb := eval(a^2/(b^2-a^2)*(E0-Einf)*(1-delta)*tau^(-alpha)
                *P*(3*r/(E0+6*K)^2*CA_Data+b^2/(r*E0^2)*CB_Data),
                {r = b, delta = 0.5}):
u3_Data_rb := eval(delta*(3*a^2*(a^2+3*b^2)*(E0-Einf)*tau^(-alpha))/gh^2
                *(b^2/r-r)*P*CC_Data, {r = b, delta = 0.5}):

# combine displacement pieces
u_Data_ra := u1_Data_ra + u2_Data_ra + u3_Data_ra:
u_Data_rM := u1_Data_rm + u2_Data_rm + u3_Data_rm:
u_Data_rb := u1_Data_rb + u2_Data_rb + u3_Data_rb:

# create arrays for plotting
Disp_ra := []:
```

```
Disp_rM := []:
Disp_rb := []:
for ii  from 1 to nops(u_Data_ra) do
  Disp_ra := [op(Disp_ra), [t_Data[ii ],  1e3*u_Data_ra[ii]]];
  Disp_rM := [op(Disp_rM), [t_Data[ii],  1e3*u_Data_rM[ii]]];
  Disp_rb := [op(Disp_rb), [t_Data[ii ],  1e3*u_Data_rb[ii]]];
end do:

# save data for later  since  computation takes a long time
save(Disp_ra, Disp_rM, Disp_rb, "Mixed_DispData_Final.out");

# plot displacement of mixed BC infant brain
plot([Disp_ra,Disp_rM,Disp_rb], labels = ["Time [s]","[mm]"],
     title  = "Infant Displacement with Mixed BC",
     legend = ["r=a", "r=0.5(a+b)", "r=b"], thickness = 3,
     color = [black, red,  blue],  linestyle = [1, 3,  2],
     view = [0..3, −20..20],  font = [TIMES, ROMAN, 14],
     legendstyle = [font = [TIMES, ROMAN, 14]],
     labeldirections = [horizontal, vertical ]);

# determine max displacement of venticle wall
max_ura := 0:
max_t := 0:
for ii  from 1 to nops(u_Data_ra) do
   if  max_ura < u_Data_ra[ii] then
       max_ura := u_Data_ra[ii];
       max_t := t_Data[ii];
   end if;
end do:
1e3*max_ura;
max_t;

# plot displacement as a function of mixing parameter delta
unassign('delta');
plot(1e3*u(d, a, .9),  d = 0 .. 1,  thickness = 3,
     title  = "Infant Displacement with Mixed Boundary Condition",
     labels = [delta,  "[mm]"], view = [0..1, 0..40],
     font = [TIMES, ROMAN, 14], labeldirections = [horizontal, vertical],
     legend = ["r=a at t=0.9 s"], legendstyle = [font = [TIMES, ROMAN, 14]]);
```

Appendix C

Details of the Fractional Hyper-Viscoelastic Model

In Section C.1, after presenting the necessary background on convected curvilinear coordinates, we determine the deformation gradients and deformation tensor used in Chapter 7 to derive the quasilinear fractional hyper-viscoelastic model. In Section C.2, we present the Laplace Transform method for solving the small strain equation of motion for this model.

C.1 Model Co-ordinate Systems and the Deformation Tensor

The thick-walled cylinder model geometry has initial configuration, B, for $t \leq 0$, with the cylindrical co-ordinate system (R, Θ, Z) and unit direction vectors $(\hat{\mathrm{e}}_R, \hat{\mathrm{e}}_\Theta, \hat{\mathrm{e}}_Z)$. The inner boundary is $R = R_1$, the outer boundary is $R = R_2$, and the unit base vectors for this undeformed state are

$$\begin{aligned}
\hat{\mathrm{e}}_R &= \cos\Theta\,\hat{\imath} + \sin\Theta\,\hat{\jmath} \\
\hat{\mathrm{e}}_\Theta &= -\sin\Theta\,\hat{\imath} + \cos\Theta\,\hat{\jmath} \\
\hat{\mathrm{e}}_Z &= \hat{k}.
\end{aligned}$$

For $t > 0$, the cylinder is in a deformed state b due to the applied boundary conditions of $\sigma_r(t, r_1) = -p_0(t)$ and $\sigma_r(t, r_2) = 0$, with the cylindrical co-ordinate system (r, θ, z) and unit direction vectors $(\hat{\mathrm{e}}_r, \hat{\mathrm{e}}_\theta, \hat{\mathrm{e}}_z)$. In this deformed state, the inner boundary is $r = r_1$, the outer boundary is $r = r_2$, and the unit

base vectors are

$$\begin{aligned}\hat{\mathrm{e}}_r &= \cos\theta\,\hat{\imath} + \sin\theta\,\hat{\jmath}\\ \hat{\mathrm{e}}_\theta &= -\sin\theta\,\hat{\imath} + \cos\theta\,\hat{\jmath}\\ \hat{\mathrm{e}}_z &= \hat{k}.\end{aligned}$$

Assuming the ends of the cylinder are tethered, the boundary conditions cause radially symmetric planar deformations to occur:

$$r = f(t, R), \qquad \theta = \Theta, \qquad z = Z, \tag{C.1}$$

where $f(t, R)$ is the deformation function to be determined.

C.1.1 Convected Co-ordinates

Assume the X^I co-ordinate system is embedded in B so that it deforms with the body and the x^i co-ordinate system coincides with the X^I system at all times during the deformation. Hence, while in motion, each point keeps the same labels (so $x^i = X^I$). By using convected co-ordinates we lose the flexibility to choose the deformed co-ordinate system to take advantage of symmetries but the resulting basic equations are simpler in form.

General Curvilinear Co-ordinates: (x^1, x^2, x^3)

Consider a set of base vectors $\vec{g}_i$ tangent to the x^i-curves at each point in space, but not necessarily unit vectors or dimensionless as $\vec{g}_i$ can change in magnitude and direction as you move along the co-ordinate curves. A vector $\vec{a}$ can be expressed with respect to the standard orthonormal base vectors via $\vec{a} = \hat{a}^i\hat{\mathrm{e}}_i$ or with respect to the covariant base vectors via $\vec{a} = a^i\vec{g}_i$, where a^i are the contravariant components of $\vec{a}$ relative to the covariant base vectors $\vec{g}_i$.

The covariant base vectors of the undeformed (B) and deformed (b) states are $\vec{G}_I$ and $\vec{g}_i$ respectively, and these base vectors are tangent to the X^I and x^i co-ordinate curves at some point P in B which deforms into p in b. The radius vector in the undeformed state B is

$$\vec{R} = R\hat{\mathrm{e}}_R + Z\hat{\mathrm{e}}_Z = R(\cos\Theta\,\hat{\imath} + \sin\Theta\,\hat{\jmath}) + Z\hat{k}, \tag{C.2}$$

and the radius vector in the deformed state b is

$$\vec{r}(t) = f(t, R)\hat{\mathrm{e}}_r + z\hat{\mathrm{e}}_z = f(t, R)(\cos\theta\,\hat{\imath} + \sin\theta\,\hat{\jmath}) + z\hat{k}. \tag{C.3}$$

We use the notation $\vec{\xi}_{,y}$ to denote differentiation of $\vec{\xi}$ with respect to y. Thus, the covariant base vectors of B are

$$\vec{G}_I = \begin{cases} \vec{G}_1 = \vec{R}_{,R} = \hat{\mathrm{e}}_R & \text{for } I = 1\\ \vec{G}_2 = \vec{R}_{,\Theta} = R\,\hat{\mathrm{e}}_\Theta & \text{for } I = 2\\ \vec{G}_3 = \vec{R}_{,Z} = \hat{\mathrm{e}}_Z & \text{for } I = 3 \end{cases} \tag{C.4}$$

and the covariant base vectors of b are

$$\vec{g}_i = \begin{cases} \vec{g}_1 = \vec{r}_{,r} = \hat{\mathrm{e}}_r & \text{for } i = 1 \\ \vec{g}_2 = \vec{r}_{,\theta} = f(t,R)\,\hat{\mathrm{e}}_\theta & \text{for } i = 2 \\ \vec{g}_3 = \vec{r}_{,z} = \hat{\mathrm{e}}_z & \text{for } i = 3. \end{cases} \tag{C.5}$$

The convected covariant base vectors, $\vec{g}_{I^*}$, are tangent to the convected X^I co-ordinate curves at p and are defined by

$$\vec{g}_{I^*} = \begin{cases} \vec{g}_{1^*} = \vec{r}_{,R} = f_R(t,R)\,\hat{\mathrm{e}}_r & \text{for } I = 1 \\ \vec{g}_{2^*} = \vec{r}_{,\Theta} = f(t,R)\,\hat{\mathrm{e}}_\theta & \text{for } I = 2 \\ \vec{g}_{3^*} = \vec{r}_{,Z} = \hat{\mathrm{e}}_z & \text{for } I = 3. \end{cases} \tag{C.6}$$

The deformation gradient can be computed in terms of the convected base vectors $\vec{g}_{I^*}$ and the reciprocal or contravariant base vectors $\vec{G}^I$. The contravariant base vectors, or dual vectors, are defined by $\vec{G}_I \cdot \vec{G}^J = \delta_I^J$, which gives from (C.4),

$$\vec{G}^I = \begin{cases} \vec{G}^1 = \hat{\mathrm{e}}_R & \text{for } I = 1 \\ \vec{G}^2 = \frac{1}{R}\,\hat{\mathrm{e}}_\Theta & \text{for } I = 2 \\ \vec{G}^3 = \hat{\mathrm{e}}_Z & \text{for } I = 3. \end{cases} \tag{C.7}$$

The contravariant base vectors for b, $\vec{g}^i$, may be found as above, but instead we demonstrate a different approach as discussed by Drozdov [30]. Let V be defined by

$$V = \vec{g}_1 \cdot (\vec{g}_2 \times \vec{g}_3) = \vec{g}_2 \cdot (\vec{g}_3 \times \vec{g}_1) = \vec{g}_3 \cdot (\vec{g}_1 \times \vec{g}_2) = r = f(t,R),$$

then

$$\vec{g}^1 = \frac{\vec{g}_2 \times \vec{g}_3}{V}, \qquad \vec{g}^2 = \frac{\vec{g}_3 \times \vec{g}_1}{V}, \qquad \vec{g}^3 = \frac{\vec{g}_1 \times \vec{g}_2}{V}$$

and the contravariant base vectors of b are

$$\vec{g}^i = \begin{cases} \vec{g}^1 = \hat{\mathrm{e}}_r & \text{for } i = 1 \\ \vec{g}^2 = \frac{1}{f}\,\hat{\mathrm{e}}_\theta & \text{for } i = 2 \\ \vec{g}^3 = \hat{\mathrm{e}}_z & \text{for } i = 3. \end{cases} \tag{C.8}$$

In a similar manner, the convected contravariant base vectors, $\vec{g}^{I^*}$, are

$$\vec{g}^{I^*} = \begin{cases} \vec{g}^{1^*} = \frac{1}{f_R}\,\hat{\mathrm{e}}_r & \text{for } I = 1 \\ \vec{g}^{2^*} = \frac{1}{f}\,\hat{\mathrm{e}}_\theta & \text{for } I = 2 \\ \vec{g}^{3^*} = \hat{\mathrm{e}}_z & \text{for } I = 3. \end{cases} \tag{C.9}$$

C.1.2 Gradients and Tensors

In this section, we find the deformation gradients and deformation tensor necessary for the model derivation presented in Chapter 7.

Deformation Gradient

The deformation gradient bi-tensor $\mathbf{F}$ is a gradient of the map $\vec{r}(t,R)$ which characterizes the map in a small neighbourhood of any point. If a map preserves orientation then $\det \mathbf{F} > 0$. The deformation gradient is defined using Einstein's notation as

$$\begin{aligned}\mathbf{F} &= \vec{g}_{I^*}\vec{G}^I \\ &= \vec{g}_{1^*}\vec{G}^1 + \vec{g}_{2^*}\vec{G}^2 + \vec{g}_{3^*}\vec{G}^3 \\ &= f_R\hat{\mathrm{e}}_r\hat{\mathrm{e}}_R + f\hat{\mathrm{e}}_\theta\frac{1}{R}\hat{\mathrm{e}}_\Theta + \hat{\mathrm{e}}_z\hat{\mathrm{e}}_Z\end{aligned}$$

or

$$\mathbf{F}(t,R) = h(t,R)\hat{\mathrm{e}}_r\hat{\mathrm{e}}_R + \frac{f(t,R)}{R}\hat{\mathrm{e}}_\theta\hat{\mathrm{e}}_\Theta + \hat{\mathrm{e}}_z\hat{\mathrm{e}}_Z, \tag{C.10}$$

where $h(t,R) = f_R(t,R)$. The stretch ratios of the deformation are $\lambda_1 = h$, $\lambda_2 = \dfrac{f}{R}$, and $\lambda_3 = 1$.

Relative Deformation Gradient

The relative deformation gradient is the tensor $\mathbf{F}_{\boldsymbol{\tau}}$ defined by

$$\mathbf{F}_{\boldsymbol{\tau}}(t,R) = \mathbf{F}(t,R)\cdot\big(\mathbf{F}(\tau,R)\big)^{-1} \tag{C.11}$$

and it characterizes the entire history of the deformation on the interval $[0,t]$. Using the definition of $\mathbf{F}$ gives

$$\mathbf{F}_{\boldsymbol{\tau}}(t,R) = \big(g_{I^*}(t)G^I(t)\big)\cdot\big(G_J(\tau)g^{J^*}(\tau)\big) = g_{I^*}(t)\delta^I_J g^{J^*}(\tau) = g_{I^*}(t)g^{I^*}(\tau),$$

which allows for easy computation:

$$\begin{aligned}\mathbf{F}_{\boldsymbol{\tau}}(t,R) &= \vec{g}_{1^*}(t)\vec{g}^{1^*}(\tau) + \vec{g}_{2^*}(t)\vec{g}^{2^*}(\tau) + \vec{g}_{3^*}(t)\vec{g}^{3^*}(\tau) \\ &= \frac{h(t,R)}{h(\tau,R)}\hat{\mathrm{e}}_r\hat{\mathrm{e}}_r + \frac{f(t,R)}{f(\tau,R)}\hat{\mathrm{e}}_\theta\hat{\mathrm{e}}_\theta + \hat{\mathrm{e}}_z\hat{\mathrm{e}}_z.\end{aligned} \tag{C.12}$$

Left Cauchy-Green Deformation Tensor

The Left Cauchy-Green deformation tensor describes deformations that do not lead to a change in the position vector $\vec{r}$ relative to the coordinate system embedded in the material, b. Examples of deformations that are excluded by this description are rotations and translations. The left Cauchy-Green tensor, $\mathbf{B}$, is defined by

$$\begin{aligned}\mathbf{B}(t,R) &= \mathbf{F}(t,R)\cdot\big(\mathbf{F}(t,R)\big)^{\mathrm{T}} \\ &= \big(g_{I^*}G^I\big)\cdot\big(G^J g_{J^*}\big) \\ &= h^2(t,R)\hat{\mathrm{e}}_r\hat{\mathrm{e}}_r + \frac{f^2(t,R)}{R^2}\hat{\mathrm{e}}_\theta\hat{\mathrm{e}}_\theta + \hat{\mathrm{e}}_z\hat{\mathrm{e}}_z,\end{aligned} \tag{C.13}$$

Note that $(\cdot)^{\mathrm{T}}$ denotes the transpose operation. The principal invariants of $\mathbf{B}$ are given by

$$\begin{cases} I_1 = \mathbf{B}_{11} + \mathbf{B}_{22} + \mathbf{B}_{33} \\ I_2 = \mathbf{B}_{11}\mathbf{B}_{22} + \mathbf{B}_{22}\mathbf{B}_{33} + \mathbf{B}_{11}\mathbf{B}_{33} - \mathbf{B}_{12}^2 - \mathbf{B}_{21}^2 - \mathbf{B}_{13}^2 \\ I_3 = \mathbf{B}_{11}\mathbf{B}_{22}\mathbf{B}_{33}, \end{cases} \tag{C.14}$$

which in this case gives

$$\begin{cases} I_1 = h^2(t) + \frac{f^2(t)}{R^2} + 1 \\ I_2 = h^2(t)\frac{f^2(t)}{R^2} + h^2(t) + \frac{f^2(t)}{R^2} \\ I_3 = h^2(t)\frac{f^2(t)}{R^2}. \end{cases} \tag{C.15}$$

C.2 Solution Via Laplace Transforms

The solution method for solving fractional differential equations with Laplace Transforms was first described by Miller and Ross [81]. Using the Laplace Transform to solve the small strain equation of motion (7.23) gives, after simplification,

$$\bar{B}(s) = \frac{b}{b-1}\frac{\Delta p}{\mu}\left(\frac{1}{s} - \frac{s^{\alpha-1}}{s^\alpha + \frac{\mu}{\eta}}\right).$$

With $\alpha = \frac{4}{5}$ and $-x^4 = \frac{\mu}{\eta}$ this becomes

$$\bar{B}(s) = \frac{b}{b-1}\frac{\Delta p}{\mu}\left(\frac{1}{s} - \frac{s^{-\frac{1}{5}}}{s^{\frac{4}{5}} - x^4}\right). \tag{C.16}$$

The term $-\frac{s^{-\frac{1}{5}}}{s^{\frac{4}{5}}-x^4}$ must be rewritten in a form appropriate for the inverse Laplace Transform. Using long division, the denominator is factored into irreducible factors, giving

$$s^{\frac{4}{5}} - x^4 = (s^{\frac{1}{5}} - x)(s^{\frac{1}{5}} + x)(s^{\frac{1}{5}} - ix)(s^{\frac{1}{5}} + ix).$$

Next, a partial fractions expansion is sought with numerators of the form $C_k s^{-\frac{4}{5}}$ for $k = 1 \ldots 4$, and where C_k are constants. In this instance, we get

$$-\frac{s^{-\frac{1}{5}}}{s^{\frac{4}{5}} - x^4} = -\frac{\frac{1}{4}s^{-\frac{4}{5}}}{s^{\frac{1}{5}} + x} - \frac{\frac{1}{4}s^{-\frac{4}{5}}}{s^{\frac{1}{5}} - x} - \frac{\frac{1}{4}s^{-\frac{4}{5}}}{s^{\frac{1}{5}} + ix} - \frac{\frac{1}{4}s^{-\frac{4}{5}}}{s^{\frac{1}{5}} - ix}.$$

Again, long division is used to simplify each term. Using the fact that

$$(s^{\frac{1}{5}} + x)(s^{\frac{4}{5}} - s^{\frac{3}{5}}x + s^{\frac{2}{5}}x^2 - s^{\frac{1}{5}}x^3 + x^4) = s + x^5,$$

and similar expressions for $(s^{\frac{1}{5}} - x)$, $(s^{\frac{1}{5}} + ix)$, and $(s^{\frac{1}{5}} - x)$, gives

$$-\frac{s^{-\frac{1}{5}}}{s^{\frac{4}{5}} - x^4} = -\frac{1}{4}\left(\frac{1 - s^{-\frac{1}{5}}x + s^{-\frac{2}{5}}x^2 - s^{-\frac{3}{5}}x^3 + s^{-\frac{4}{5}}x^4}{s + x^5}\right.$$
$$+ \frac{1 + s^{-\frac{1}{5}}x + s^{-\frac{2}{5}}x^2 + s^{-\frac{3}{5}}x^3 + s^{-\frac{4}{5}}x^4}{s - x^5}$$
$$+ \frac{1 - s^{-\frac{1}{5}}ix + s^{-\frac{2}{5}}(ix)^2 - s^{-\frac{3}{5}}(ix)^3 + s^{-\frac{4}{5}}(ix)^4}{s + (ix)^5}$$
$$\left. + \frac{1 + s^{-\frac{1}{5}}ix + s^{-\frac{2}{5}}(ix)^2 + s^{-\frac{3}{5}}(ix)^3 + s^{-\frac{4}{5}}(ix)^4}{s - (ix)^5}\right).$$

This form can now be transformed back to t-space using the inverse Laplace Transform. The fractional powers of s in the numerators result in the transformed function being expressed in terms of the Gamma function, defined by,

$$\Gamma(z) = \int_0^\infty s^{z-1}\mathrm{e}^{-s}\mathrm{d}s,$$

and the incomplete Gamma function, defined by,

$$\Gamma(a, z) = \int_z^\infty s^{a-1}\mathrm{e}^{-s}\mathrm{d}s.$$

Substituting these results into (C.16), recalling that $x = \frac{1+i}{\sqrt{2}}\left(\frac{\mu}{\eta}\right)^{\frac{1}{4}}$, and taking the inverse Laplace Transform, gives the small strain function $B(t)$ for

$\alpha = \frac{4}{5}$ as

$$B(t) = \frac{b}{b-1}\frac{\Delta p}{\mu}\Bigg[1 - \frac{1}{4}\mathrm{e}^{-x^5 t}\Bigg(1 - (-1)^{-\frac{1}{5}}\left(1 - \tfrac{1}{\pi}\Gamma\left(\tfrac{1}{5}, -x^5 t\right)\Gamma\left(\tfrac{4}{5}\right)\sin\left(\tfrac{\pi}{5}\right)\right)$$
$$+ (-1)^{-\frac{2}{5}}\left(1 - \tfrac{1}{\pi}\Gamma\left(\tfrac{2}{5}, -x^5 t\right)\Gamma\left(\tfrac{3}{5}\right)\sin\left(\tfrac{2\pi}{5}\right)\right)$$
$$- \frac{\Gamma\left(\frac{3}{5}\right) - \Gamma\left(\frac{3}{5}, -x^5 t\right)}{(-1)^{\frac{3}{5}}\Gamma\left(\frac{3}{5}\right)} + \frac{\Gamma\left(\frac{4}{5}\right) - \Gamma\left(\frac{4}{5}, -x^5 t\right)}{(-1)^{\frac{4}{5}}\Gamma\left(\frac{4}{5}\right)}\Bigg)$$
$$- \frac{1}{4}\mathrm{e}^{x^5 t}\Bigg(1 + \left(1 - \tfrac{1}{\pi}\Gamma\left(\tfrac{1}{5}, x^5 t\right)\Gamma\left(\tfrac{4}{5}\right)\sin\left(\tfrac{\pi}{5}\right)\right)$$
$$+ \left(1 - \tfrac{1}{\pi}\Gamma\left(\tfrac{2}{5}, x^5 t\right)\Gamma\left(\tfrac{3}{5}\right)\sin\left(\tfrac{2\pi}{5}\right)\right)$$
$$+ \frac{\Gamma\left(\frac{3}{5}\right) - \Gamma\left(\frac{3}{5}, x^5 t\right)}{\Gamma\left(\frac{3}{5}\right)} + \frac{\Gamma\left(\frac{4}{5}\right) - \Gamma\left(\frac{4}{5}, x^5 t\right)}{\Gamma\left(\frac{4}{5}\right)}\Bigg)$$
$$- \frac{1}{4}\mathrm{e}^{-(ix)^5 t}\Bigg(1 - (-1)^{-\frac{1}{5}}\left(1 - \tfrac{1}{\pi}\Gamma\left(\tfrac{1}{5}, -(ix)^5 t\right)\Gamma\left(\tfrac{4}{5}\right)\sin\left(\tfrac{\pi}{5}\right)\right)$$
$$+ (-1)^{-\frac{2}{5}}\left(1 - \tfrac{1}{\pi}\Gamma\left(\tfrac{2}{5}, -(ix)^5 t\right)\Gamma\left(\tfrac{3}{5}\right)\sin\left(\tfrac{2\pi}{5}\right)\right)$$
$$- \frac{\Gamma\left(\frac{3}{5}\right) - \Gamma\left(\frac{3}{5}, -(ix)^5 t\right)}{(-1)^{\frac{3}{5}}\Gamma\left(\frac{3}{5}\right)} + \frac{\Gamma\left(\frac{4}{5}\right) - \Gamma\left(\frac{4}{5}, -(ix)^5 t\right)}{(-1)^{\frac{4}{5}}\Gamma\left(\frac{4}{5}\right)}\Bigg)$$
$$- \frac{1}{4}\mathrm{e}^{(ix)^5 t}\Bigg(1 + \left(1 - \tfrac{1}{\pi}\Gamma\left(\tfrac{1}{5}, (ix)^5 t\right)\Gamma\left(\tfrac{4}{5}\right)\sin\left(\tfrac{\pi}{5}\right)\right)$$
$$+ \left(1 - \tfrac{1}{\pi}\Gamma\left(\tfrac{2}{5}, (ix)^5 t\right)\Gamma\left(\tfrac{3}{5}\right)\sin\left(\tfrac{2\pi}{5}\right)\right)$$
$$+ \frac{\Gamma\left(\frac{3}{5}\right) - \Gamma\left(\frac{3}{5}, (ix)^5 t\right)}{\Gamma\left(\frac{3}{5}\right)} + \frac{\Gamma\left(\frac{4}{5}\right) - \Gamma\left(\frac{4}{5}, (ix)^5 t\right)}{\Gamma\left(\frac{4}{5}\right)}\Bigg)\Bigg].$$

Glossary

Arachnoid Villi The small protrusions of the arachnoid (the thin layer covering the cortical surface) through the dura mater into the venous sinuses. These are believed to be a site of CSF absorption.

Blood Brain Barrier The tight junctions between endothelial cells of capillary walls that restrict the transcapillary flow of molecules.

Bulk Modulus (K) The measure of a substances resistance to uniform compression, defined by $K = -V\frac{\partial P}{\partial V}$, or the pressure increase required to cause a given relative decrease in volume.

Cerebrospinal Fluid (CSF) The clear colourless liquid that surrounds the brain and spinal cord as well as fills the interior ventricles of the brain. In this Thesis, CSF also refers to any fluid found in the brain tissue, i.e. the interstitial fluid.

Choroid Plexus A collection of ependymal cells and capillaries found in all cerebral ventricles where CSF production mainly occurs.

Communicating Hydrocephalus The class of hydrocephalus where CSF circulates from the ventricles to the spinal SAS but not to the cranial SAS where absorption mainly occurs. The mechanism for ventricular enlargement is unknown for this class because the non-communicating hydrocephalus mechanism of a large pressure gradient does not hold.

Compliance (C) The tendency of a compartment to stretch in response to an internal pressure. It is defined as $C = \frac{\Delta V}{\Delta P}$, or the change in volume that results from a change in pressure.

Edema Sometimes spelled oedema, it is the abnormal accumulation of fluid, and in this Thesis, it refers specifically to accumulated fluid in the extracellular spaces of tissue.

Elastance The reciprocal of compliance, $\frac{\Delta P}{\Delta V}$, it is the change in pressure that results from a change in volume.

Endothelial Cells The cells that line the surface of blood vessels.

Ependyma The thin membrane, consisting of epithelial cells, lining the ventricular system of the brain and spinal cord. Commonly referred to in this Thesis as the ventricle walls.

Extracellular Matrix (ECM) The interstitial structure consisting of fibrous proteins that support the cells of the tissue.

Foramen Magnum The hole in the skull through which the spinal cord connects to the brain.

Hydrocephalus A clinical condition with various causes and no cure that is characterized by the abnormal accumulation of CSF in the enlarged cerebral ventricles.

Integrins Receptors protruding from the cell membrane that bind with the fibers of the ECM to adhere the cell.

Intracranial Pressure (ICP) The pressure of the ventricular CSF.

Intramantle Gradient A pressure gradient from the ventricles to the parenchyma and/or from the SAS to the parenchyma.

Kaolin A clay mineral that is used in solution to induce hydrocephalus in animal experiments by blocking CSF absorption in the cranial SAS.

Lectican A family of proteins commonly found in brain ECM.

Ligand A molecule in the ECM that binds to an integrin receptor. Binding occurs via intermolecular forces.

Non-Communicating Hydrocephalus The class of hydrocephalus where a blockage impedes the normal circulation of CSF and a pressure build up occurs across this blockage, enlarging the ventricles and compressing the brain tissue.

Normal Pressure Hydrocephalus (NPH) A special case of communicating hydrocephalus where the ICP is within the normal range. It most commonly occurs in the elderly population and is often undiagnosed or misdiagnosed as either Alzheimer's disease or Parkinson's disease.

Parenchyma The functional parts of an organ, in the brain this refers to the neurons and glial cells.

Periventricular Region The regions of the brain tissue that surround the ventricles.

Permeability A measure of the ability of a porous material to transmit fluids.

Pressure Volume Index (PVI) A method of evaluating the dynamics of the CSF compartments. It is defined as the volume of fluid necessary to raise the ICP by a factor of 10, that is $\mathrm{PVI} = \Delta V / \log_{10}\left(\frac{P_{peak}}{P_{baseline}}\right)$.

Proteoglycan A core protein attached to one or more long carbohydrate chains commonly found in the ECM.

Shear Modulus (μ) Sometimes called the modulus of rigidity, it is the ratio of the shear stress to the shear strain and thus describes a material's response to shear strains.

Subarachnoid Space (SAS) The region between the membrane surrounding the brain ad spinal cord (pia mater) and the arachnoid membrane, dura mater, and skull.

Transparenchymal (Transmantle) Gradient A pressure gradient from the ventricles across the brain parenchyma to the cranial SAS.

Ventricles Four interconnected regions within the brain that produce CSF and are in free communication with the cranial and spinal SAS as well as the spinal central canal.

Ventriculomegaly A brain condition characterized by enlarged lateral ventricles. In this Thesis it is used interchangeably with hydrocephalus.

Viscosity A measure of a fluid's resistance to flow under shear or tensile stress.

Young's Modulus (E) A measure of the tensile stiffness of a material, it is defined as the ratio of uniaxial stress to uniaxial strain.

Bibliography

[1] Milton Abramowitz and Irene A. Stegun (eds.), *Handbook of mathematical functions with formulas, graphs, and mathematical tables*, U.S. Government, 1972, http://www.math.sfu.ca/ cbm/aands/index.htm.

[2] Hydrocephalus Association, *The stats*, www.hydroassoc.org/about-2/media-resources/the-stats/, May 2010.

[3] World Arnold Chiari Malformation Association, *Cerebrospinal fluid flow and Chiari malformation*, www.pressenter.com/~{}wacma/csf.htm, March 2007.

[4] R.L. Bagley and P.J. Torvik, *Fractional calculus - a different approach to the analysis of viscoelastically damped structures*, AIAA J. **21** (1983), 741–748.

[5] ———, *A theoretical basis for the application of fractional calculus to viscoelasticity*, J. Rheol. **27** (1983), 201–210.

[6] ———, *On the fractional calculus model of viscoelastic behavior*, J. Rheol. **30** (1986), 133–155.

[7] Grant A. Bateman, *The role of altered impedance in the pathophysiology of normal pressure hydrocephalus, Alzheimer's disease and syringomyelia*, Med. Hypotheses **63** (2004), 980–985.

[8] R. Begg, Personal Communication, 2009.

[9] R. Begg and K. Wilkie, *A mechanism for ventricular expansion in communicating hydrocephalus*, Proceedings of the OCCAM-Fields-MITACS Biomedical Problem Solving Workshop, http://www.math.uwaterloo.ca/~kpwilkie/OCCAM_Hydrocephalus_Report.pdf, 2009.

[10] M. Bergsneider, M.R. Egnor, M. Johnston, D. Kranz, J.R. Madsen, J.P. McAllister II, C. Stewart, M.L. Walker, and M.A. Williams, *What we don't (but should) know about hydrocephalus*, J. Neurosurg. (3 Suppl. Pediatrics) **104** (2006), 157–159.

[11] E.A. Bering, *Circulation of the cerebrospinal fluid: Demonstration of the choroid plexuses as the generator of the force for flow of fluid and ventricular enlargement*, J. Neurosurg. **19** (1962), 405–413.

[12] E.A. Bering and O. Sato, *Hydrocephalus: Changes in formation and absorption of cerebrospinal fluid within the cerebral ventricles*, J. Neurosurg. **20** (1963), 1050–1063.

[13] R.A. Bhadelia, A.R. Bogdan, S.M Wolpert, S. Lev, B.A. Appignani, and C.B. Heilman, *Cerebrospinal fluid flow waveforms: Analysis in patients with Chiari I malformation by means of gated phase-contrast MR imaging velocity measurements*, Radiology **196** (1995), 195–202.

[14] M.A. Biot and D.G. Willis, *The elastic coefficients of the theory of consolidation*, J. Appl. Mech. **24** (1957), 594–601.

[15] Maurice A. Biot, *General theory of three-dimensional consolidation*, J. App. Phys. **12** (1941), 155–164.

[16] Robert Burridge and Joseph B. Keller, *Poroelasticity equations derived from microstructure*, J. Acoust. Soc. Am. **70** (1981), no. 4, 1140–1146.

[17] S. Cheng and L.E. Bilston, *Unconfined compression of white matter*, J. Biomech. **40** (2007), 117–124.

[18] K.V. Christ, K.B. Williamson, K.S. Masters, and K.T. Turner, *Measurement of single-cell adhesion strength using a microfluidic assay*, Biomed. Microdevices **12** (2010), no. 3, 443–455.

[19] R.M. Christensen, *Theory of viscoelasticity, an introduction*, ch. 1, pp. 21–25, Academic Press, Inc., 1982.

[20] M.J. Clarke and F.B. Meyer, *The history of mathematical modeling in hydrocephalus*, Neurosurg Focus **22** (2007), no. 4, E3.

[21] H.F. Cserr, C.J. Harling-Berg, and P.M. Knopf, *Drainage of brain extracellular fluid into blood and deep cervical lymph and its immunological significance*, Brain Pathol. **2** (1992), no. 4, 269–276.

[22] M. Czosnyka, Z.H. Czosnyka, P.C. Whitfield, T. Donovan, and J.D. Pickard, *Age dependence of cerebrospinal pressure-volume compensation in patients with hydrocephalus*, J. Neurosurg. **94** (2001), no. 3, 482–486.

[23] G.B. Davis, M. Kohandel, S. Sivaloganathan, and G. Tenti, *The constitutive properties of the brain parenchyma part 2: Fractional derivative approach*, Med. Eng. Phys. **28** (2006), 455–459.

[24] K. Diethelm, N.J. Ford, A.D. Freed, and Y. Luchko, *Algorithms for the fractional calculus: A selection of numerical methods*, Comput. Meth. Appl. Mech. Engrg **194** (2005), 743–773.

[25] J. Dobbing, *The later development of the brain and its vulnerability*, Scientific Foundations of Paediatrics (J.A. Davis and J. Dobbing, eds.), Heinemann Medical, 1974.

[26] C. Dong and X.X. Lei, *Biomechanics of cell rolling: Shear flow, cell-surface adhesion, and cell deformability*, J. Biomech. **33** (2000), no. 1, 35–43.

[27] J.M. Drake, Personal Communication.

[28] C.S. Drapaca, S. Sivaloganathan, and G. Tenti, *Nonlinear constitutive laws in viscoelasticity*, Math. Mech. Solids **12** (2007), no. 5, 475–501.

[29] C.S. Drapaca, G. Tenti, K. Rohlf, and S. Sivaloganathan, *A quasilinear viscoelastic constitutive equation for the brain: Application to hydrocephalus*, J. Elast. **85** (2006), no. 1, 65–83.

[30] Aleksey Drozdov, *Viscoelastic structures: Mechanics of growth and aging*, Academic Press, 1998.

[31] T. Dutta-Roy, A. Wittek, and K. Miller, *Biomechanical modelling of normal pressure hydrocephalus*, J. Biomech. **41** (2008), 2263–2271.

[32] M. Egnor, A. Rosiello, and L. Zheng, *A model of intracranial pulsations*, Pediatr. Neurosurg. **35** (2001), no. 6, 284–298.

[33] M. Egnor, L. Zheng, A. Rosiello, F. Gutman, and R. Davis, *A model of pulsations in communicating hydrocephalus*, Pediatr. Neurosurg. **36** (2002), 281–303.

[34] Per K. Eide, *Comparison of simultaneous continuous intracranial pressure (ICP) signals from ICP sensors placed within the brain parenchyma and the epidural space*, Med. Eng. Phys. (2008), 34–40.

[35] ———, *Demonstration of uneven distribution of intracranial pulsatility in hydrocephalus patients*, J. Neurosurg. **109** (2008), no. 5, 912–917.

[36] M.S. Estes and J.H. McElhaney, *Response of brain tissue of compressive loading*, Proc. 4th ASME J. Biomechanics Conf., 1970.

[37] G.T. Fallenstein, V.D. Hulce, and J.W. Melvin, *Dynamic mechanical properties of human brain tissue*, J. Biomech. **2** (1969), 217–226.

[38] W. Findley, J. Lai, and K. Onaran, *Creep and relaxation of non-linear materials with an introduction to linear viscoelasticity*, North-Holland Series in Applied Mathematics and Mechanics, vol. 18, North-Holland Pub. Co., 1976.

[39] Centers for Disease Control and Prevention, *Table 68. live births, infant, neonatal and postneonatal deaths, and mortality rates mother's hispanic origin and race of mother for non-hispanic origin by 130 selected infant causes: United states, 2001 period data*, Tech. report, http://www.cdc.gov/nchs/data/dvs/LINK01WK68.pdf, 2001.

[40] G. Franceschini, D. Bigoni, P. Regitnig, and G.A. Holzapfel, *Brain tissue deforms similarly to filled elastomers and follows consolidation theory*, J. Mech. Phys. Solids **54** (2006), 2592–2620.

[41] E.K. Franke, *The response of the human skull to mechanical vibrations*, Tech. Report 54–24, Wright-Patterson Air Force Base, Ohio, 1954, WADC Tech. Rep.

[42] Yuan-Cheng Fung, *Biomechanics: Mechanical properties of living tissues*, Springer-Verlag New York Inc., 1981.

[43] J.E. Galford and J.H. McElhaney, *A viscoelastic study of scalp, brain and dura*, J. Biomech. **3** (1970), 211–221.

[44] R. Gorenflo, J. Loutchko, and Y. Luchko, *Corrections to the paper "computation of the Mittag-Leffler function $E_{\alpha,\beta}(z)$ and its derivative"*, Fract. Calc. Appl. Anal. **6** (2003), no. 1, 111–112.

[45] Rudolf Gorenflo, Joulia Loutchko, and Yuri Luchko, *Computation of the Mittag-Leffler function $E_{\alpha,\beta}(z)$ and its derivative*, Fract. Calc. Appl. Anal. **5** (2002), no. 4, 491–518.

[46] D. Greitz, *Cerebrospinal fluid circulation and associated intracranial dynamics - a radiologic investigation using MR imaging and radionuclide cisternography*, Acta Radiologica Suppl. **386** (1993), 1–23.

[47] ———, *Paradigm shift in hydrocephalus research in legacy of Dandy's pioneering work: Rationale for third ventricuolostomy in communicating hydrocephalus*, Childs Nerv. Syst. **23** (2007), no. 5, 487–489.

[48] D. Greitz, R. Wirestam, A. Franck, B. Nordell, C. Thomsen, and F. Stahlberg, *Pulsatile brain movement and associated hydrodynamics studied by magnetic resonance phase imaging. the monro-kellie doctrine revisited*, Neuroradiology **34** (1992), no. 5, 370–380.

[49] James E. Guinane, *Why does hydrocephalus progress?*, J. Neurol. Sci. **32** (1977), 1–8.

[50] S. Hakim, *Biomechanics of hydrocephalus*, Acta Neurol. Latinoamer. **17** (1971), 169–174.

[51] S. Hakim, J.G. Venegas, and J.D. Burton, *The physics of the cranial cavity, hydrocephalus and normal pressure hydrocephalus: Mechanical interpretation and mathematical model*, Surg. Neurol. **5** (1976), 187–210.

[52] H.J. Haubold, A.M. Mathai, and R.K. Saxena, *Mittag-Leffler functions and their applications*, Tech. report, arXiv:0909.0230v2, 2009, http://arxiv.org/abs/0909.0230.

[53] N. Heymans and J.C. Bauwens, *Fractal rheological models and fractional differential equations for viscoelastic behavior*, Rheol. Acta **33** (1994), 210–219.

[54] A.H.S. Holbourn, *Mechanics of head injuries*, Lancet (1943), 438–441.

[55] J.D. Humphrey and K.R. Rajagopal, *A contrained mixture model for growth and remodelling of soft tissues*, Math. Model. Meth. Appl. Sci. **12** (2002), no. 3, 407–430.

[56] H.E. James, *Hydrocephalus in infancy and childhood*, Am. Fam. Phys. **45** (1992), no. 2, 733–742.

[57] R.N. Johnson, C.J. Maffeo, A.B. Butler, J.D. Mann, and N.H. Bas, *Neurobiology of cerebrospinal fluid*, ch. 44: Intracranial Hypertension in Experimental Animals and Man, pp. 697–706, Plenum Press, 1983.

[58] M. Johnston, A. Zakharov, C. Papaiconomou, G. Salmasi, and D. Armstrong, *Evidence of connections between cerebrospinal fluid and nasal lymphatic vessels in humans, non-human primates and other mammalian species*, Cerebrospinal Fluid Res. **1** (2004), no. 1, 2.

[59] M. Kaczmarek, R.P. Subramaniam, and S.R. Neff, *The hydromechanics of hydrocephalus: steady-state solutions for cylindrical geometry*, Bull. Math. Biol. **59** (1997), no. 2, 295–323.

[60] D.E. Kenyon, *Transient filtration in a porous elastic cylinder*, Trans. ASME **43** (1976), no. 4, 594–598.

[61] Stelios K. Kyriacou, Ashraf Mohamed, Karol Miller, and Samuel Neff, *Brain mechanics for neurosurgery: modeling issues*, Biomech. Model. Mechanobiol. **1** (2002), no. 2, 151–164.

[62] E. Lee, J.Z. Wang, and R. Mezrich, *Variation of lateral ventricular volume during the cardiac cycle observed by mr imaging*, Am. J. Neuroradiol. **10** (1989), 1145–1149.

[63] D.N. Levine, *Pathogenesis of cervical spondylotic myelopathy*, J. Neurol. Neurosurg. Psychiatry **62** (1997), 334–340.

[64] ———, *The pathogenesis of normal pressure hydrocephalus: A theoretical analysis*, Bull. Math. Biol. **61** (1999), 875–916.

[65] ———, *Intracranial pressure and ventricular expansion in hydrocephalus: Have we been asking the wrong question?*, J. Neurol. Sci. **269** (2008), 1–11.

[66] V. Libertiaux and F. Pascon, *Viscoelastic modeling of brain tissue: A fractional calculus-based approach*, Mech. of Microstru. Solids **46** (2009), 81–90.

[67] A.A. Linninger, M. Xenos, D.C. Zhu, M.R. Somayaji, S. Kondapalli, and R.D. Penn, *Cerebrospinal fluid flow in the normal and hydrocephalic human brain*, IEEE Trans. Biomed. Eng. **54** (2007), no. 2, 291–302.

[68] Andreas A. Linninger, Cristian Tsakiris, David C. Zhu, Michalis Xenos, Peter Roycewicz, Zachary Danziger, and Richard Penn, *Pulsatile cerebrospinal fluid dynamics in the human brain*, IEEE Trans. Biomed. Eng. **52** (2005), no. 4, 557–565.

[69] J.G. Mandell, T. Neuberger, C.S. Drapaca, A.G. Webb, and S.J. Schiff, *The dynamics of brain and cerebrospinal fluid growth in normal versus hydrocephalic mice*, J. Neurosurg. Pediatr. (2010), Accepted April 2010.

[70] Susan S. Margulies and Kirk L. Thibault, *Infant skull and suture properties: Measurements and implications for mechanisms of pediatric brain injury*, J. Biomech. Eng. **122** (2000), 364–371.

[71] A. Marmarou, K. Shulman, and R.M. Rosende, *A nonlinear analysis of the cerebrospinal fluid system and intracranial pressure dynamics*, J. Neurosurg. **48** (1978), 332–344.

[72] A. Marmarou, H.F. Young, and G.A. Aygok, *Estimated incidence of normal pressure hydrocephalus and shunt outcome in patients residing in assisted-living and extended-care facilities*, Neurosurg. Focus **22** (2007), no. 4, E1.

[73] C. May, J.A. Kaye, J.R. Atack, M.B. Schapiro, R.P. Friedland, and S.I. Rapoport, *Cerebrospinal fluid production is reduced in healthy aging*, Neurology **40** (1990), 500–503.

[74] D.G. McLone, *Critque for: Di Rocco, C.; Di Trapani, G.; Pettorossi, V.E., and Caldarelli, M.: On the pathology of experimental hydrocephalus induced by artificial increase in endoventricular CSF pulse pressure*, Child's Brain **5** (1979), no. 6, 583.

[75] K.K. Mendis, R. Stalnaker, and S.H. Advani, *A constitutive relationship for large deformation finite element modeling of brain tissue*, J. Biomech. Eng. Trans. ASME **117** (1995), 279–285.

[76] David K. Menon and John M. Turner, *Textbook of neuroanaesthesia and critical care*, Cambridge, 2000.

[77] T.H. Milhorat, *Choroid plexus and cerebrospinal fluid production*, Science **166** (1969), 1514–1516.

[78] K. Miller, *Constitutive model of brain tissue suitable for finite element analysis of surgical procedures*, J. Biomech. **32** (1999), 531–537.

[79] K. Miller and K. Chinzei, *Constitutive modelling of brain tissue: Experiment and theory*, J. Biomech. **30** (1997), no. 11/12, 1115–1121.

[80] ———, *Mechanical properties of brain tissue in tension*, J. Biomech. **35** (2002), 483–490.

[81] Kenneth S. Miller and Bertram Ross, *Fractional greens' functions*, Indian J. Pure Appl. Math. **22** (1991), no. 9, 763–767.

[82] M. Miyagami and S. Nakamura dn N. Moriyasu, *Hydrodynamics of the CSF under experimental occlusion of superior sagittal sinus*, No Shinkei Geka. **3** (1975), 739–745.

[83] S. Momjian and D. Bichsel, *Nonlinear poroplastic model of ventricular dilation in hydrocphalus*, J. Neurosurg. **109** (2008), 100–107.

[84] M.Stastna, G. Tenti, S. Sivaloganathan, and James M. Drake, *Brain biomechanics: consolidation theory of hydrocephalus. variable permeability and transient effects*, Canad. Appl. Math. Quart. **7** (1999), no. 1, 93–109.

[85] T. Nagashima, N. Tamaki, S. Matsumoto, B. Horwitz, and Y. Seguchi, *Biomechanics of hydrocephalus: a new theoretical model*, Neurosurg. **21** (1987), no. 6, 898–904.

[86] G. Nagra, L. Koh, I. Aubert, M. Kim, and M. Johnston, *Intraventricular injection of antibodies to β_1-integrins generates pressure gradients in the brain favouring hydrocephalus development in rats*, Am. J. Physiol. Regul. Integr. Comp. Physiol. **297** (2009), no. 5, R1312–R1321.

[87] University of Iowa Health Care, *Acute brain injury - a guide for family and friends*, www.uihealthcare.com, May 2010.

[88] American Association of Neurological Surgeons, *Adult onset hydrocephalus*, www.neurosurgerytoday.org/what/patient_e/adult.asp, March 2007.

[89] Uniformed Services University of the Health Sciences, *Medpix medical image database*, https://rad.usuhs.edu/medpix/, May 2010.

[90] M.R. Pamidi and S.H. Advani, *Nonlinear constitutive relations for human brain tissue*, Trans. ASME **100** (1978), 44–48.

[91] D. Pang and E. Altschuler, *Low-pressure hydrocephalic state and viscoelastic alterations in the brain*, Neurosurg. **35** (1994), no. 4, 643–655.

[92] C. Papaiconomou, A. Zakarov, R. Bozanovic-Sosic, and M. Johnston, *Does neonatal cerebrospinal fluid absorption occur via arachnoid projections or extracranial lymphatics?*, Am. J. Physiol. **283** (2002), R869–R879.

[93] A. Peña, N.G. Harris, M.D. Bolton, M. Czosnyka, and J.D. Pickard, *Communicating hydrocephalus: the biomechanics of progressive ventricular enlargement revisited*, Acta Neurochir. **81** (2002), 59–63.

[94] Richard D. Penn, Max C. Lee, Andreas A. Linninger, Keith Miesel, Steven Ning Lu, and Lee Stylos, *Pressure gradients in the brain in an experimental model of hydrocephalus*, J. Neurosurg. **102** (2005), 1069–1075.

[95] Richard D. Penn and Andreas Linninger, *The physics of hydrocephalus*, Pediatr. Neurosurg. **45** (2009), 161–174.

[96] I. Podlubny, *Geometric and physical interpretation of fractional integration and fractional differentiation*, Fract. Calc. Appl. Anal. **5** (2002), no. 4, 367–386, Dedicated to the 60th anniversary of Prof. Francesco Mainardi. MR MR1967839 (2004k:26011a)

[97] Harold D. Portnoy, Michael Chopp, Craig Branch, and Michael B. Shannon, *Cerebrospinal fluid pulse waveform as an indicator of cerebral autoregulation*, J. Neurosurg. **56** (1982), 666–678.

[98] J.E. Preston, *Ageing choroid plexus-cerebrospinal fluid system*, Microsc. Res. Tech. **52** (2001), 31–37.

[99] K.R. Rajagopal and A.S. Wineman, *A constitutive equation for nonlinear solids which undergo deformation induced microstructural changes*, Int. J. Plasticity **8** (1992), 385–395.

[100] M. Rammling, M. Madan, L. Paul, B. Behnam, and J.V. Pattisapu, *Evidence for reduced lymphatic CSF absorption in the H-Tx rat hydrocephalus model*, Cerebrspinal Fluid Res. **5** (2008), 15.

[101] C. Di Rocco, *Hydrocephalus and cerebrospinal fluid pulses*, Hydrocephalus (K. Shapiro, A. Marmarou, and H. Portnoy, eds.), Raven Press, 1984, pp. 231–249.

[102] C. Di Rocco, G. Di Trapani, V.E. Pettorossi, and M. Caldarelli, *On the pathology of experimental hydrocephalus induced by artificial increase in endoventricular CSF pulse pressure*, Child's Brain **5** (1979), no. 2, 81–95.

[103] L. Rogers, *Operators and fractional derivatives for viscoelastic constitutive equations*, J. Rheol. **27** (1983), 351–372.

[104] G.A. Rosenberg, L. Saland, and W.T. Kyner, *Pathophysiology of periventricular tissue changes with raised CSF pressure in cats*, J. Neurosurg. **59** (1983), no. 4, 606–611.

[105] E. Ruoslahti, *Brain extracellular matrix*, Glycobiol. **6** (1996), no. 5, 489–492.

[106] Ingolf Sack, Bernd Beierbach, Jens Wuerfel, Dieter Klatt, Uwe Hamhaber, Sebastian Papazoglou, Peter Martus, and Jürgen Braun, *The impact of aging and gender on brain viscoelasticity*, NeuroImage **46** (2009), 652–657.

[107] J. Sahuquillo, E. Rubio, A. Codina, A. Molins, J.M. Guitart, M.A. Poca, and A. Chasampi, *Reappraisal of the intracranial pressure and cerebrospinal fluid dynamics in patients with the so-called "normal pressure hydrocephalus" syndrome*, Acta Neurochir. **112** (1991), 50–61.

[108] J.J. Seibert, T.C. McCowan, W.M. Chadduck, J.R. Adametz, C.M. Glasier, S.L. Williamson, B.J. Taylor, R.E. Jr Leithiser, J.R. McConnell, C.A. Stansell, and et al., *Duplex pulsed doppler US versus intracranial pressure in the neonate: Clinical and experimental studies*, Radiology **171** (1989), no. 1, 155–159.

[109] K. Shapiro, A. Fried, and A. Marmarou, *Biomechanical and hydrodynamic characterization of the hydrocephalic infant*, J. Neurosurg. **63** (1985), 69–75.

[110] K. Shapiro, A. Marmarou, and K. Shulman, *Characterization of clinical CSF dynamics and neural axis compliance using the pressure-volume index: I. the normal pressure-volume index*, Ann. Neurol. **7** (1980), no. 6, 508–514.

[111] L.Z. Shuck and S.H. Advani, *Rheological response of human brain tissue in shear*, Trans. ASME J. Basic Eng. **94** (1972), 905–911.

[112] S. Sivaloganathan, M. Stastna, G. Tenti, and J.M. Drake, *Biomechanics of the brain: A theoretical and numberical study of Biot's equations of consolidation theory with deformation-dependent permeability*, Int. J. Non Linear Mech. **40** (2005), 1149–1159.

[113] ———, *A viscoelastic approach to the modelling of hydrocephalus*, Appl. Math. Comput. **163** (2005), 1097–1107.

[114] ———, *A viscoelastic model of the brain parenchyma with pulsatile ventricular pressure*, Appl. Math. Comput. **165** (2005), 687–698.

[115] S. Sivaloganathan, G. Tenti, and J.M. Drake, *Mathematical pressure volume models of the cerebrospinal fluid*, Appl. Math. Comput. **94** (1998), 243–266.

[116] Frederick H. Sklar and Martin Linder, *The role of the pressure-volume relationship of brain elasticity in the mechanics and treatment of hydrocephalus*, Hydrocephalus (K. Shapiro, A. Marmarou, and H. Portnoy, eds.), Raven Press, 1984, pp. 323–336.

[117] Alan Smillie, Ian Sobey, and Zoltan Molnar, *A hydroelastic model of hydrocephalus*, J. Fluid Mech. **539** (2005), 417–443.

[118] Ian Sobey and Benedikt Wirth, *Effect of non-linear permeability in a spherically symmetric model of hydrocephalus*, Math. Med. Biol. **23** (2006), no. 4, 339–361.

[119] L. Suarez and A. Shokooh, *Response of systems with damping materials modeled using fractional calculus*, Appl. Mech. Rev. **48** (1995), S118–S126.

[120] Z. Taylor and K. Miller, *Reassessment of brain elasticity for analysis of biomechanisms of hydrocephalus*, J. Biomech. **37** (2004), 1263–1269.

[121] G. Tenti, S. Sivaloganathan, and J.M. Drake, *Brain biomechanics: Steady-state consolidation theory of hydrocephalus*, Can. App. Math. Q. **7** (1999), no. 1, 111–124.

[122] ———, *The synchrony of arterial and CSF pulsations is not due to resonance*, Pediatr. Neurosurg. **37** (2002), 221–222.

[123] ———, *Mathematical modeling of the brain: Principles and challenges*, Neurosurg. **62** (2008), no. 5, 1146–1157.

[124] Kirk L. Thibault and Susan S. Margulies, *Age-dependent material properties of the porcine cerebrum: effect on pediatric inertial head injury criteria*, J. Biomech. **31** (1998), 1119–1126.

[125] D. Tsakanikas and N. Relkin, *Normal pressure hydrocephalus*, Semin. Neurol. **27** (2007), no. 1, 58–65.

[126] B. Tully and Y. Ventikos, *Coupling poroelasticity and CFD for cerebrospinal fluid hydrodynamics*, IEEE Trans. Biomed. Eng. **56** (2009), no. 6, 1644–1651.

[127] Arnold Verruijt, *Flow through porous media*, ch. Elastic Storage of Aquifers, pp. 331–376, Academic Press, 1969.

[128] E.K. Walsh and A. Schettini, *Brain tissue elasticity and CSF elastance*, Intracranial Pressure VII (J.T. Hoff and A.L. Betz, eds.), Springer-Verlag, 1989, pp. 271–274.

[129] H.C. Wang and A.S. Wineman, *A mathematical model for the determination of viscoelastic behavior of brain in vivo. I. oscillatory response*, J. Biomech. **5** (1972), no. 5, 431–446.

[130] G.N. Watson, *A treatise on the theory of Bessel functions*, Cambridge University Press, 1922, http://www.archive.org/details/treatiseontheory00watsuoft.

[131] K.P. Wilkie, C.S. Drapaca, and S. Sivaloganathan, *Aging impact on brain biomechanics with applications to hydrocephalus*, Med. Eng. Phys. (2010), Submitted.

[132] ———, *A theoretical study of the effect of intraventricular pulsations on the pathogenesis of hydrocephalus*, Appl. Math. Comput. **215** (2010), 3181–3191.

[133] C.B. Wilson and V.B. Bertan, *Interruption of the anterior choroidal artery in experimental hydrocephalus*, Arch. Neurol. **17** (1967), no. 6, 614–619.

[134] Benedikt Wirth and Ian Sobey, *An axisymmetric and fully 3D poroelastic model for the evolution of hydrocephalus*, Math. Med. Biol. **23** (2006), no. 4, 363–388.